Synthesis by ammonolysis and luminescence properties of cerium or europium-doped oxynitrides with the apatite structure

Sébastien Thomas

N° d'ordre : 4698

THESIS

Presented at

L'UNIVERSITÉ BORDEAUX I

ÉCOLE DOCTORALE DES SCIENCES CHIMIQUES

by **Sébastien THOMAS**

FOR THE DEGREE OF

DOCTEUR

SPECIALITY: Physico-Chimie de la Matière Condensée

Synthesis by Ammonolysis and Luminescence Properties of Cerium or Europium-doped Oxynitrides with the Apatite Structure

---

Under the joint supervision of: **Amparo FUERTES and Alain GARCIA**

Presented on December 14th 2012

Jury:

M MAGLIONE Mario	Directeur de Recherche- ICMCB	Président
Mme CHADEYRON Geneviève	Professeur-ICCF- Université de Clermont-Ferrand	Rapporteur
M TESSIER Franck	Chargé de Recherche-ISCR-Université de Rennes I	Rapporteur
Mme BUISSETTE Valérie	R&D manager- Rhodia/Solvay	Examinateur
Mme FUERTES Amparo	Professor-ICMAB-CSIC	Examinateur
M GARCIA Alain	Chargé de Recherche-ICMCB-Université Bordeaux I	Examinateur

Remerciements

Cette thèse est le résultat d'un travail de trois ans prenant place en grande partie à l'Institut de Chimie de la Matière Condensée de Bordeaux. En premier lieu, je tiens donc tout naturellement à exprimer ma gratitude à l'égard de Monsieur Claude Delmas, ancien Directeur de l'Institut de Chimie de la Matière Condensée de Bordeaux, pour m'avoir accueilli au sein de son laboratoire. Je souhaiterais également remercier son successeur, Monsieur Mario Maglione, pour l'honneur qu'il m'a fait en acceptant de présider mon jury de thèse.

Je voudrais également remercier Mr Franck Tessier, chargé de recherche à l'ISCR (Université de Rennes 1) et Mme Geneviève Chadeyron, professeur à l'ICCF (Université de Clermont-Ferrand) pour avoir accepté de juger ce travail en qualité de rapporteurs.

Ce projet, né de la collaboration entre trois entités : l'ICMCB, l' Institut de Ciència de Materials de Barcelona (ICMAB) et l'entreprise Solvay-Rhodia, a permis un travail mêlant des problématiques scientifiques industrielles et plus fondamentales, ainsi que de riches échanges entre des laboratoires appartenant à des pays différents. Je souhaiterais remercier avec insistance mes deux directeurs de thèse que sont Alain Garcia et Amparo Fuertes. J'ai eu avec le premier de passionnantes discussions scientifiques au sujet des propriétés optiques de nos matériaux. Les enquêtes quasi policières que nous avons pu mener par moment resteront dans ma mémoire et impacteront ma manière de faire de la recherche à l'avenir. J'aimerai le remercier tout particulièrement pour sa bonne humeur et sa capacité à positiver au jour le jour. La seconde, qui a su me faire profiter de sa grande expérience en cristallochimie et en synthèse, m'a aussi donné l'opportunité de me former en travaillant avec de talentueux scientifiques. Merci également à Thierry Le Mercier et Valérie Buissette pour m'avoir donné un aperçu de ce que pouvait être la Recherche en industrie, et pour m'avoir soutenu à de nombreuses reprises. Je tenais également à remercier Véronique Jubera pour son aide dans l'organisation de cette thèse, ainsi que Benoît Glorieux.

Cette thèse a été l'occasion pour moi de travailler avec un grand nombre de personnes au sein de l'ICMCB et je tenais donc tout naturellement à les remercier: Michel Lahaye pour

son aide avec la spectroscopie Auger et la Microsonde X ; Catherine Labrugère pour les mesures XPS ; Michaël Josse, pour m'avoir patiemment guidé dans l'affinement Rietveld de mes données neutrons. Merci à Michel Ménétrier pour son aide avec les mesures de RMN du ^{29}Si ; au service RX de l'ICMCB, particulièrement efficace ; à Antoine Villesuzanne, pour l'aide qu'il m'a apporté avec la DFT ; et à Dominique Denux et Philippe Dagault pour les mesures d'ATG.

Un grand merci également à Marc Dussauze pour m'avoir permis de faire des mesures de spectroscopie Raman et Infrarouge au sein de l'ISM, et à Dominique Cavagnat, pour son aide au niveau de la simulation des spectres Raman et Infrarouge.

Una gran parte de la tesis se desarrolló en el ICMAB, situado en España, más exactamente en Bellaterra, al lado de Barcelona. Fue un gran placer trabajar allí. Me gustaría agradecer a toda la gente con quien he podido trabajar y conversar en el ICMAB. Me han acogido con mucha benevolencia desde el principio, y me han ayudado a integrarme rápidamente. Trabajar en el despacho ON FIRE ha sido por cierto una experiencia inolvidable! Gracias a todos los que fueron o son aun miembros del equipo: Nina, con su energía inagotable de todos los días; Javi, por su locura poética y por haber participado en construir mi cultura musical española; gracias también a Laura la Poppy Electro de Mollet; Ana Milena y su espíritu salsero; Alex el trabajador loco!; y Stefania también! Evidentemente, no olvido a todas las otras personas del ICMAB, exterior a este despacho que han participado de esta buena atmósfera: Ana López, Judith, las dos Jessicas, Jullieth ma pooooooule, Angela, Nerea, Otto, Oana…y todos los que olvido sin querer!

Un grand merci également à toutes les personnes du groupe III de l'ICMCB, a.q.a. les OPTIX. L'ambiance de travail au sein de ce groupe m'a paru très agréable et intellectuellement stimulante, notamment grâce à l'émulation que savent y créer les permanents. Une pensée spéciale pour Guigui, qui m'a supporté durant les derniers mois de la thèse dans notre bureau des sous-sols. Mais également : Maitre Bourhis, pour m'avoir précédé et montré la voie ; Hélène pour avoir su me transférer son instinct de la recherche d'emploi ; Lucile pour ces créations culinaires et Alex pour avoir réparé tout ce que j'ai cassé sans jamais broncher (ou presque… ^^).

Pour finir, merci à mes amis, aux personnes que j'ai pu rencontrer en dehors du monde scientifique lors des nombreux voyages de ces trois dernières années et qui ont su me motiver sans parfois forcément tout comprendre à ce que je faisais ! Merci à ma famille pour m'avoir appuyé et supporté, surtout pendant les derniers mois de la thèse, avec une pensée toute particulière pour ma mère.

Table of contents

General Introduction

General Introduction:

For ages, the human kind has been looking for reliable lighting sources. Recent awareness regarding global warming has highlighted the necessity to reduce energetic consumption. Materials Science is involved in this challenge, and notably lighting devices development follows this trend: energetic efficiency is now a fundamental characteristic to take in account when considering a lighting device. The phase out of incandescent light bulbs has been decided in many countries [5]. Compact fluorescent lamps and linear fluorescent tubes constitute a leading technology in the lighting market but the mercury vapor waste they generate after use could engender some environmental issues. Solid-State Lighting (SSL) appears as a promising alternative. Combining advantages like high efficiency, high lifetime, environmental friendliness and high potential of improvement, SSL-based devices will play an important part in the future of lighting.

Currently, the most widely spread technology for lighting using SSL (Backlighting in LCD displays, flashlight for cameras in smartphones…) is a combination between an InGaN blue Light Emitting Diode and a YAG: Ce^{3+} phosphor which absorbs a part of this light and converts it into yellow light. The combination of both emissions gives a cool white light. For home and office lighting, a warmer light is desirable and thus phosphors emitting at higher wavelength with high energetic efficiencies would help extend SSL to the general lighting market. Many researches are carried out worldwide to find new phosphors and industrially-convenient methods to synthesize it. In this context, rare earth doped (oxy)nitrides attract much attention as they combine broad band emissions in the yellow, orange or red with high energetic efficiencies and good thermal and chemical stabilities.

This thesis work has been dedicated to the synthesis of Eu^{2+} or Ce^{3+}-doped oxynitrides by heating oxide precursors in flowing $NH_3(g)$ at relatively low temperature. New phosphors based on the apatite structure have been discovered. Their structural characteristics and luminescent properties have been investigated.

The work presented in this thesis is the result of a collaboration between two laboratories dedicated to public research: l'Institut de Chimie de la Matière Condensée de Bordeaux (ICMCB, CNRS) and l' Institut de Ciència de Materials de Barcelona (ICMAB,

CSIC) under the supervision of specialty chemical company Rhodia-Solvay. In the context of the ONILUD (OxyNItrures LUminescents pour Diodes) project, initiated thanks to the European Excellency Network FAME directed by Jean ETOURNEAU, financed by both the Région Aquitaine and Rhodia-Solvay, this thesis has benefited from a large international collaboration.

The present work is divided as follow:

- The first chapter introduces in details the different themes tackled in this study. A short history of lighting technologies is given, and the advantages brought by Solid-State Lighting are highlighted. Methods for the synthesis of nitrides and oxynitrides are described. Eventually, a description of the apatite crystal structure is given.

- The second chapter is dedicated to the description of the synthesis method that has been used as well as the chemical and structural characterization of the samples obtained. A peculiar attention has been given to the determination of nitrogen content and distribution in the available sites in the crystal structure.

- In the third chapter, the concepts necessary to understand the properties of luminescent materials are introduced. The sometimes original luminescent features that have been obtained are described in details. A large part is dedicated to the understanding of these luminescent properties with respect to structural modifications brought by nitrogen introduction. Finally, some attempts to optimize the phosphor properties are discussed.

References:

[1] Patel, P. *MRS Bulletin* **36**, 678–680 (2011).

Chapter I:

Introduction

Chapter I: Introduction

I.1 Evolution of lighting technology

I.1.1. Lighting: A key research field for energy saving

Global warming and the growing scarcity of fossil fuels worldwide represent challenges which will require changes in the way we consume and produce energy. There is an urgent need for savings in energy consumption and natural resources exploitation, and this will be made possible by changing our habits as well as the technology we use for producing and employing energy. Scientific research will play a fundamental part in taking up these challenges.

In industrially developed countries, lighting represents a non-negligible part of the energy consumed. On average, in France, lighting represents 12.8% of the total residential sector electric energy consumption [1]. In the United States, it represents 19.81% of the building sectors (residential and commercial sectors together) electric energy consumption and 9.2% of its total energy consumption [2]. Worldwide demand for electricity is increasing rapidly. Indeed, by 2030, previsions based on current policies evaluate 77% of increase for global light consumption [3]. Interestingly, light consumption is very unequally distributed over countries in the world, and not only there is a difference between developing and developed countries, but also between occidental developed countries: in North America in average 101Mlmh is consumed per person and per year whereas this figure decreases to 42 Mlmh in Europe and to 3 Mlmh for India [3]. It is likely that developing countries will show increasing light consumption while more and more people get access to electricity and the need for light may increase even more than forecasted.

A key point is that technologies used for general lighting are so far particularly energetically inefficient. The incandescent light bulb, still enlightening our everyday life, converts only 5% of the electrical energy input in visible light. The rest is mainly lost as heat. The compact fluorescent lamps, appointed to replace at least for short-term old incandescent light bulb, reach a 20% energetic efficiency. As a comparison, a gasoline engine has typically 30% efficiency in the conversion of chemical energy in movement, and a electric oven converts 70% of the received energy in heat. Obviously, the physical phenomena, as well as

the types of energy involved are not comparable, but this helps to assess the gap which has to be filled. In this context, lighting constitutes a crucial field of research for energy saving.

I.1.2. A short history of lighting technology

Modern lighting technology history started in the 19th century, with the first demonstration of arc lamp concept by British scientist sir Humphry Davy in 1809 and the numerous patents for incandescent light bulbs between 1835 and 1879, notably attributed to Joseph Swan and Thomas Edison, American funder of General Electric. These two inventions, based on two different physical phenomena, *viz.* incandescence (Emission of visible electromagnetic radiations from a hot body as a result of its temperature) and excitation-desexcitation of an ionized gas under a flow of electrons, have constituted the two main models of lighting device for more than one century. Incandescent lamps and gas-discharge lamps still occupy today the major part of our lighting environment whereas candles and kerosene lamps have been replaced progressively. (They are still used nowadays by 1.5 billion people in the world without access to electricity) [4]

Incandescent light bulb was imagined and designed in several forms since its first demonstration in 1835 by James Bowman Lindsay. Filament material, filament shape and size, vacuum or gas filling, bulb material, are some of the characteristics which have been played with to increase lifetime and luminescence of this device [4]. Its modern form, consisting of a tungsten filament introduced in a glass bulb containing argon and nitrogen has had a long and a successful career. Cheap to produce, emitting a pleasant warm light, the incandescent bulb, quickly abandoned for street lighting, commercial and industrial building because of its extremely low efficiency, has been widely used in our homes during more than one century. Halogen lamps, which first related patent was delivered in 1882, derive from the initial incandescent light bulb technology: a small amount of halogen gas is added (generally Iodine or Bromine) which allows a redeposition of the evaporated tungsten back on the filament via halogen chemical cycles, thus increasing the lifetime of the device. Those lamps can be operated at higher temperature than a standard gas-filled lamp, giving higher luminous efficacy. (The luminous efficacy is expressed in lumen/Watt, describing the quantity of light perceived by the human eye for a given electrical power input)

Gas-discharge lamps have also played an important role in lighting history. Their working principle is based on the excitation of an ionized gas by collisions between its atoms and electrons. Atoms of the ionized gas (plasma) enter in an excited state by collisions with electrons from the arc. Their subsequent relaxation gives rise to light, with characteristics depending on the gas nature. This can be a single gas or a mixture of several gases. Noble gas like neon, argon, krypton or xenon can be used alone or mixed with additional materials like mercury, sodium or metal halides. In this case, the noble gas is there for starting the gas discharge phenomenon, the other material being responsible for the eventual emission characteristics.

The first mercury vapor lamp was invented in 1901, and an improved form, close to the current model for this technology, was patented in the 1930s to be used for general lighting. This technology has nevertheless been surpassed by metal halide lamps, developed in the 1960s, where the gas constituting the atmosphere of the electric arc is a mixture of vaporized mercury and metal halides. They are currently applied for large area overhead illumination like in parking lots, arenas, or factories.

Sodium vapor lamp are gas-discharge lamps containing a small amount of argon and neon to start the gas discharge, and solid sodium, readily vaporized and being responsible for the luminescent properties of the device. Its distinctive feature is to show a typical yellow light emission, nearly monochromatic, corresponding to the Sodium emission rays, mainly at 589.0 nm and 589.6 nm. As a result, lit objects are only seen by reflection of this light on them, in such a way that the color rendering index is close to zero (Color Rendering Index, or CRI, describes the capacity of a light source to render the “true” color of an object through the human vision). Nevertheless they show very high efficacies, and this is the reason why they are already used. The subdued light produced gives also a distinctive atmosphere appreciated in certain cases: movies, some stone built districts; and shows less lighting contamination than other lighting source. They appeared in the 1930s with other gas-discharge lamps and exist in two versions: low-pressure and high-pressure. High pressure sodium vapor lamps show broader emission spectra.

Fluorescent lamps, which first appeared at the end of the 1920s, derive of the operating principle of a gas-discharge lamp. Their specificity lies in glass tube coating with phosphors, solid crystalline materials which convert short-UV light emitted by the gas-

discharge lamp in visible light. They have been widely used as single linear tubes, but also exist as bulbs, with one or several folded tubes, and called compact fluorescent lamps (CFL).

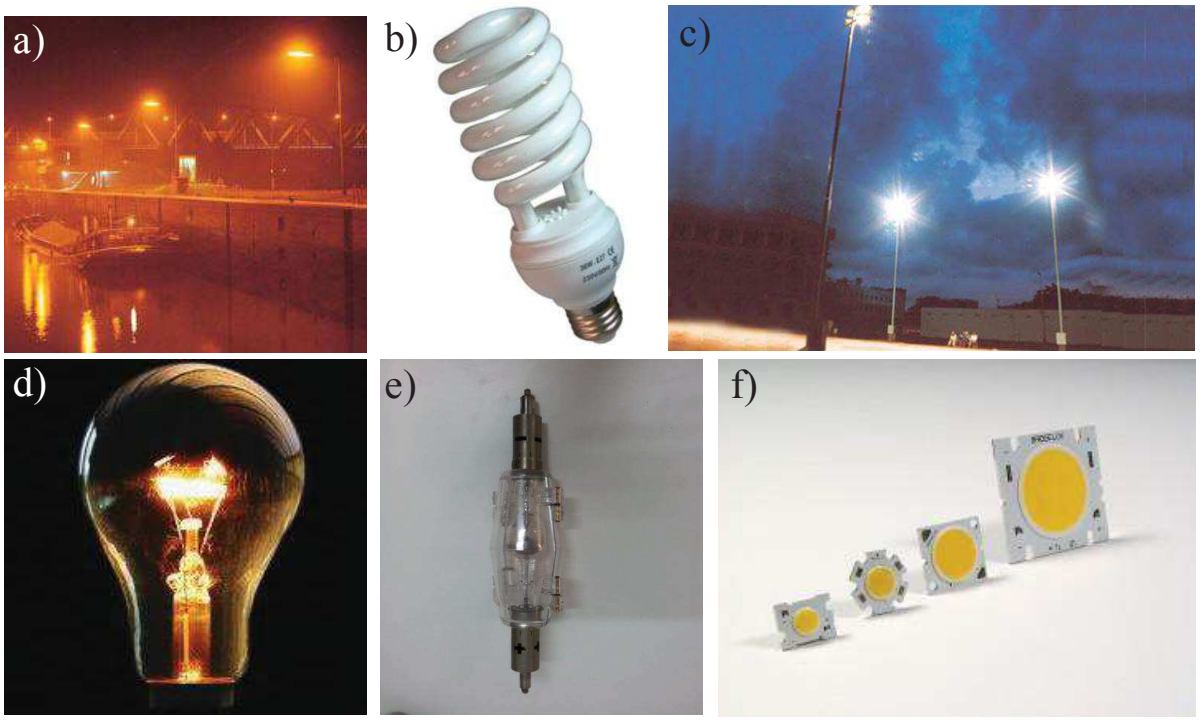

Figure I-1. a) Harbor lighting by sodium vapor lamp b) Compact fluorescent lamp c) Metal halide lamps for stadium lighting d) The classical light incandescent bulb e) A Xenon arc lamp, used in our spectrofluorimeter f) Some examples of white LEDs.

Nowadays, incandescent light bulbs are being phased out in several countries (Brazil and Venezuela in 2005, France in 2010, and a complete removal of Europe's shops forecasted in 2013, in 2014 for United States) [5]. This policy is justified by the extremely low energy efficiency of this old technology in spite of its low production costs. Compact fluorescent lamps are currently replacing the classical incandescent light bulb in our homes. They present good color rendering index, efficacies at least 5 times higher than their incandescent counterpart and high lifetime. Nevertheless, the mercury vapors that they contain make them hazardous waste once their lifetime has overpassed. Huge quantities of these devices raise the question of their waste treatment regarding the possible environmental damage [6].

CFLs and linear fluorescent tubes currently constitute a leading technology in the lighting market. Long fluorescent tubes have largely taken over in offices, commercial buildings and factories. The phase out of incandescent light bulb will also greatly benefit to

CLFs in the next decade at least. Solid-state-lighting is expected to play an important part in the future of lighting technologies because of its huge potential (High lifetime, high efficiency and environmental friendliness). Nevertheless, many economical and technological issues still have to be settled [6]. Table I-1 shows characteristics for different lamp technologies in their current state of development (Data reproduced from [2]).

Table I-1. Typical characteristics for a set of lamp technologies

Current technology	**Efficacy (lumens/Watt)**	**Lifetime (hours)**	**Color Rendering Index**
Incandescent	10 - 19	750 – 2500	97
Halogen	14 - 20	2000 - 3500	99
Fluorescent – T8 (Tube, 1 inch diameter)	35 – 87	7500 - 20000	52 – 90
Compact Fluorescent	40 - 70	10000	82
Mercury Vapor	25 - 50	29000	15 – 50
Metal Halide	50 - 115	3000 - 20000	65 – 70
High-Pressure Sodium	50 – 124	29000	22
Low-Pressure Sodium	18 – 180	18000	0
Solid State Lighting	20 – 100	15000 - 50000	33 - 97

I.2. Light Emitting Diodes: A breakthrough technology

I.2.1. Working principle of a Light Emitting Diode (LED)

A LED is an electronic device composed of several layers of semiconductor single crystals linked to electrodes and lying on a substrate. The most basic LED is composed of two semiconductor layers forming a p-n junction: one n-doped (containing electrons in excess), and one p-doped (containing positively charged holes). Doping in semiconducting layers is achieved by introducing trace amounts of interstitial atoms with a higher or lower charge than the atoms of the host. When a tension is applied to the diode, electrons and holes flow into the junction and radiative recombination might occur in the area where both holes and electrons meet. The semiconductor material constituting the diode is characterized by a bandgap of a given energy. Close to the junction, electrons and holes will have different localized energy

levels. While recombining, electrons will lose energy by releasing photons depending on the bandgap value.

Current LED devices generally include an active layer between the n-doped layer and the p-doped layer (Figure I-2) in order to maximize the probabilities of recombination. This active layer is generally very thin in III-nitrides LEDs (typically 2nm), whereas n-doped and p-doped layers are thicker. All high brightness LEDs commercialized nowadays have active layers containing quantum wells: a semiconductor with a given band gap is inserted in another semiconductor of higher band gap. Electrons and holes are thus confined within the barriers fixed by the high band gap, and discrete energy levels appear in the well. This design greatly improves the efficiency of the device. Phenomena lying beside this technology are referred to as diode Electroluminescence.

The first LED reported in history was created by the Russian Oleg Vladimirovich Losev in 1927. After the war, much work has been carried out on infrared LEDs, notably made of GaAs [7]. Nick Holonyak Jr. developed in 1962 the first practical visible light emitting diode. Made of GaAsP and emitting a weak red light, it was working with milliAmper current [8]. Finally, the first high-brightness blue LED was demonstrated by Shuji Nakamura of Nichia Corporation in 1992, it was made of GaN. This technology has been greatly improved since then, and devices working with current close to one Amper are now common. Gallium nitride development has constituted a definite scientific advance in the field of LED. Before, bright LEDs were only available for emitting from yellow to infrared. This discovery gave access to blue, green and hence white LED. Indeed, InN, GaN and AlN (the so-called III-nitrides) are three semiconductors which have the same hexagonal crystal structure, with different bandgap: 0.7 eV, 3.4 eV and 6.2 eV respectively (It is worth noting that the term “semiconductor” is to some extent abusive here, given that 3.4 eV and 6.2 eV can be considered as high values for a semiconductor band gap). While varying the proportion of indium, gallium and aluminium in a nitride semiconductor, it is theoretically possible to tune the light emitted as desired from deep UV to infrared.

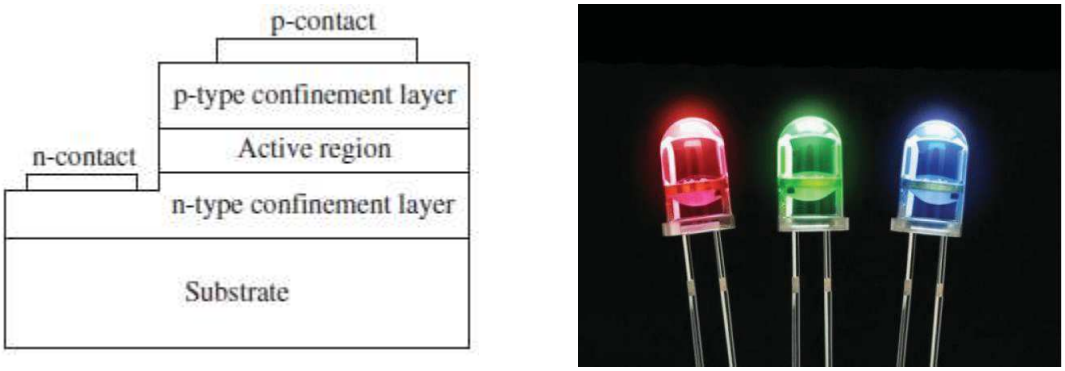

Figure I-2. General scheme of a Light Emitting Diode (left), three LEDs with three different emissions in the visible spectrum (right).

LEDs have found applications in a growing number of devices: Infrared LEDs are used in remote controllers and optical fibers communications, UV-Led for water and air purification, white-LEDs as backlighting in LCD screenplay, in biomedical applications (Photo rejuvenation or treatments of biological clock disorder for instance) [9], as well as indoor plant cultivations [10], and eventually they appear to present excellent characteristics for becoming the future dominant technology for general lighting.

I.2.2. Organic Light Emitting Diodes (OLEDs)

In parallel with inorganic semiconductor-based LEDs, much public and private research is conducted on light emitting diodes made of organic compounds. Organic light emitting diodes (OLED) are constituted of several layers of organic materials. Typically, a hole transport layer, an electron transport layer, and an emissive layer. They are deposited on a transparent conducting surface (Indium Tin Oxide for instance) and encapsulated. This technology would bring very interesting properties relative to their inorganic counterpart. The potentially flexible devices would give birth to a lot of exciting possibilities like flexible displays which could take the form of any surface or electronic paper, which could be fold on demand. The other original prospect related to this technology is to use ink-jet printing as a high scale industrial process of fabrication. Until now, they are mainly used in small screens for portable devices like phones and game consoles.

Nevertheless, OLED's development suffers of some important drawbacks until now, the main one being the low chemical resistance of the materials considered. A lot of research

is carried out nowadays on encapsulation in order to limit these degradations. They also generally have efficiencies much lower than classic LEDs. [14]

I.2.3. White light production

In order to produce white light with LEDs, two main different strategies are generally considered: multi-chip and single-chip devices. The first one involves combining several LEDs together in the same device, each of one emitting in a different wavelength area of the visible spectra, typically red, blue and green. The second strategy involves combining LED chips with down-converting phosphors. Ideally, the first configuration would be the most efficient, avoiding the losses inherent to conversion of light by phosphors, because each LED emits its own light. However it also generates many difficulties that are not fixed yet. Indeed, until now the different semiconductor materials employed to obtain the different colors, for instance red green and blue, do not show the same efficiencies. Green LEDs are a peculiar subject of preoccupation, as they already present, for reasons not elucidated yet, very low efficiencies. For instance, in InGaN-based LED, the intensity of light is decreasing when Indium content increases. That is to say, from tuning the band gap in order to emit blue to green light, the efficiency drops. This fact is known as “the green gap” and motivates many researches in the field for filling the gap existing between this LED and the others. Another subject of concern is the inhomogeneity of LEDs behavior with time and temperature. Typically, some LEDs will lose efficiency at a faster rate than other, or will behave differently with temperature variations, resulting in a degradation of the color rendering index of the light. This phenomenon forces the constructors and scientist to add feedback electronic devices regulating the power input in each LEDs in order to keep the same general light color with time. This gives multi-chips white-LEDs fabrication a higher cost and complexity.

The typical white LED available in the market is a combination of an InGaN blue LED with $Y_3Al_5O_{12}$: Ce^{3+} (YAG: Ce^{3+}) phosphor, which has a broad band yellow emission while being excited in the blue. Other combinations are possible, for instance, devices composed of a UV-emitting LED like AlGaN, with various phosphors emitting red/green/blue, or orange/blue light. Such devices are also called pc-LEDs, standing for phosphor converted-LEDs.

A third alternative strategy has also been recently envisaged and is being investigated: Monolithic white LED. The active layer would be constituted of many quantum wells $In_xGa_{1-x}N$/GaN emitting at various wavelength, but with a special design avoiding too much loss recombination on dislocations [11]. The resulting monolithic device would emit white light with high efficiency and could simplify the production lines. Nevertheless, this technology is still at its beginning and Color Rendering Index are very low.

I.2.4. Advantages of white pc-LEDs over other technologies

White pc-LEDs present a tremendous number of advantages over other lighting technologies (Table I-1). In their current state of development, they can be found to have high efficacies, ten times higher than incandescent bulb and higher than compact fluorescent lamps. Even if their efficacies are not that impressive until now, what makes them so promising, is their progression curve: while technologies like halide lamps have "only" seen their efficacies increasing of 40 lum/W in 45 years, LEDs have seen an improvement of 100 lm/W in 10 years (Figure I-3). Haitz's law, similar to Moore's law (for predicting the doubling of the number of Si transistors in a cheap every 18-24 months), predicts that the LED's luminous output per package doubles every 18-24 months whereas the cost decreases [12].

The theoretical maximum efficacy of an ideal white light source (with a CRI of 100), is 240 lm/W. Indeed, the sensibility of the human eye, which during the day has its maximum at approximately 555 nm (Slightly yellowish green), and decreases progressively for both higher and lower wavelength, defines a threshold for efficacy at each emission wavelength. At 555 nm, the maximum efficacy reaches 683 lm/W, and for a white light source with a CRI of 90, which is considered as a good value for white light, it reaches 408 lm/W. The progresses possible are thus large and very promising.[6]

A supplementary advantage which is non-negligible with solid-state-lighting is the devices lifespan. While an incandescent light bulb last in average 1000 hours, and a compact fluorescent lamp 10000 hours, a white-Led can reach 100000 hours of lifetime. This is thanks to the semiconductor material which does not deteriorate at all under temperature of use or through excitation-emission cycles. Furthermore, White-LEDs do not contain toxic materials.

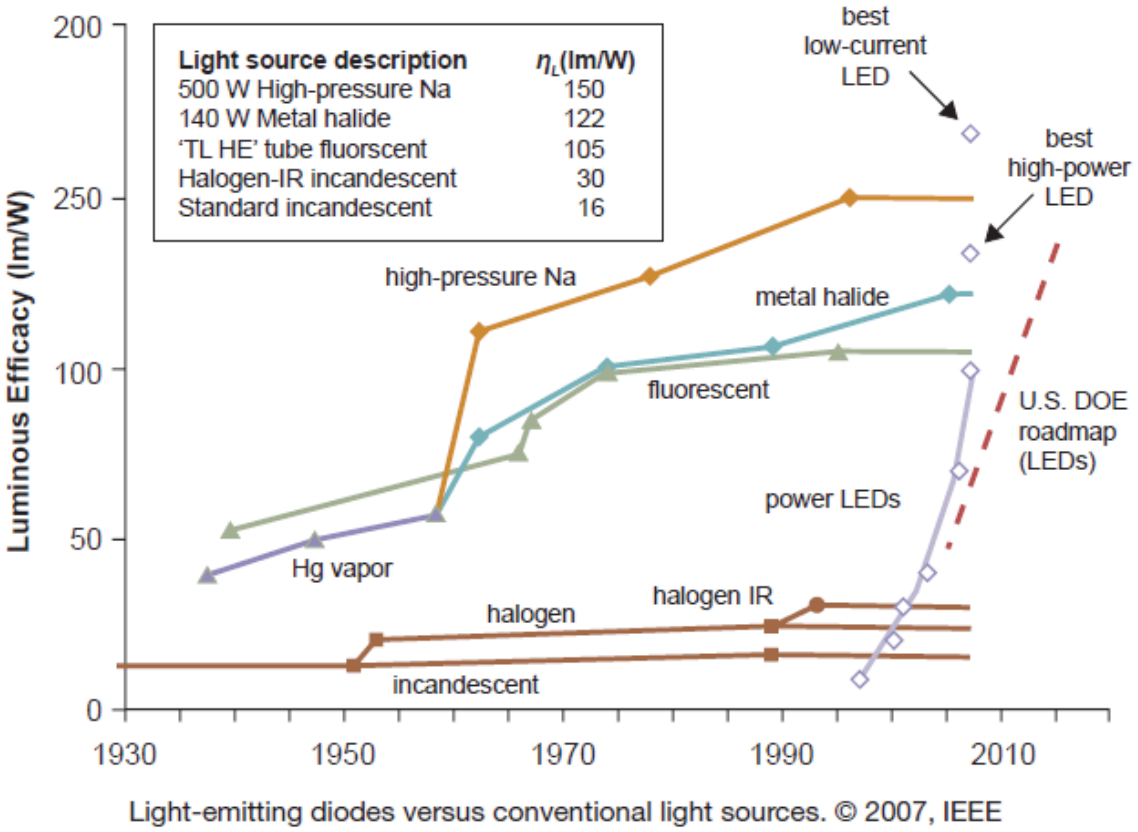

Figure I-3. Evolution of luminous efficacy (lm/W) over the past decades for different categories of lighting technologies.

To finish, LEDs are also considered as very promising light sources because they allow imagining new applications for light in our everyday lives. As this technology is in nature closely related to electronics, it is a perfect candidate for smart lighting applications. Actually, the output power of the produced light can be modulated very quickly which make possible the communication between devices without altering the lighting features observed by users. In a house for instance, lighting devices could communicate between each others to automatically adapt lighting to where people are localized. Another example of smart lighting application is lighting systems respecting the circadian rhythm. Indeed, the human wake-up/sleep cycles are affected by the variations of the color temperature of the light, changing between midday and evening for instance. Home lighting synchronized with the biological clock could have a beneficial effect on health [13].

I.2.5. LED technology's needs for further improvement

What is currently hampering the entry of LED in the general lighting market? The main problem that can be identified is the cost. In fact, construction of white-LEDs based on GaN semiconductors remains more expensive than producing CFLs and light bulbs. One solution for decreasing the costs of semi-conductors fabrication would be to enlarge the substrates they are grown on. By increasing the surface, more LEDs are produced at a time, but the edge effect is also greatly reduced. Moreover, an important industrial issue in LED production is to determine the nature of the substrate material. Most LEDs are currently grown on 2 inch diameter sapphire or SiC substrates. Cost reduction could be achieved by growing GaN-based LEDs on 6 inch silicon wafer, already really common in electronics industry. However, the higher lattice mismatch between Silicon and GaN generates a higher rate of dislocation, detrimental to the LEDs lighting performances. [15]

Heat management is also a crucial point of improvement for White LEDs. As other small electronic devices, LEDs generates heat on a small area which results in high temperature rise for the device. This heat can drastically decrease the lifespan of the device if not taken in charge: temperature junction is for instance very important. Other parts of the device may degrade like the epoxy resin encapsulating the device, which suffer from blue light and heat exposure, and becomes more fragile [16]. More efficient ways of evacuating heat from the device constitute an active field of research [17].

Another problem which arises is directly related to LED working. Indeed, a big issue with GaN devices is that the efficiency decreases at high current. For commonly expected luminescence output, a high current is necessary. Corresponding devices are called high power LEDs.

Currently, nearly all the white LEDs available on the market are composed of a blue light emitting InGaN based LED and yellow phosphor YAG: Ce^{3+}. The light emitted has a CRI of about 70, which is not sufficient to fulfill the needs of customers for home use. Furthermore, YAG: Ce^{3+} shows some thermal quenching. As the multichips methods still carry many unfixed problems, the single chip method is still the most considered by market specialists. There is a need for high efficiency dowconverting phosphors emitting at high wavelength and cheap to produce.

I.3 Nitrides and oxynitrides as phosphor materials

I.3.1. Why (oxy)nitride phosphors?

The acceleration of research on phosphors which can have applications in white pc-LEDs coincide with the development of LEDs based on wide bang gap semi-conductors like GaN or InGaN, emitting in the UV-Blue with high energetic efficiency. Indeed, since their discovery by Nakamura in 1992 [18] [19], the number of articles related with the study of phosphors has never stopped increasing. (Figure I-4)

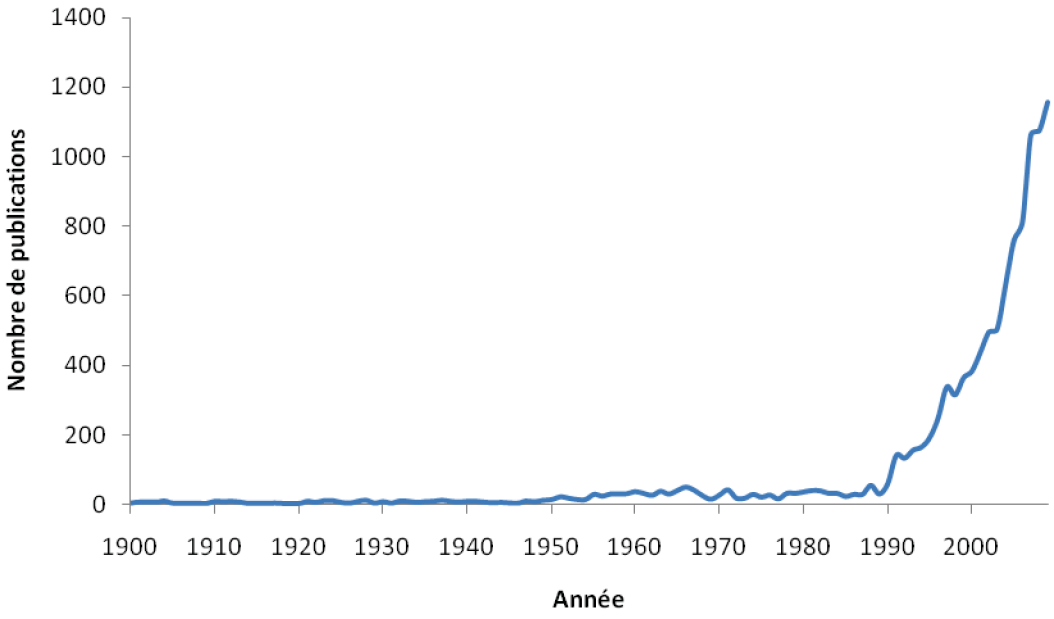

Figure I-4. Number of articles containing the key-word “phosphor” in their title from 1900 to 2009. (Source: www.IsiWebOfKnowledge.com)

As stated previously, there is a need for new phosphors emitting at long wavelength in the visible, with high efficiencies and good thermal and chemical stability. Nitride and oxynitride phosphors have attracted considerable attention because they show the required physical and chemical features. Why do nitrides attract so much attention compared with other class of compounds?

Currently, a market suitable phosphor needs to fulfill the following requirements:

- A broad band emission at long wavelength. Yellow, orange and red phosphors attract much attention. Green phosphors are nevertheless also necessary for high CRI light sources.
- A corresponding excitation ideally matching with either the emission of an InGaN blue diode, peaking at 460 nm, or with the emission of an AlGaN UV-LED typically with a maxima at 290 nm.
- A high external quantum efficiency (EQE), which is the ratio expressed in percentage of the total number of photons emitted by the phosphor to the total number of incident photons coming from the exciting source.
- Ability to resist to the temperatures generated during LED working (typically between 90 and 100°C). Luminescent properties also have to be stable. A good resistance to thermal quenching is a key point. Indeed, the widely used YAG: Ce^{3+} phosphor has the main drawback of loosing efficiency with temperature. In some cases, nitrides have shown better characteristics in this aspect.

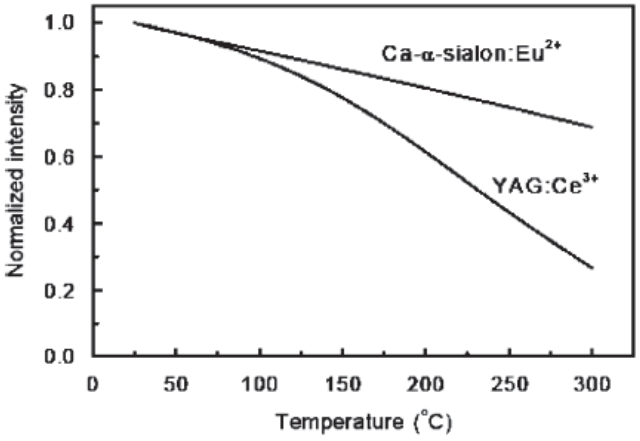

Figure I-5. Curves describing the evolution of normalized emission intensity with temperature for YAG: Ce^{3+} and Ca-α-SiAlON: Eu^{2+}. (Taken from [20])

- Non toxicity.
- The possibility to precisely tune the emission properties by making vary one accessible parameter of the phosphor. Generally, it is related to its composition. It can be a ratio between two cationic elements in the structure, or the activator concentration for instance.

Some sulfides show nice luminescent features: CaS: Eu^{2+} and SrS: Eu^{2+} as red phosphors and $SrGa_2S_4$: Eu^{2+} as green phosphor for instance. They can be used to improve

the CRI of the white-LED. Nevertheless, they also show low chemical stability in the environment of the LED package, notably because of their high sensitivity to humidity [20].

Compared to oxides, rare-earth doped nitrides show generally higher emission and excitation wavelength [20] [21] [22]. Eu^{2+} and Ce^{3+} show luminescence properties involving 4f→5d transitions. The higher formal charge of N^{3-} compared with O^{2-} increases the crystal-field splitting of the 5d orbitals and the lower electronegativity of nitrogen leads to a decrease of the energies of all 5d levels compared to 4f energy levels because of the decrease of the interelectronic repulsion. The resulting 5d→4f transitions occur at lower energy, *i.e.* at higher wavelength. These aspects will be explained with more detail in Chapter III. Furthermore, many ternary nitridosilicates doped with Eu^{2+} or Ce^{3+} show high efficiencies and good thermal stability (Figure I-5).

I.3.2. (Oxy)nitride phosphors

One of the first rare-earth doped nitride phosphors was reported in 1997 for $CaSiN_2$: Eu^{2+} [23]. In the following years, other nitride host lattices were explored like La_3SiN_5: Eu^{2+} [24], $Ba_2Si_5N_8$: Eu^{2+} [25], and also oxynitride systems with Y-Si-O-N: Ce^{3+} [26]. The broad emission and excitation bands as well as the relatively high red-shifted luminescence obtained attracted increasing attention on (oxy)nitrides as host lattices for rare-earth doped phosphors. During the last ten years, many new host lattices were explored [20] [21] [22].

Different Ce-doped and Eu-doped (oxy)nitride phosphors can be found in the literature. Their main luminescence features have been listed. Values of emission and excitation wavelengths in nanometers are given as a rough guide. In fact, it is somewhat difficult to give absolute values for emission and excitation of phosphors with broad band features. Moreover, it has to be kept in mind that the luminescent properties of a phosphor powder can vary with the grain sizes and morphologies, porosity, surface defects, and hence are strongly influenced by the synthesis method.

Table I-2. Luminescence features of reported Eu-doped and Ce-doped (oxy)nitride phosphors

Phosphor Formula	**Excitation (nm)**	**Emission (nm)**
$MSi_2O_2N_2 : Ce^{3+}, Na^+$ (M= Ba, Sr, Ca) [27]	Ba: 300-360 nm Sr: 300-360 nm Ca: 300-360 nm	Ba: 396 nm (**Violet**) Sr: 473 nm Ca: 392 nm
$LnSiO_2N : Ce^{3+}$ (Ln= La, Y)	La: 322-356 nm [8] Y: 340-370 nm [26]	La: 416 nm [8] Y: 405-442 nm [26]
$La_3Si_8O_4N_{11} : Ce^{3+}$ [8]	290-365 nm	424-458 nm
$La_3SiN_5 : Ce^{3+}$ [29]	355-380 nm	464-475 nm (**Blue**)
$Ln_5Si_3O_{12}N : Ce^{3+}$	La: 312-360 nm [8] Y: 290-355 nm [26]	La: 478 nm [8] Y: 475 nm [26]
β-Sialon : Ce^{3+}	310-340 nm ; 410 nm	470-490 nm [30]
$Y_2Si_3O_3N_4 : Ce^{3+}$ [26]	310-390 nm	493 nm
M-α-Sialon : Ce^{3+} (Ca, Y) [31]	285, 385 nm	500 nm
$Ln_4Si_2O_2N_7 : Ce^{3+}$ (Ln= La, Y)	La: 317-345 nm [8] Y: 355-400 nm [26]	La: 488 nm [8] Y: 504 nm [26]
$M_2Si_5N_8 : Ce^{3+}$-(Li^+, Na^+) (M= Ba, Sr, Ca) [32]	Ba: 370-450 nm Sr: 370-450 nm Ca: 370-450 nm	Ba: 451 nm Sr: 553 nm Ca: 470 nm
β-Sialon : Eu^{2+} [33]	280-480 nm	528-550 nm (**Green**)
$La_3SiN_5 : Eu^{2+}$ [34]	250-450 nm	553nm
$MSi_2O_2N_2 : Eu^{2+}$ (M= Ba, Sr, Ca) [35]	Ba: 380 nm Sr: 360 nm Ca: 355 nm	Ba: 537 nm Sr: 494 nm Ca: 560 nm
$MSi_6N_8 : Eu^{2+}$ (M= Ba, Sr, Ca)	Ba: 310 nm Sr: 290-400 nm Ca: 325-450 nm	Ba: 500 nm [36] Sr: 450 nm [37] Ca: 550-560 nm [38]
$La_3Si_6N_{11}$: Ce^{3+} [39]	370, 455 nm	543-585 nm (**Yellow**)
M-α-Sialon : Eu^{2+} (Li, Ca, Y)	Li : 300, 435-449 nm Ca : 300, 400-450 nm Y : 300, 400-450 nm	Li : 563-586 nm [40] Ca : 590 nm [41] Y : 611 nm [42]
$M_2Si_5N_8 : Eu^{2+}$ (M= Ba, Sr, Ca) [43]	Ba: 300-500 nm Sr: 300-500 nm Ca: 300-500 nm	Ba: 570-680 Sr: 609-680 Ca: 605-615
$MSiN_2 : Ce^{3+}, Li^+$ (M= Ba, Sr, Ca)	Ba: 395 nm Sr: 305 and 403 nm Ca: 440-550 nm	Ba: 485 nm [44] Sr: 535 nm [44] Ca: 625 nm [45]
$MSiN_2 : Eu^{2+}$ (M= Ba, Sr, Ca)	Ba: 395 nm Sr: 395 nm Ca: 400 nm	Ba: 600-630 nm [44] Sr: 670-685 nm [44] Ca: 605 nm [45]
$CaAlSiN_3 : Ce^{3+}$ [46]	260-300 nm, 390-500nm	570-603 nm
$CaAlSiN_3 : Eu^{2+}$ [47] [48]	460 nm	630-644nm (Red)

While skimming through this list, it appears clearly that silicon ternary nitrides and oxynitrides represents the major part of current research on high emission wavelength phosphors. Low cost of silicon and relatively good results obtained with these materials seem to explain this fact. Another interesting fact is that there are only few Ce^{3+}-doped oxynitrides emitting at long wavelength and most of them are blue emitting phosphors.

Many rare-earth doped (oxy)nitrides can be considered already as viable for use in high performance white LEDs. Indeed, green (β-SiAlON: Eu^{2+}, $SrSi_2O_2N_2$: Eu^{2+}), yellow (Ca-α-SiAlON: Eu^{2+}) and orange or red phosphors ($CaAlSiN_3$: Ce^{3+} or Eu^{2+}, $M_2Si_5N_8$: Eu^{2+}, $CaSiN_2$: Eu^{2+}) have been widely investigated. Generally what is limiting their entry in the market is that the synthesis methods necessary for their production are too expensive or not adapted to industrial scale production. In the next sections, we will describe the main synthesis techniques to produce nitrides and oxynitrides.

I.3.3. Nitride chemistry

Oxides are still now the most studied, known and characterized group of compounds in Solid Chemistry. Known oxides number surpasses by far nitrides compounds. For instance in 1993, only a few hundred nitrides had been characterized whereas the number of known oxides reached more than ten thousand [49].

Nitrogen is mostly abundant in atmosphere and in living organisms on earth, but not in the earth's crust. Whereas the atmosphere is composed of nearly 78% nitrogen and 21% oxygen, nitrogen is in small quantity in the earth's mantle and crust, compared to many elements like O, Si, Fe or Al (about $5x10^{-5}$ % of Nitrogen for 46% of Oxygen)[50]. This is notably due to the thermodynamic of triple bonding N≡N formation. Moreover, the high positive enthalpy of formation of N^{3-} ion starting from N atom (nearly 3 times the energy necessary to form O^{2-} from O atom) explains the trend of nitrogen to form mainly non-ionic bonding, except with the most electropositive elements. These thermodynamic factors explain both nitrides scarcity and their tendency to form non usual or even unique structures. Research on nitrides [49] [51] [52] [53] [54] [55] and oxynitrides [56] [57] [1] has progressed substantially in recent years and many promising and relevant compounds have been found.

Materials with high chemical, thermal and mechanical stability can be formed between nitrogen and other elements. For elements having electronegativity close to nitrogen, highly covalent bonds can be formed. Resulting structures are covalent and highly reticulated with strong bonds. Nitridosilicates, which constitute a very important class of materials in the field of phosphors, well illustrate this fact. Indeed, nitrogen atoms can make one, two, three or even four bondings with silicon atoms, forming very dense networks. Moreover, side sharing between neighbouring tetrahedras in order to form Si_2N_6 units is also possible [59]. As a comparison, oxygen can only make at most two bonds with silicon. Those nitride compounds are highly stable over temperature (until 1600°C at least), and are not attacked by hot acids or bases [60]. That is also the reason why ternary, quaternary or multinary nitridosilicates are chemically stable and show low thermal quenching.

Nonetheless, the thermal stability of a nitride is generally lower than an oxide. This is again due to the very high bonding energy of N_2 (941 $kJ.mol^{-1}$) which can constitute a product of decomposition from nitride compounds. The thermal dissociation accompanied of N_2 formation will occur at lower temperature than for corresponding oxides with formation of O_2 (Bonding energy: 499 $kJ.mol^{-1}$). For instance, aluminium nitride AlN will decompose above 1800°C while the extrapolated ebullition point of Al_2O_3 is around 3000°C.

The affinity of most of the elements is higher for oxygen than for nitrogen, and hence bonding energies for a given element with oxygen will be higher than with nitrogen. Formation of oxides is thus a non-negligible co-reaction during nitrides synthesis. Preparation of pure nitrides requires a total exclusion of water and oxygen.

I.3.4. Oxynitrides

Oxygen and nitrogen show similar crystallochemical (ionic radii, preferential coordination number) and electronic characteristics (anionic polarisability, electronegativity), which allows the formation of analogous structures and the mutual substitution of both anions at the same crystallographic positions giving rise to solid solutions. Oxynitrides perovskite have attracted considerable attention [57] [61] [2] but many other structures have been explored: scheelite [63], fluorite [64], baddeleyite [65] and pyrochlore [3], for instance. It is generally considered that nitrogen can replace oxygen following one of two ways [67]:

1) Replacement of oxygen by nitrogen with formation of an anionic vacancy:

$$2\ N^{3-} + 1\ \square = 3\ O^{2-}$$

2) Or cross-substitution, where the anionic substitution takes place concomitantly with a cationic substitution, for instance:

$$R^{3+} + N^{3-} = M^{2+} + O^{2-}$$

With R a rare-earth and M an alkaline-earth.

Oxynitrides of several structural types are thus accessible and for a given phase, the ratio O/N can be varied continuously, offering the possibility to tune the physical properties of a given material. Several examples of oxynitride materials with tunable properties exist: the photocatalytical activity of TiO_2 is shifted to the visible range and can be adjusted when doped with nitrogen [68]; non-toxic inorganic pigments with body colors from yellow to red have been obtained with the solid solution $Ca_{1-x}La_xTaO_{2-x}N_{1+x}$ [69]; large colossal magnetoresistances have been recently discovered in $EuNbO_2N$ and $EuWO_2N$ [4] [71].

Table I-3. Crystal chemical and electronic features of nitrogen and oxygen [57]

	N	**O**
Anionic charge z	-3	-2
Electronegativity	3.0	3.4
Anionic Polarisability ($Å^3$)	1.10	0.80
Electronic Affinity $A \rightarrow A^{z-}$ ($kJ.Mol^{-1}$)	1736	601
Bonding energy A-A ($kJ.mol^{-1}$)	941	499
Ionic radius (Å)	1.46	1.38
Coordination number	II–VIII	II–VIII

I.3.5. Synthetic approaches

The synthesis of nitride-based materials is less straightforward than for oxides because of their lower stability. As a consequence, a rigorous control of oxygen concentration during the synthesis is needed in order to avoid decomposition in oxides at high temperatures. The main methods of preparation of nitride-based materials are described below with emphasis on the synthesis approaches of oxynitridosilicates as they constitute the most widely investigated compounds as white LEDs' nitride-based phosphors.

I.3.5.1. Solid State Reaction in nitrogen gas atmosphere

The most widely used method of synthesis of (oxy)nitridosilicates is the thermal treatment at high temperature (between 1300°C and 1600°C) of a sintered pellet containing a stoichiometric mixture of metal oxides, carbonates and/or nitrides (*e.g.* Si_3N_4 or AlN) under a high-pressure $N_{2(g)}$, or a mixture N_2/H_2 (typically 90/10 or 95/5 % v/v) if reducing conditions are required. In many examples, a high-temperature gas pressure sintering furnace is used. Because of the low reactivity of N_2 at atmospheric pressure, more efficient nitrogen sources have been investigated.

I.3.5.2. Carbothermal Reduction Nitridation (CRN)

In this method a mixture of oxide powders, nitrides and carbon (activated carbon, graphite powder) is treated at high temperature under flowing N_2. The carbon powder is a reducing agent and reacts with the metal oxide forming CO:

$$3M_xO + 3C + N_2 \rightarrow M_{3x}N_2 + 3CO$$

Typically, quantities of carbon are between 60 and 120% molar of the total oxygen quantity in the starting material [72]. This quantity of carbon has to be optimized. Indeed, if it is too low, formation of secondary oxide phases can occur, and if it is too high, the quantity of carbonated residue becomes too important and, in the case of phosphor synthesis, can harm luminescent properties.

I.3.5.3. Ammonolysis: an example of Gas Reduction Nitridation

Gaseous ammonia $NH_{3(g)}$, is stable at room temperature and atmospheric pressure, but thermodynamically unstable at temperatures higher than 458 K (185°C) [73], decomposing into $N_{2(g)}$ and $H_{2(g)}$:

$$2NH_{3(g)} \rightarrow N_{2(g)} + 3H_{2(g)}$$

However, ammonia is kinetically stable at much higher temperature than its thermodynamic stability limits. The minimum temperature for an efficient thermal activation of ammonia is 823 K that is to say 550°C. It is thus possible to work with ammonia at room pressure. The decomposition reaction produces hydrogen and nitrogen in a native state, highly reactive. At a sufficiently high temperature, the use of ammonia gas at atmospheric pressure is equivalent to using $N_{2(g)}/H_{2(g)}$ at high pressure.

Several types of metallic compounds can be nitrided with the help of flowing ammonia gas by using adequate temperatures. Typical reactions for binary oxides and sesquioxides are:

$$M_2O_{3(s)} + 2NH_{3(g)} \rightarrow 2MN_{(s)} + 3\ H_2O_{(g)}$$

$$MO_{2(s)} + \frac{4}{3}NH_{3(g)} \rightarrow MN_{(s)} + 2\ H_2O_{(g)} + \frac{1}{6}N_{2(g)}$$

Sulfides can react with ammonia to form nitrides [74]. Sulfides are less stable than oxides and thus more reactive. Nevertheless, nitridation reaction produces hydrogen sulfide $H_2S_{(g)}$, which is less stable than water. Globally the reaction is thermodynamically more advantageous starting with sulfides.

The ammonolysis of metal chlorides produces $HCl_{(g)}$. The reactions are more favored from the point of view of thermodynamics because they lead to three moles of $HCl_{(g)}$ per mole of $NH_{3(g)}$. The free enthalpy for the ammonolysis reaction forming three moles of gas is higher and thus the stabilization of the nitride is favored. Nevertheless, it is worth noting that most of the chlorides are gases at the necessary temperatures (*e.g.* $SiCl_4$ boiling point= 57.3°C), which favors the formation of nanocrystals at high-temperature, but also generates important technical constraints. The example of $Si_3N_{4(s)}$ synthesis by ammonolysis using three different types of precursors, (1) oxide, (2) sulfide and (3) chloride, well illustrates these statements:

$$\frac{3}{4}SiO_{2(s)} + NH_{3(g)} \rightarrow \frac{1}{4}Si_3N_{4(s)} + \frac{3}{2}H_2O_{(g)} \quad (1)$$

$$\frac{3}{4}SiS_{2(s)} + NH_{3(g)} \rightarrow \frac{1}{4}Si_3N_{4(s)} + \frac{3}{2}H_2S_{(g)} \quad (2)$$

$$\frac{3}{4}SiCl_{4(g)} + NH_{3(g)} \rightarrow \frac{1}{4}Si_3N_{4(s)} + 3\ HCl_{(g)} \quad (3)$$

Thermodynamic studies have allowed determining Ellingham diagrams for nitridation of oxides, sulfides or chlorides precursors in presence of ammonia [73]. The ammonolysis of oxide precursors are the less favorable. Indeed, most free enthalpies for reactions between oxides and ammonia are positive until 1400 K.However, direct nitridation of oxides can occur by maintaining H_2O partial pressure below the equilibrium partial pressure at the considered temperature. This will drive the reaction equilibrium towards the production of nitride. In practice, this is realized when working with flowing ammonia in a tubular furnace. Indeed, when NH_3 reacts with the oxide, the water is evacuated by the gas flow, decreasing the water

partial pressure around the sample. The free enthalpy of formation of nitride under ammonia decreases when the temperature increases for all the investigated oxides.

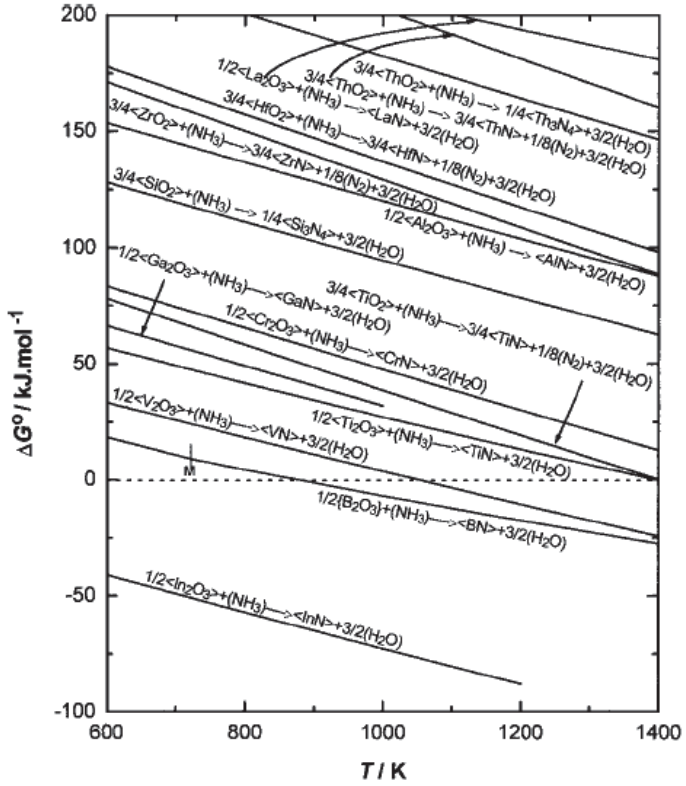

Figure I-6. Ellingham-Richardson-Jeffes diagram showing free standard enthalpy variation in with temperature for the formation of nitrides from metallic oxides and ammonia. [73]

Ammonolysis has been used for producing oxynitride glasses, for instance in the system Si-Al-O-N and phosphorus oxynitride glasses were synthesized with the same method [75]. More recently, direct nitridation of single crystals of $La_2Ti_2O_7$ and $Sr_2Nb_2O_7$ has been carried out [76]. $MSiN_2$ powders have been produced by reacting intermetallics MSi with flowing anhydrous ammonia at 550-1000°C [77].

Hydrazine (N_2H_4) has also been envisaged as a reactant to produce nitrides starting with the same type of precursors than in ammonolysis [73]. It is a highly more nitriding agent than ammonia and decomposes above 623K following the reaction:

$$3N_2H_4 \rightarrow 4\,NH_3 + N_2$$

This compound, mainly used as fuel for rockets or missile is however instable and difficult to handle, and eventually has to be activated at high temperature.

A gas mixture of ammonia and hydrocarbon has been used to prepare AlN. Typically, propane or methane are mixed at the rate of 0.5% in volume. Nanoparticules and nanofibers of AlN have thus been produced by reaction between alumina Al_2O_3 and an ammonia-propane flow at 1100-1400°C [78].

I.3.5.4. Ammonothermal synthesis

Solvothermal process has been used with liquid ammonia as a solvent. Many syntheses in supercritical ammonia have proved to be efficient for production of nitride phosphors. Synthesis in supercritical ammonia can be used to obtain a variety of metal amides, imides and nitrides. Liquid ammonia is also a good solvent for synthesis of nitride phosphors because alkali, alkaline-earth (except Be) as well as lanthanides are soluble under atmospheric pressure. As a consequence, synthesis in supercritical ammonia can be used either for direct synthesis of nitrides, or synthesis of highly reactive precursors like $Si(NH)_2$. The resulting precursors are air sensitive (to oxygen and humidity) and thus difficult to handle. A glove box is generally required for their synthesis and subsequent use. This technique of synthesis, giving good results at low temperature, is adapted to a laboratory scale, but not to industrial scale. The time necessary to obtain some precursors is also very long. ($Sr(NH_2)_2$ can be obtained after 5 days at 150°C and at 300 bars [79])

Even at high temperature, silicon nitride Si_3N_4, a widely used compound for the synthesis of (oxy)nitridosilicates, has a low chemical reactivity [49] [80]. It is widely applied as structural material in application intended for high performance at high temperature (turbocharger, bearings, cutting tools). Because of this inertia, it can only be used as starting material to synthesize ternary nitridosilicates when it is treated in addition with highly reactive metal nitrides like Li_3N or Mg_3N_2 are used:

$$Mg_3N_2 + Si_3N_4 \xrightarrow[1200°C\text{-}N_2]{} 3\ MgSiN_2$$

Schnick [55] has developed a synthetic method of ternary or higher nitrides consisting in reacting pure metals with silicidiimide $Si(NH)_2$. Silicidiimide is an amorphous compound relatively undefined but reactive, which is converted in amorphous Si_3N_4 at temperatures higher than 900°C. It is a precursor for the production of Si_3N_4 ceramics [80].

More recently, alkaline-earth metal amides have been used as precursors to prepare nitrides [79]. Metal amides can be produced by dissolving the corresponding metal in liquid ammonia [81], or in supercritical ammonia, where the reaction is faster and more complete.

I.3.5.5. Self-propagating reaction at high temperature

This technique involves the initiation of a highly exothermic reaction by heating at high temperature (ignition). The resulting high temperatures (higher than the temperature necessary to the ignition), released by the reaction at one point of the reactor engender the progressive reaction of all the other points in direct proximity with this heat, which forms a chain reaction propagating at all the sample. As an example, this technique has been reported to form Titanium carbonitride by heating a mixture of Ti metal and carbon powder in a reactor under flowing $N_{2(g)}$ [82].

This process can also be used for methathesis reactions. They correspond to chemical reaction involving the exchange of one or several atoms between chemical species having a close structure. Bonds in the resulting products are similar in number and nature than in the starting reactants. Fast synthesis of binary transition metal nitrides can be performed by the reaction between halides of transition metals with high oxidation states and alkaline metal nitrides *e.g.* Li_3N or Na_3N [83]. This way, TiN, HfN, ZrN are obtained by reaction between $TiCl_4$, $HfCl_4$ or $ZrCl_4$ with Li_3N. Corresponding reactions are:

$$MX_n + \frac{n}{3} Li_3N \rightarrow MN + nLiX + \frac{n/3-1}{2} N_{2(g)}$$

This kind of reaction has also been initiated by microwave [84], or by ignition in air [85].

I.3.5.6. Other methods

Many other less common approaches have been developed to synthesize nitrides. For instance, nanowires of α-Si_3N_4 have been synthesized by a reaction between an excess of silicon tetrachloride $SiCl_4$ and magnesium nitride at 600°C [86]. Sardar and Rao have produced GaN nanocrystals via a reaction in solvothermal conditions with an organic solvent [87]. Urea has been used as nitriding agent to produce ternary metal oxynitrides generally in the form of nanoparticles [88] starting from metal carbonates and transition metal oxides.

Heating a mixture of pure elements with sodium azide NaN_3 in a N_2 atmosphere, the so-called Na flux method, can lead to the formation of single crystals of binary, and ternary nitrides. NaN_3 decomposes above 275°C to give melted sodium and dinitrogen following the equation [89]:

$$2\ NaN_3 \rightarrow 2\ Na + 3\ N_2$$

It has been applied to the synthesis of binary nitrides like GaN [90], but also for ternary and multinary nitrides: single crystals of $MSiN_2$ (M= Ca, Sr, Ba) [77] and $Ba_5Si_2N_6$ [59], at respectively 900-1000°C and 750-850°C. Calcium cyanamide reduction has been used to synthesize $CaSrSi_5N_8 : Eu^{2+}$.[91]

I.3.5.7. Ammonolysis: a potential low-temperature method for oxynitride phosphors synthesis

Synthesis methods for nitride production are very diverse. Some involve highly reactive precursors like amide and imides which have to be synthesized prior to the final phosphor producing reaction. They involve many steps, sometimes very time consuming and controlled atmospheres. Others are more easily scalable, but involves high temperature, and are thus highly energy consuming (Solid State Reaction with $N_{2(g)}$ for instance).

Ammonolysis is a relatively old technique but has, to our knowledge, little been used for phosphor synthesis. We think that it shows many advantages for the synthesis of oxynitride phosphors. A typical set-up for ammonolysis only involves a tubular furnace with

flowing ammonia gas. This process can be easily adapted to an industrial fabrication scale. Furthermore, ammonolysis shows a decisive advantage for phosphor synthesis: ammonia gas, once activated, is both reducing and nitriding. Widely used rare-earth doping element like cerium and europium are commercially available in oxidation states that are not suitable for broad band emission (Cerium is in fact in the oxidation state 4+ in CeO_2 and europium is in the oxidation state +3 in Eu_2O_3 whereas broad band emission and excitation features are brought by Eu^{2+} and Ce^{3+}). Ammonia is a strong nitriding and reducing agent and is able to stabilize, at relatively low temperatures, the reduced oxidation states of cerium and europium. Finally, ammonia gas can be activated at relatively low temperature.

In this work we have used ammonolysis of oxysilicate and oxygermanate apatite precursors for the synthesis of oxynitridosilicate and oxynitridogermanate new phosphors. In the next section, we will describe the apatite structure and applications.

I.4 Apatites

I.4.1. Generalities

Apatites form a large group of compounds, both naturally occurring and synthetic. It is the most common phosphate mineral in nature, with various formulas, generally described as $Ca_5(PO_4)_3(OH,F,Cl)$ [92]. This mineral is also one of the few taking part in living organisms: human bones are constituted of more than 20% in weight of carbonated hydroxyapatite, with a low crystallinity and teeth's enamel is composed at 97% of hydroxyapatite [93].

The most common general formula for apatites can be written as $[A^I]_4[A^{II}]_6[(TO_4)_6][X]_2$ with A=La, Y, Ba, Sr, Ca, Pb, Cd…; T=P, Si, Ge, V, As… and X= OH, F Cl, O... Some variants also exist with the following description $[A^I]_4[A^{II}]_6[(TO_3)_6][X]_2$ or $[A^I]_4[A^{II}]_6[(TO_5)_6][X]_2$ [94].

I.4.2. Applications of apatites

I.4.2.1. Phosphors

Phosphate apatites have been widely used as phosphor host matrices. In the early years of fluorescent lamp, calcium halophosphates activated with antimony and manganese were often used [95]. Later, Eu^{2+}-doped halophosphate have been developed. One of the most known example is $Sr_5(PO_4)_3Cl : Eu^{2+}$, used as blue component in high efficiency compact fluorescent lamp [96]. The luminescence of cerium-doped silicate apatites [97] and oxynitridosilicate apatites have been studied [26] [8]. More recently, silicate apatites doped with europium have been investigated [98].

I.4.2.2. Other applications

Materials with apatite structure have been investigated in a wide range of scientific fields and have found various application: for instance their good resistance to high energy radiations make them interesting as nuclear waste holder [99], fluorapatite and hydroxyapatite have been investigated as supports in heterogeneous liquid phase catalysis[100], hydroxyapatite-based biomaterials can be used in reconstructive medicine[101] and copper-containing calcium and barium hydroxyapatites have been investigated as non-toxic pigment[102].

Apatites have also been intensively investigated as promising materials for electrolytes in low temperature (773-1023K) solid oxide fuel cells (SOFC). Rare-earth silico- and germanoapatites with the formula $RE_{10-x}(TO_4)_6O_{3-1.5x}$ have attracted much attention because they have shown the best properties as oxide anion conductors at low temperature, close to the traditional SOFC electrolyte in commercial systems working at higher temperature: yttria stabilized zirconia (YSZ).

I.4.3.The apatite crystal structure

I.4.3.1. A flexible structure

The apatite structure is composed of isolated TO_4 tetrahedra. Their spatial arrangement generates two cationic positions A^I and A^{II}. A^I cations are surrounded by TO_4 tetrahedra only, whereas A^{II} cations are localized at the periphery of c-axis-oriented tunnels that also accommodate X anions in a more central position. The structure can also be seen as made of a $A^I_4(TO_4)_6$ framework delimiting c-axis-oriented channels which will widen or shrink in function of the nature of the $A^{II}_6X_2$ units they contain. Indeed, A^IO_6 are trigonal prisms with two triangular faces that can twist one from each other in the plane perpendicular to the c-axis. The metaprism twist angle ϕ of A^IO_6 (mean angle O-A^I-O) trigonal prisms can vary in order to modify the size of the tunnels for a given framework. Larger angles will constrict the size of the tunnels. (Figure I-7)

Apatite has been reported as crystallizing in many space groups: $P6_3/m$, $P6_3$, P-3, P-6, $P2_1/m$, $P2_1$… The highest symmetry is obtained notably with hexagonal $P6_3/m$, but lower symmetries also exist depending on the compositional variations, for instance monoclinic $P2_1/m$ or triclinic P-1.

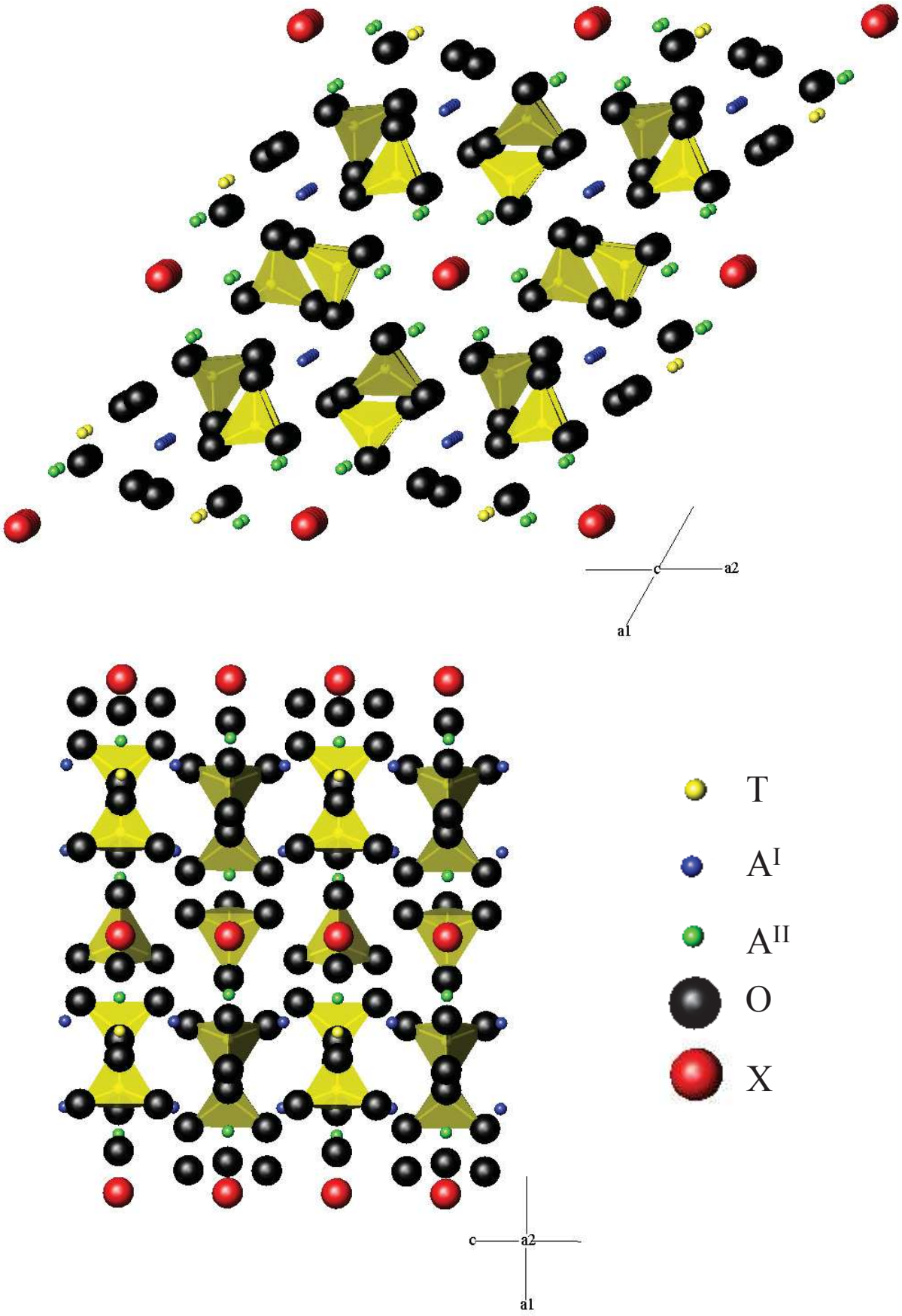

Figure I-7. Three-dimensional scheme of a typical apatite structure crystallizing in the $P6_3/m$ space-group.

The capacity of enlargement and shrinkage of the c-oriented tunnels give its high flexibility to the apatite structure. The metaprism twist angle will affect the tunnel expansion or collapse in function of its content. Cation substitution, cationic vacancies, interstitial anion can be accommodated by the structure. This is especially true for the lanthanum silico and germano apatites which will be described more in details in the following part.

I.4.3.2. A focus on lanthanum silicate apatites

Since the seminal work by Nakayama et al. [103] [104], much investigation has been carried out on lanthanum silico and germano apatites. Those compositions can accommodate lanthanum vacancies, but also substitution of lanthanum by an alkaline earth cation. This aliovalent substitution is possible because of the capacity of the apatite structure to accommodate variations in the total anion content. Indeed, variations of the cation stoichiometry or nature modify the total anion content per formula between 26 and 27. Two types of composition can be distinguished, unsubstituted apatites (1) and substituted apatites (2). The classical description of apatites like $Ca_5(PO_4)_3Cl$ in space-group $P6_3/m$ plans a total anion content of 26 in the unit cell. But, by substituting divalent alkaline-earth by trivalent rare-earth like La^{3+}, incorporation of extra-anion in the structure is necessary to conserve electroneutrality. It is thus possible to define the value δ, which represents the quantity of extra-oxygen in the formula. As a consequence, lanthanum apatites can be either understoichiometric ($\delta<0$), stoichiometric ($\delta=0$) or hyperstoichiometric ($\delta>0$) in oxygen.

$$(1)\ La_{9.33+x}\square_{0.67-x}Si_6O_{26+1.5x}\ (0 \le x \le 0.67)\ \delta=1.5x$$

$$(2)\ La_{8+x}Æ_{2-x}Si_6O_{26+0.5x}\ (0 \le x \le 2)\ \delta=0.5x$$

The exact localization of these extra oxygen anions, called interstitial oxygens, is a subject of concern because they are relevant for the observed high ionic conductivities of lanthanum apatite related materials. Numerous structural studies by neutron powder diffraction [20] [106] [107], synchrotron x-ray diffraction, and ab-initio calculations (DFT) [108], have been reported to determine the exact position of the interstitial oxygen and to suggest different conduction mechanisms.

Many compositions have been studied in these lanthanum apatite series because the interstitial oxygen interstitial quantity and lanthanum vacancies play an important part in oxide ion conductivity. Those studies have also highlighted the fact that not all compositions are possible and that there are compositional ranges of existence for apatites. Several authors have proposed 0.5 as the upper limit for δ [109] [22]. This can be justified by considering anion-anion distance in the c-oriented channels: if we consider that the ionic diameter of O^{2-} is 2.8 Å, and that in a unit cell the c parameter is about 7.2 Å, it appears clearly that there cannot be more than 2.5 oxygen atoms by unit cell. Following this statement range of compositions for lanthanum silicoapatites would be:

(1) $La_{9.33+x}\square_{0.67-x}Si_6O_{26+1.5x}$ $(0 \leq x \leq 0.33)$

(2) $La_{8+x}Æ_{2-x}Si_6O_{26+0.5x}$ $(0 \leq x \leq 1)$

I.4.3.3. Lanthanum germanate apatites

Lanthanum germanate apatites show some structural specificities compared to silicates. First of all, they show various crystalline forms depending on the compositions, because the longer Ge-O bonds allow additional structural relaxation. León-Reina *et al.* [107] have reported triclinic P-1 apatite phases for $La_{10-x}(GeO_4)_6O_{3-1.5x}$ in the range $9.66 \leq 10\text{-}x \leq 9.75$. A higher oxygen content seems to be stabilized in unsubstituted lanthanum germanate apatites because of these structural relaxations. In these cases some authors have placed the interstitial oxygen atoms near GeO_4 tetrahedra, leading to GeO_5 units. Indeed, they have found that a compound with the stoichiometry "$La_{10}(GeO_4)_6O_3$" was better described by the formula $La_{10}(GeO_4)_5(GeO_5)O_2$ [111]. Pseudomorphic phase transitions in lanthanum strontium germanate apatite have been reported by Pramana *et al.*[112]. The crystallographic structure changes with La/Sr atomic ratio, playing on total anion content. While increasing Sr content, the total anion content increases, and the general symmetry decreases going from hexagonal to monoclinic and triclinic.

I.4.3.4. A potential host lattice for oxynitride phosphors

The high flexibility of the apatite structure, notably its capacity to accommodate a wide range of oxygen content in the tunnels, makes it a good candidate for the stabilization of

oxynitridosilicates. On the other hand, the capacity of lanthanum apatites to accommodate cations with different oxidation states offers interesting possibilities for doping by optically active rare-earth like Ce^{3+} and Eu^{2+}. As a result lanthanum silicate- and germanate-apatites present good characteristics for being investigated as potential (oxy)nitride phosphors.

References for Chapter I:

[1] http://www.edf.com/html/panorama/. (Retrieved August 2012).

[2] *Building Energy Databook 2010 (http://buildingsdatabook.eren.doe.gov)*. Energy Efficiency and Renewable Energy, U.S. Department of Energy, Washington, DC, (2010).

[3] *Light's Labour's Lost: Policies for Energy-efficient Lighting*. International Energy Agency (IEA), (2006).

[4] Zissis, G. and Kitsinelis, S. *Journal of Physics D: Applied Physics* **42**, 173001 (2009).

[5] Patel, P. *MRS Bulletin* **36**, 678–680 (2011).

[6] Humphreys, C. J. *MRS Bulletin* **33**, 459–470 (2008).

[7] Braunstein, R. *Physical Review* **99**(6), 1892 (1955).

[8] Holonyak, N. and Bevacqua, S. *Applied Physics Letters* **1**, 82 (1962).

[9] Yeh, N. G., Wu, C.-H., and Cheng, T. C. *Renewable and Sustainable Energy Reviews* **14**(8), 2161 – 2166 (2010).

[10] Yeh, N. and Chung, J.-P. *Renewable and Sustainable Energy Reviews* **13**(8), 2175 – 2180 (2009).

[11] Chyurlia, P., Semond, F., Lester, T., Bardwell, J., Rolfe, S., Tang, H., and Tarr, N. *Electronics Letters* **46**(3), 240–242 (2010).

[12] Haitz, R., Kish, F., Tsao, J., and Nelson, J. *Compound Semiconductor Magazine* **6**, 34 (2000).

[13] Schubert, E. F. and Kim, J. K. *Science* **308**, 1274–1278 (2005).

[14] Kalyani, N. T. and Dhoble, S. J. *Renewable and Sustainable Energy Reviews* **16**, 2696–2723 (2012).

[15] *iLED: Innovation in Solid State Lighting* (3), 16 – 19 (March 2012).

[16] Chang, M.-H., Das, D., Varde, P., and Pecht, M. *Microelectronics Reliability* **52**(5), 762 – 782 (2012).

[17] *iLED : Innovation in Solid State Lighting* (1) June (June 2011).

[18] Nakamura, S. and Mukai, T. *Japanese Journal of Applied Physics* **31**, L1457–L1459 (1992).

[19] Nakamura, S. *Journal of Crystal Growth* **201-202**(0), 290 – 295 (1999).

[20] Xie, R.-J. and Hirosaki, N. *Science and Technology of Advanced Materials* **8**, 588–600 (2007).

[21] Xie, R.-J., Hirosaki, N., Sakuma, K., and Kimura, N. *Journal of Physics D: Applied Physics* **41**, 144013 (2008).

[22] He, X.-H., Lian, N., Sun, J.-H., and Guan, M.-Y. *Journal of Materials Science* **44**, 4763–4775 (2009).

[23] Lee, S. S., Lim, S. S., Sum, S., and Wager, J. F. *Proceedings of the Society of Photo-Optical Instrumentation (SPIE)* **3241**, 75–83 (1997).

[24] Uheda, K., Takizawa, H., Endo, T., Yamane, H., Shimada, M., Wang, C.-M., and Mitomo, M. *Journal of Luminescence* **87-89**, 967 – 969 (2000).

[25] Höppe, H., Lutz, H., Morys, P., Schnick, W., and Seilmeier, A. *Journal of Physics and Chemistry of Solids* **61**(12), 2001 – 2006 (2000).

[26] van Krevel, J., Hintzen, H., Metselaar, R., and Meijerink, A. *Journal of Alloys and Compounds* **268**(1-2), 272 – 277 (1998).

[27] Li, Y. Q., de With, G., and Hintzen, H. *Journal of Materials Chemistry* **15**, 4492–4496 (2005).

[28] Dierre, B., Xie, R.-J., Hirosaki, N., and Sekiguchi, T. *Journal of Materials Research* **22**(7), 1933–1941 (2007).

[29] Suehiro, T., Hirosaki, N., Xie, R.-J., and Sato, T. *Applied Physics Letters* **95**(5), 051903 (2009).

[30] Ryu, J. H., Won, H. S., Park, Y.-G., Kim, S. H., Song, W. Y., Suzuki, H., Yoon, C.-B., Kim, D. H., Park, W. J., and Yoon, C. *Electrochemical and Solid-State Letters* **13**(2), H30–H32 (2010).

[31] Xie, R.-J., Hirosaki, N., Mitomo, M., Yamamoto, Y., Suehiro, T., and Ohashi, N. *Journal of the American Ceramic Society* **87**(7), 1368–1370 (2004).

[32] Li, Y., de With, G., and Hintzen, H. *Journal of Luminescence* **116**(1-2), 107 – 116 (2006).

[33] Hirosaki, N., Xie, R.-J., Kimoto, K., Sekiguchi, T., Yamamoto, Y., Suehiro, T., and Mitomo, M. *Applied Physics Letters* **86**(21), 211905 (2005).

[34] Zhou, Y., ichi Yoshizawa, Y., Hirao, K., Lences, Z., and Sajgalik, P. *Journal of the European Ceramic Society* **31**(1-2), 151 – 157 (2011).

[35] Bachmann, V., Ronda, C., Oeckler, O., Schnick, W., and Meijerink, A. *Chemistry of Materials* **21**(2), 316–325 (2009).

[36] Xie, R.-J., Hirosaki, N., Li, Y., and Takeda, T. *Journal of Luminescence* **130**(2), 266 – 269 (2010).

[37] Shioi, K., Xie, N. H. R.-J., Takeda, T., and Li, Y. *Journal of Materials Science* **43**, 5659–5661 (2008).

[38] Song, Y., Choi, T., Luo, Y., Senthil, K., and Yoon, D. *Optical Materials* **33**(7), 989 – 991 (2011).

[39] Seto, T., Kijima, N., and Hirosaki, N. *ECS Transactions* **25**(9), 247–252 (2009).

[40] Xie, R.-J., Hirosaki, N., Mitomo, M., Sakuma, K., and Kimura, N. *Applied Physics Letters* **89**(24), 241103 (2006).

[41] Xie, R.-J., Hirosaki, N., Mitomo, M., Yamamoto, Y., Suehiro, T., and Sakuma, K. *The Journal of Physical Chemistry B* **108**(32), 12027–12031 (2004).

[42] Suehiro, T., Onuma, H., Hirosaki, N., Xie, R.-J., Sato, T., and Miyamoto, A. *The Journal of Physical Chemistry C* **114**(2), 1337–1342 (2010).

[43] Li, Y., van Steen, J., van Krevel, J., Botty, G., Delsing, A., DiSalvo, F., de With, G., and Hintzen, H. *Journal of Alloys and Compounds* **417**(1-2), 273 – 279 (2006).

[44] Duan, C. J., Wang, X. J., Otten, W. M., Delsing, A. C. A., Zhao, J. T., and Hintzen, H. T. *Chemistry of Materials* **20**(4), 1597–1605 (2008).

[45] Toquin, R. L. and Cheetham, A. *Chemical Physics Letters* **423**(4-6), 352 – 356 (2006).

[46] Li, Y. Q., Hirosaki, N., Xie, R. J., Takeda, T., and Mitomo, M. *Chemistry of Materials* **20**(21), 6704–6714 (2008).

[47] Uheda, K., Hirosaki, N., Yamamoto, Y., Naito, A., Nakajima, T., and Yamamoto, H. *Electrochemical and Solid-State Letters* **9**(4), H22–H25 (2006).

[48] Li, J., Watanabe, T., Sakamoto, N., Wada, H., Setoyama, T., and Yoshimura, M. *Chemistry of Materials* **20**(6), 2095–2105 (2008).

[49] Schnick, W. *Angewandte Chemie International Edition English* **32**, 806–818 (1993).

[50] http://www.elementschimiques.fr/?fr/proprietes/abondances. (Retrieved 17/08/12).

[51] Juza, R. *Advances in Inorganic Chemistry and Radiochemistry* **9**, 81–131 (1966).

[52] DiSalvo, F. J. and Clarke, S. J. *Current Opinion in Solid State and Materials Science* **1**, 241–249 (1996).

[53] Niewa, R. and DiSalvo, F. J. *Chemistry of Materials* **10**(10), 2733–2752 (1998).

[54] Gregory, D. H. *Journal of the Chemical Society, Dalton Transactions* , 259–270 (1999).

[55] Schnick, W. and Huppertz, H. *Chemistry - A European Journal* **3**, 679–683 (1997).

[56] Marchand, R., Laurent, Y., Guyader, J., L'haridon, P., and Verdier, P. *Journal of the European Ceramic Society* **8**, 197–213 (1991).

[57] Fuertes, A. *Dalton Transactions* **39**, 5942–5948 (2010).

[58] Fuertes, A. *Journal of Materials Chemistry* **22**, 3293–3299 (2012).

[59] Yamane, H. and DiSalvo, F. J. *Journal of Alloys and Compounds* **240**(1-2), 33 – 36 (1996).

[60] Schnick, W., Huppertz, H., and Lauterbach, R. *Journal of Materials Chemistry* **9**, 289–296 (1999).

[61] Marchand, R., Pors, F., and Laurent, Y. *Revue Internationale des Hautes Températures et des Réfractaires* **23**, 11 (1986).

[62] Clarke, S. J., Guinot, B. P., Michie, C. W., Calmont, M. J. C., and Rosseinsky, M. J. *Chemistry of Materials* **14**(1), 288–294 (2002).

[63] Antoine, P., Marchand, R., and Laurent, Y. *Revue Internationale des Hautes Températures et des Réfractaires* **24**, 43 (1987).

[64] Tessier, F., Maillard, P., Orhan, E., and Cheviré, F. *Materials Research Bulletin* **45**(2), 97 – 102 (2010).

[65] Armytage, D. and Fender, B. E. F. *Acta Crystallographica Section B* **30**, 809 (1974).

[66] Yang, M., Oro-Solé, J., Fuertes, A., and Attfield, J. P. *Chemistry of Materials* **22**(14), 4132–4134 (2010).

[67] Tessier, F. and Marchand, R. *Journal of Solid State Chemistry* **171**, 143–151 (2003).

[68] Asahi, R., Morikawa, T., Ohwaki, T., Aoki, K., and Taga, Y. *Science* **293**, 269–271 (2001).

[69] Jansen, M. and Letschert, H. P. *Nature* **404**, 980–982 (2000).

[70] Jorge, A. B., Oro-Sole, J., Bea, A. M., Mufti, N., Palstra, T. T. M., Rodgers, J. A., Attfield, J. P., and Fuertes, A. *Journal of the American Chemical Society* **130**(38), 12572–12573 (2008).

[71] Yang, M., Oro-Sole, J., Kusmartseva, A., Fuertes, A., and Attfield, J. P. *Journal of the American Chemical Society* **132**(13), 4822–4829 (2010).

[72] Kurushima, T., Gundiah, G., Shimomura, Y., Mikami, M., Kijima, N., and Cheetham, A. K. *Journal of The Electrochemical Society* **157**(3), J64–J68 (2010).

[73] Jacob, K. T., Verma, R., and Mallya, R. M. *Journal of Materials Science* **37**, 4465–4472 (2002).

[74] Tessier, F. and Marchand, R. *Journal of Alloys and Compounds* **262-263**(0), 410 – 415 (1997). Proceedings of the Twelfth International Conference on Solid Compounds of Transition Elements.

[75] Marchand, R., Tessier, F., Sauze, A. L., and Diot, N. *International Journal of Inorganic Materials* **3**(8), 1143 – 1146 (2001).

[76] Ebbinghaus, S. G., Aguiar, R., Weidenkaff, A., Gsell, S., and Reller, A. *Solid State Sciences* **10**(6), 709 – 716 (2008).

[77] Gal, Z. A., Mallinson, P. M., Orchard, H. J., and Clarke, S. J. *Inorganic Chemistry* **43**(13), 3998–4006 (2004). PMID: 15206881.

[78] Yamakawa, T., Tatami, J., Wakihara, T., Komeya, K., Meguro, T., MacKenzie, K. J. D., Takagi, S., and Yokouchi, M. *Journal of the American Ceramic Society* **89**(1), 171–175 (2006).

[79] Zeuner, M., Schmidt, P. J., and Schnick, W. *Chemistry of Materials* **21**(12), 2467–2473 (2009).

[80] Lange, H., Wötting, G., and Winter, G. *Angewandte Chemie International Edition English* **30**, 1579–1597 (1991).

[81] Senker, J., Jacobs, H., Müller, M., Press, W., Müller, P., Mayer, H. M., and Ibberson, R. M. *The Journal of Physical Chemistry B* **102**(6), 931–940 (1998).

[82] Yeh, C. and Chen, Y. *Ceramics International* **31**(5), 719 – 729 (2005).

[83] Gillan, E. G. and Kaner, R. B. *Inorganic Chemistry* **33**(25), 5693–5700 (1994).

[84] Hector, A. L. and Parkin, I. P. *Chemistry of Materials* **7**(9), 1728–1733 (1995).

[85] Bacon, P., Hou, J., Sleight, A., and Nielsen, R. *Journal of Solid State Chemistry* **119**(1), 207 – 209 (1995).

[86] Zou, G., Hu, B., Xiong, K., Li, H., Dong, C., Liang, J., and Qian, Y. *Applied Physics Letters* **86**(18), 181901 (2005).

[87] Sardar, K. and Rao, C. N. R. *Advanced Materials* **16**, 425–429 (2004).

[88] Gomathi, A., Reshma, S., and Rao, C. *Journal of Solid State Chemistry* **182**(1), 72 – 76 (2009).

[89] Greenwood, N. N. and Earnshaw, A. *Chemistry of the Elements*. (1986).

[90] Yamane, H., Shimada, M., Clarke, S. J., and DiSalvo, F. J. *Chemistry of Materials* **9**(2), 413–416 (1997).

[91] Piao, X., Machida, K.-I., Horikawa, T., and Hanzawa, H. *Journal of the Electrochemical Society* **155**(1), J17–J22 (2008).

[92] White, T., Ferraris, C., Kim, J., and Madhavi, S. *Reviews in Mineralogy and Geochemistry* **57**(1), 307–401 (2005).

[93] *Encyclopaedia Universalis (www.universalis-edu.com). (Articles "Os" and "Dents")* (Retrieved 08/12).

[94] White, T. J. and ZhiLi, D. *Acta Crystallographica Section B* **59**(1), 1–16 Feb (2003).

[95] William M. Yen, S. S. and Yamamoto, H., editors. *Phosphor Handbook - Second Edition*. CRC Press, (2007).

[96] Welker, T. *Journal of Luminescence* **48-49, Part 1**(0), 49 – 56 (1991).

[97] Lammers, M. J. J. and Blasse, G. *Journal of the Electrochemical Society* **134**, 2068–2072 (1987).

[98] Cui, Z.-F., Yuan, S.-L., Yang, Y.-X., Cheviré, F., Tessier, F., and Chen, G.-R. *Chinese Physics Letters* **28**(1), 014209 (2011).

[99] Ohnuki, T., Kozai, N., Samadfam, M., Yasuda, R., Yamamoto, S., Narumi, K., Naramoto, H., and Murakami, T. *Chemical Geology* **211**(1-2), 1 – 14 (2004).

[100] Smahi, A., Solhy, A., Badaoui, H. E., Amoukal, A., Tikad, A., Maizi, M., and Sebti, S. *Applied Catalysis A: General* **250**(1), 151 – 159 (2003).

[101] Harrison, J., Melville, A., Forsythe, J., Muddle, B., Trounson, A., Gross, K., and Mollard, R. *Biomaterials* **25**(20), 4977 – 4986 (2004).

[102] Karpov, A. S., Nuss, J., Jansen, M., Kazin, P. E., and Tretyakov, Y. D. *Solid State Sciences* **5**(9), 1277 – 1283 (2003).

[103] Nakayama, S., Aono, H., and Sadaoka, Y. *Chemistry Letters* **24**(6), 431–432 (1995).

[104] Nakayama, S. and Sakamoto, M. *Journal of the European Ceramic Society* **18**(10), 1413 – 1418 (1998).

[105] Sansom, J. E. H., Richings, D., and Slater, P. R. *Solid State Ionics* **139**, 205–210 (2001).

[106] Berastegui, P., Hull, S., Garcia, F. G., and Grins, J. *Journal of Solid State Chemistry* **168**(1), 294 – 305 (2002).

[107] Leon-Reina, L., Martin-Sedeño, M. C., Losilla, E. R., Cabeza, A., Martinez-Lara, M., Bruque, S., Marques, F. M. B., Sheptyakov, D. V., and Aranda, M. A. G. *Chemistry of Materials* **15**(10), 2099–2108 (2003).

[108] Jones, A., Slater, P. R., and Islam, M. S. *Chemistry of Materials* **20**(15), 5055–5060 (2008).

[109] Leon-Reina, L., Losilla, E. R., Martinez-Lara, M., Bruque, S., and Aranda, M. A. G. *Journal of Materials Chemistry* **14**, 1142–1149 (2004).

[110] Guillot, S. *Etude des paramètres principaux gouvernant les propriétés de conduction dans les apatites, électrolytes pour piles SOFC*. PhD thesis, Université de Lille, (September 29th 2009).

[111] Pramana, S. S., Klooster, W. T., and White, T. J. *Acta Crystallographica Section B* **63**(4), 597–602 (2007).

[112] Pramana, S. S., White, T. J., Schreyer, M. K., Ferraris, C., Slater, P. R., Orera, A., Bastow, T. J., Mangold, S., Doyle, S., Liu, T., Fajar, A., Srinivasan, M., and Baikie, T. *Dalton Transactions* , 8280–8291 (2009).

Chapter II:

Synthesis and crystal chemistry of rare-earth activated apatite oxynitrides

Chapter II: Synthesis and crystal chemistry of rare earth activated apatite oxynitrides

II.1. Synthesis of oxynitrido-silicates and -germanates with apatite structure

II.1.1. Introduction

Oxynitrides can be obtained by topotactic reactions starting from oxides with the appropriate crystal structure. Indeed, when nitrogen introduction only requires slight structural changes leading to weak energetic perturbations, oxynitride compounds can be obtained as metastable phases using soft conditions. For instance, perovskite oxynitrides have been widely studied and are commonly obtained by ammonolysis of oxide precursors at moderate temperatures [1] [2]. Pyrochlore oxynitrides have been obtained by topochemical nitriding of pyrochlore oxides [3] [4].

As previously discussed, oxidic apatites show a very flexible structure, suitable for topotactic anion substitution. Ammonolysis of lanthanum (strontium-substituted) silico and germano-apatites has been studied with the initial aim of testing their resistance as potential electrolytes in ammonia-fueled SOFCs [5] [6]. It was shown that after treating the oxide powder in flowing ammonia at 600°C, 800°C and 950°C for germanates, strontium-substituted lanthanum silicates and unsubstituted lanthanum silicates respectively, nitrogen was introduced then decreasing the ionic conductivity.

The need for new phosphors emitting at long wavelength with high efficiencies has already been discussed in chapter I. Many promising nitride phosphors (like $CaAlSiN_3$: Eu^{2+} or $MSiN_2$: Eu^{2+}) can only be synthesized in inert atmosphere or using special precursors and would not be suitable for high-scale industrial production. High-temperatures of synthesis also have to be avoided for cost and environmental reasons. Ammonolysis can be considered as a convenient route for industrial low-temperature synthesis process. Indeed, the related set-up generally involves a tubular furnace with flowing gas, a technology already existing in industries.

In this work, the treatment of precursor oxides with the required cationic ratios in NH_3 gas was used as the general convenient method to prepare new luminescent oxynitride materials at moderate temperatures. This allowed decreasing the temperature from 1600-1400 °C to 1100 °C with respect to the method generally used for the synthesis of luminescent

(oxy)nitride silicates, that is, the solid state reaction between oxides, nitrides and carbonates under N_2 or N_2/H_2 mixtures.

An alternative method by direct ammonolysis of a sol-gel precursor has also been investigated and is discussed in section II.1.4.2.

II.1.2. Stability and composition of silicate apatites

Unsubstituted lanthanum apatites and lanthanum alkaline-earth apatites show a wide range of possible compositions due to total anion content variability and the structural capacity to accommodate vacancies. The synthesis of precise stoichiometries can thus result difficult. Moreover, the phase diagram of La_2O_3-SiO_2 shows that the apatite phase exists in a narrow range of ratios La/Si, and that two stable silicates phases $La_2Si_2O_7$ and La_2SiO_5 may form as stable impurity phases. Many studies report the difficulty to synthesize apatite phases with high oxygen content, like $La_{10}Si_6O_{27}$ without formation of La_2SiO_5.

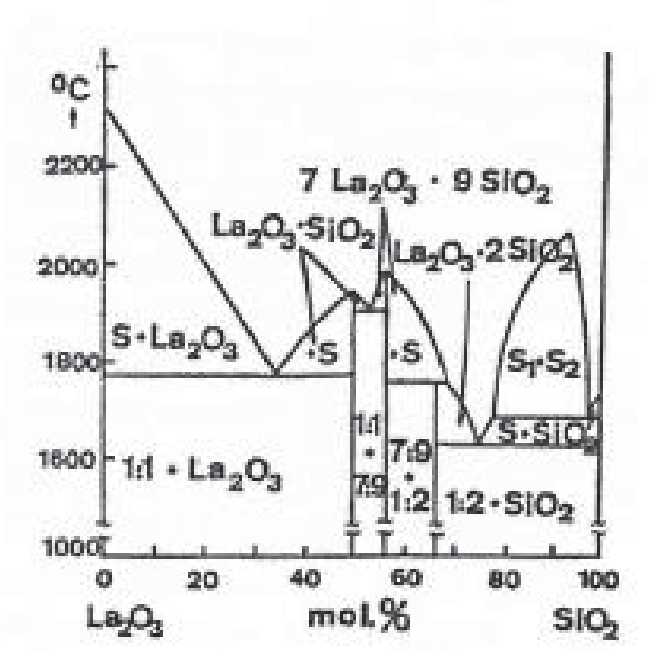

Figure II-1. Phase diagram of the system La_2O_3-SiO_2. Ratios 1:1, 7:9 and 1:2 correspond respectively to La_2SiO_5, $La_{9.33}Si_6O_{26}$ and $La_2Si_2O_7$. (Taken from [7])

II.1.3. Explored chemical compositions

The aim of this section is to describe the different compositions that have been studied in this work, and to explain the reasons why they have been chosen. The objective of this PhD

thesis was double: exploring a new host lattice for luminescent properties, and developing a convenient synthesis technique for producing oxynitride phosphors at low temperature. During the progress of this PhD thesis, efforts were made to synthesize the compound $SrSi_2O_2N_2$ by ammonolysis but remained unsuccessful. For the synthesis of apatite oxynitridosilicates and oxynitridogermanates different compositions have been explored:

- In order to check if the ammonolysis was a suitable method of synthesis of oxynitride phosphors, we used it for the preparation of the already reported blue emitting compound $La_5Si_3O_{12}N$: Ce^{3+} [8].

- The oxynitride $La_9SrSi_6O_{26.5-1.5y}N_y$, synthesized by ammonolysis, has been investigated as a potential host lattice for Ce^{3+} and Eu^{2+} doping. The optical properties of the resulting compounds have been studied and are described in chapter III.

- The germanate oxynitrides $La_{9.33+x}Ge_6N_yO_{26+1.5x-1.5y}$ and $La_{9.5}Sr_{0.5}Ge_6N_yO_{26.75-1.5y}$ were also investigated as potential host lattices for Ce^{3+} and Eu^{2+}. The optical properties of the resulting compounds have been studied and are described in chapter III.

- Precise investigation of optical properties required the synthesis of oxide compounds were the doping rare-earths are in their reduced form, *i.e.* with valence 3+ and 2+ for cerium and europium respectively. The oxidic analogous compounds of the investigated oxynitrides were thus synthesized by reduction in Ar/H_2 starting with the same oxide precursors.

- Undoped samples were also synthesized for comparison purposes.

- Potential impurities, doped with cerium and europium, have in some cases been synthesized for checking that their potential luminescent features were not actually falsely attributed to apatite phases.

II.1.4. Synthesis of oxidic apatite precursors

II.1.4.1. Ceramic method

Apatite oxide precursors were synthesized by solid-state reaction starting from stoichiometric mixture between La_2O_3 (Rhodia 99.99%), SiO_2 (Aldrich 99.995%) or GeO_2 (Aldrich 99.995%), $SrCO_3$ (Aldrich 99.9%), Eu_2O_3 (Rhodia 99.99%) or CeO_2 (Rhodia 99.995%). The purity of reactants was first checked by X-ray diffraction and thermogravimetric analysis. La_2O_3 is very hygroscopic and a large content of $La(OH)_3$ was

identified by X-ray diffraction (XRD). This reactant, together with SiO_2, was treated at 1000°C during fifteen hours for dehydration prior to any weighing. Powders were weighted immediately after this treatment. XRD of the reactants Eu_2O_3, CeO_2, GeO_2 and $SrCO_3$ showed no impurities. Thermogravimetric analyses (TGA) of the same compounds did not show any weight loss assignable to dehydration then these reactants were used as received. The weighed powders were thoroughly crushed and mixed in an agate mortar several times in order to obtain a precursor with homogenous precursor. The resulting powder was subsequently pelletized and treated in a muffle furnace.

Silicon apatite oxide precursors were synthesized by several treatments in air at temperatures ranging between 1300°C and 1450°C until the final phase was obtained, without any trace of the reactants in the XRD pattern (La_2O_3 or $La(OH)_3$ for instance). Intermediate regrinding and pelletizing was performed between the treatments.

Germanium apatite oxide precursors were synthesized by two treatments in air for 14 hours at 1100°C, with pelletizing and intermediate regrinding.

A non-negligible quantity of impurity which has been identified as La_2GeO_5 was obtained during the synthesis of some germanate samples. This phase doped with cerium has thus been synthesized alone in order to check its luminescence properties. The oxide was obtained with the same method than for germano-apatites and was ammonolyzed in the same conditions: 600 °C-20 h-660 ml/min.

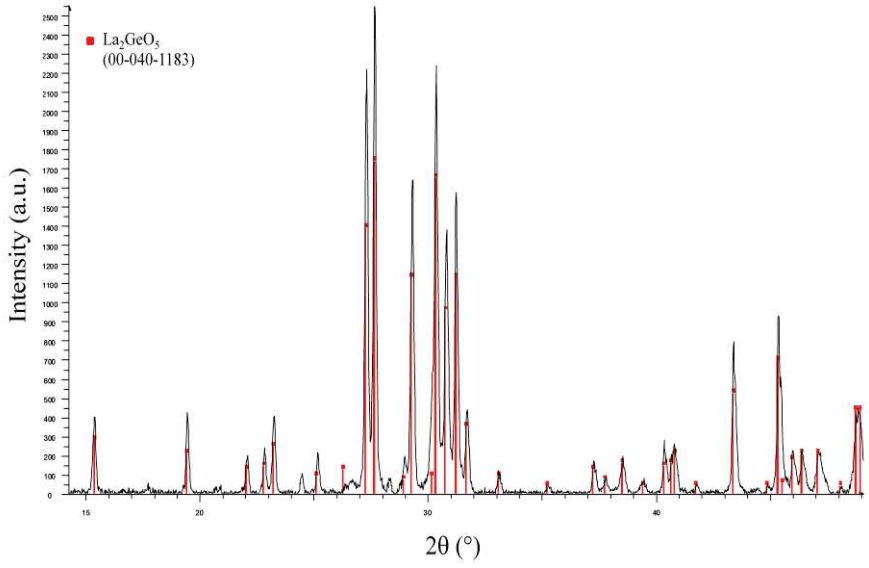

Figure II-2. X-ray diffraction pattern of $La_{1.98}Ce_{0.02}GeO_5$.

II.1.4.2. Sol-gel method

Following the objective of low temperature synthesis technique, an alternative method has also been explored: direct ammonolysis of a precursor made by Sol-Gel method. Sol-Gel methods can provide very reactive precursors for ammonolysis with good dispersion of cationic elements.

Hydrolysis-condensation of tetraethyl orthosilicate (TEOS) was used to produce a gel. In a typical synthesis, lanthanum, europium or cerium nitrate were introduced in a mixture of acetic acid and anhydrous ethanol. Nitrate precursors were analyzed by TGA before any weighing to determine their exact water content. After complete dissolution, TEOS was added and a gel formed after 1 hour, subsequently dried at 90°C. The following conditions, taken from [9] were used: acetic acid volume was fixed to twice the TEOS volume, and the concentration of silicon in solution was fixed to 0.9 $mol.L^{-1}$. After drying, the dried gel was calcined at 600°C during 4 hours.

II.1.5. Ammonolysis of oxidic apatites

Ammonolysis reactions were carried out by treating oxide powders in flowing $NH_{3(g)}$ (Carburos Metàlicos, 99.9%). Sintered alumina boats (Alsint, 99.7% Al_2O_3) were previously treated in order to eliminate superficial –OH groups. The furnace was a tubular split-type as shown in Figure II-2, using a reaction silica glass tube of dimensions 110 cm x 30 mm (inner diameter). Reaction temperatures ranged between 600°C and 1050°C, with flow of $NH_{3(g)}$ between 270 ml/min and 660 ml/min.

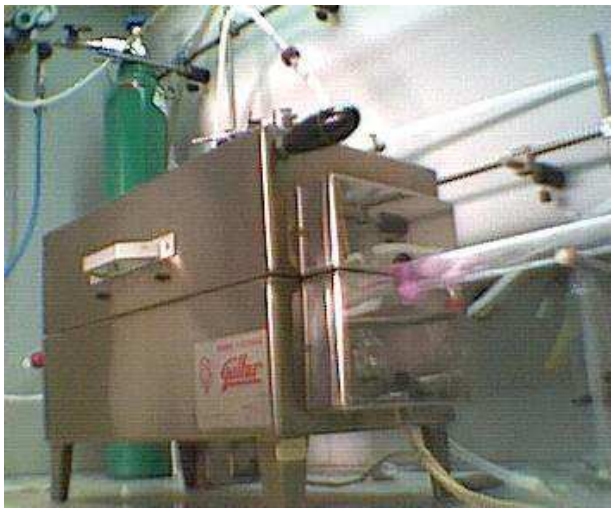

Figure II-3. Ammonolysis system at Solid State Chemistry Laboratory of ICMAB.

Due to the high toxicity of ammonia, it is necessary to check the air tightness of all the system before and during the synthesis. In addition to the risk of heating ammonia in presence of oxygen (Auto-ignition temperature: 651°C, Flammability limit in air: 16.5-26.8%), the affinity of the metals (La, Ce, Eu…) is higher for oxygen than for nitrogen. In conditions of ammonolysis, traces of oxygen are sufficient to react irreversibly with the sample, giving oxide impurities. It should be taken into account that important concentrations of H_2 may be present in the reaction tube at high temperatures since ammonia dissociates appreciably into H_2 and N_2 at temperatures higher than 500 °C.

Reduction under Ar/H_2 of the same oxide precursors have been carried out in parallel, in order to identify the luminescence modifications brought by the nitrogen introduction and not only by doping rare-earth reduction. Syntheses were carried out under flowing Ar/H_2 (Air liquide 90%/10% V/V, 99.999%) at 1000°C during 10 hours.

The oxidic apatite samples prepared by sol-gel were treated at 1050°C during 20 hours under ammonia flow rate of 270 ml/min. X-ray diffraction patterns (Figure II-4) showed that the apatite phase was obtained directly after this treatment. Analysis by scanning electron microscopy (SEM) showed that the average grain size was about 200 nm (Figure II-5). In conclusion, by using ammonolysis reactions of oxidic precursors we were able to stabilize the oxynitride apatite phase at significantly lower temperatures than used by the conventional solid state reaction of mixtures of Si_3N_4, La_2O_3 and rare-earth oxides under N_2/H_2 gas (usually between 1400 and 1600°C).

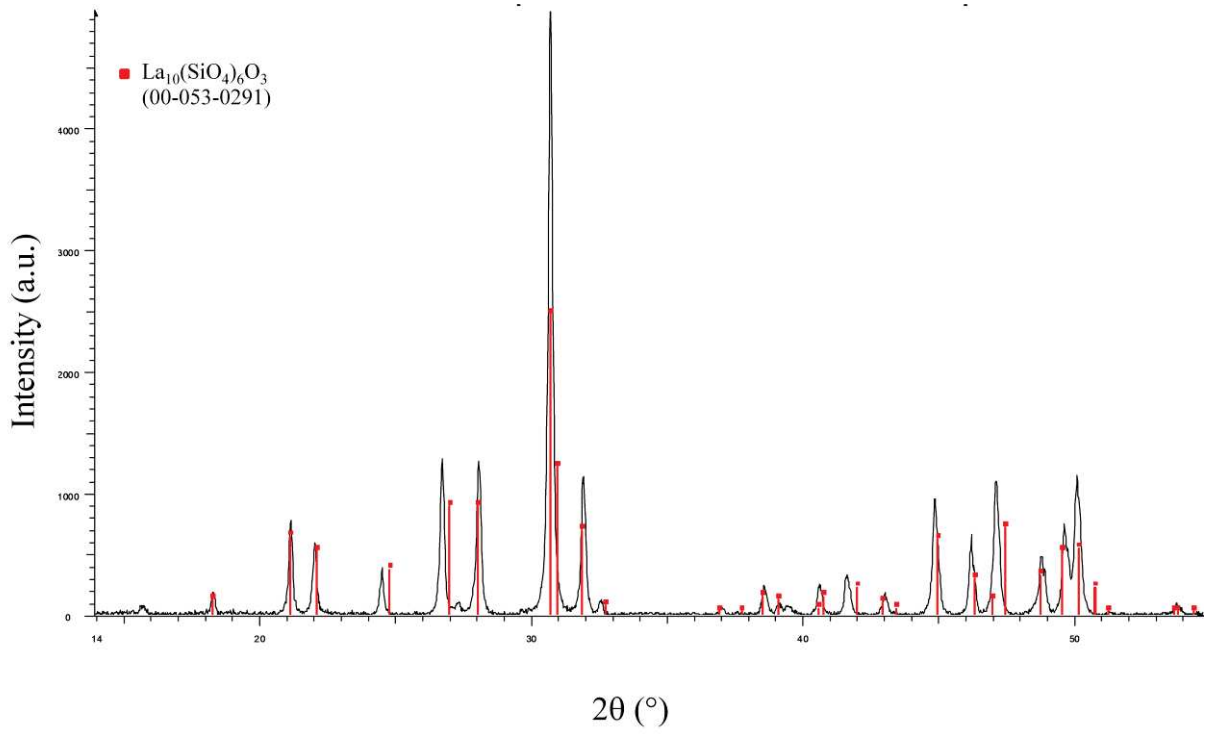

Figure II-4. X-ray diffraction pattern of $La_{10}Si_6O_{25.23}N_{1.18}$, prepared by ammonolysis of a sol-gel precursor.

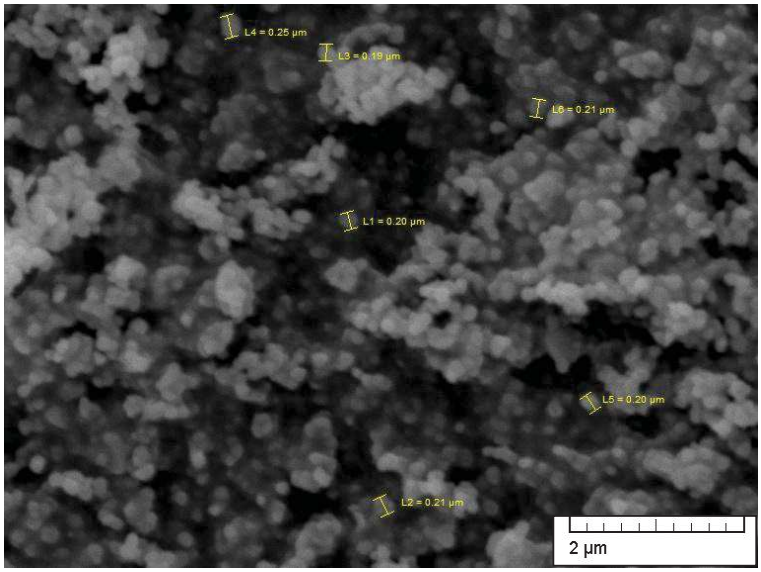

Figure II-5. Scanning electron microscopy image of $La_{10}Si_6O_{25.23}N_{1.18}$, prepared by ammonolysis of a sol-gel precursor.

Nevertheless, the samples obtained by this method showed very low emission intensities compared with those obtained from precursors prepared by solid-state-reaction. This could be due either to the small particle size that increases the number of absorption-reflexion steps in the material, or to the presence of unreacted amorphous silica between

grains. As a consequence, the method by solid-state reaction was selected for the synthesis of oxidic apatites.

II.1.6. Phase composition, thermal stability and microstructural characterization of the samples

II.1.6.1. X-ray powder diffraction

X-Ray powder diffraction was routinely used to study the phase composition of the samples as well as to determine the cell parameters of the oxynitridosilicate/oxynitridogermanate phases. The acquisition of X-ray patterns was carried out with two diffractometers: a Rigaku D/Max-RC and a Siemens D2000, both with Cu radiation Kα (λ = 1.5418 Å) and θ-2θ geometry. The 2θ range was between 5° and 100°, with 0.02° step, and a scanning speed of 1.2°/min. The PDF (Powder Diffraction File) database and DRXWin and Creafit programs have been used for phase analysis of the samples. Figure II-6 and II-7 show X-ray diffraction patterns of different samples after ammonolysis.

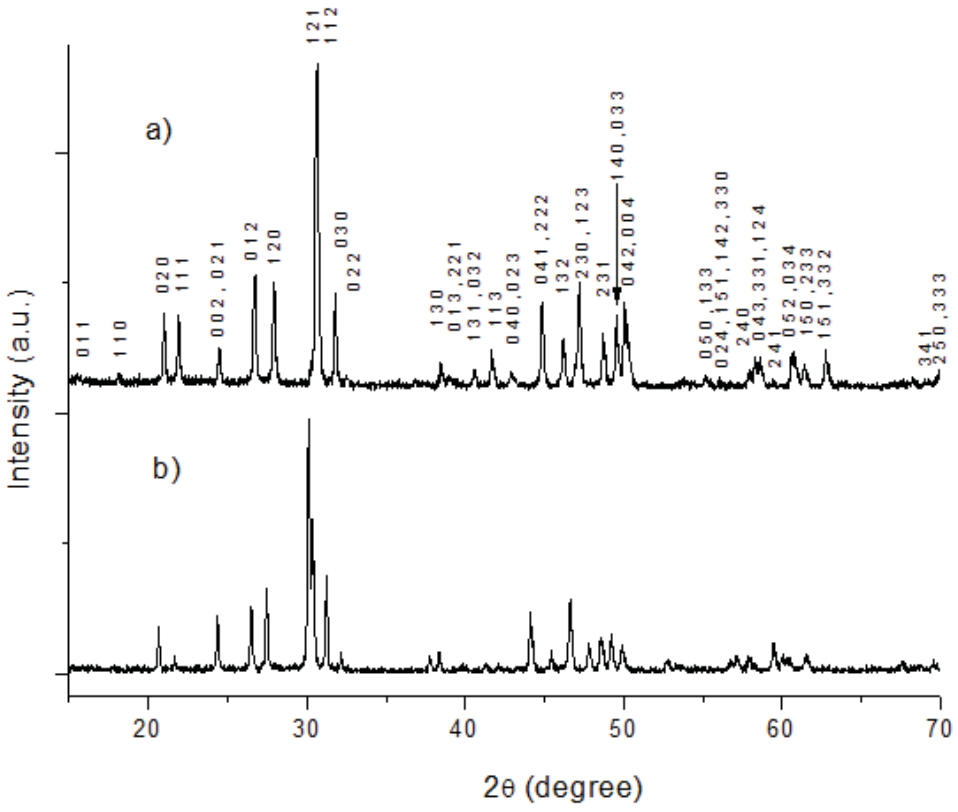

Figure II-6. X-ray powder diffraction patterns corresponding to europium substituted nitrided apatites, obtained from the precursors a) $La_9Sr_{0.9}Eu_{0.1}Si_6O_{26.55}$ and b) $La_{9.5}Sr_{0.4}Eu_{0.1}Ge_6O_{26.8}$ indexed in the space group $P6_3/m$.

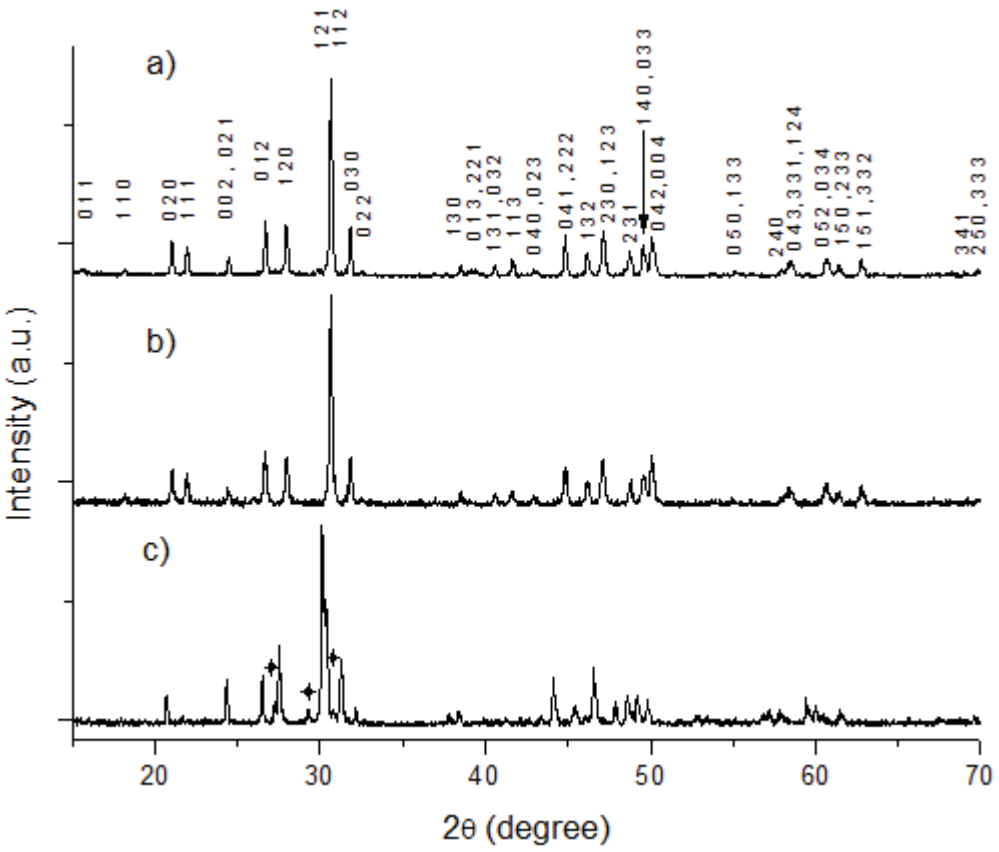

Figure II-7. X-ray powder diffraction patterns of the cerium doped oxynitridosilicates and germanates obtained by treatment in NH_3 of the oxyapatites with nominal compositions a) $La_{8.9}Ce_{0.1}SrSi_6O_{26.5}$, b) $La_{9.23}Ce_{0.1}Si_6O_{26}$ and c) $La_{9.9}Ce_{0.1}Ge_6O_{27}$. Peaks corresponding to La_2GeO_5 are indicated by crosses.

All the patterns except those of precursors of germanium compounds can be indexed in a hexagonal unit cell with dimensions a≈9.7 Å and c≈7.2 Å and symmetry $P6_3/m$ characteristic of the apatite structure. The observed 2θ positions and relative intensities of reflections were close to those reported for $La_{9.33}Si_6O_{26}$ (ICDD PDF file 490443). $La_{9.9}Ce_{0.1}Ge_6O_{27}$ is triclinic and change to hexagonal symmetry after treatment in NH_3 at 600 °C (Figure II-9) as it was previously in [5]. Lanthanum strontium silicoapatites showed no evolution before and after heat treatment in flowing $NH_{3(g)}$. As previously reported [6], anisotropic peak broadening could be observed after ammonolysis (Figure II-8). Traces amount of strontium have been found in the $La_{9.9}Ce_{0.1}Ge_6O_{27}$ phase by Inductively Coupled Plasma – Atomic Emission Spectroscopy.

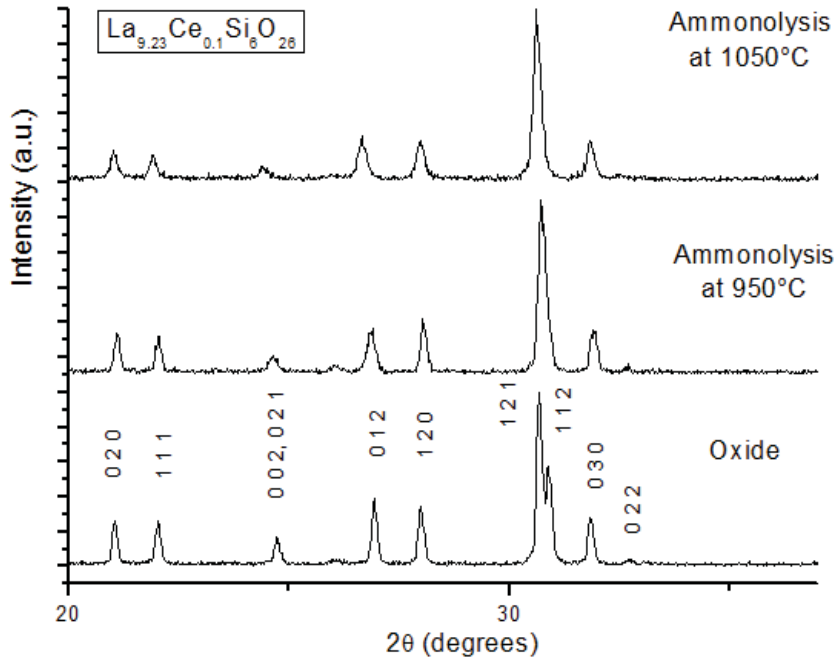

Figure II-8. X-ray diffraction patterns of $La_{9.23}Ce_{0.1}Si_6O_{26}$ before and after ammonolysis at 950 °C and 1050 °C.

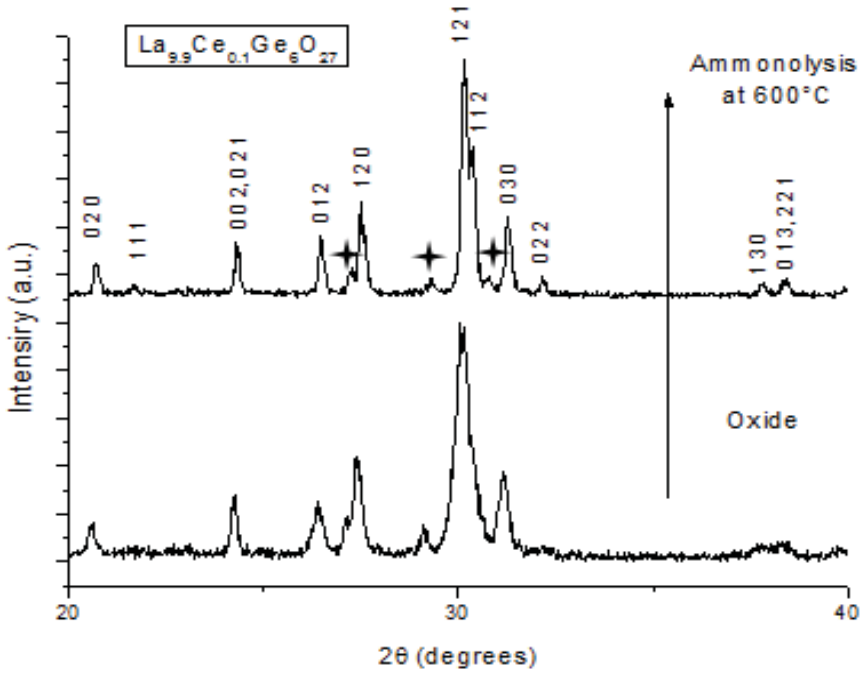

Figure II-9. X-ray diffraction pattern of $La_{9.9}Ce_{0.1}Ge_6O_{27}$ before and after ammonolysis at 600°C. Peaks corresponding to La_2GeO_5 are indicated by crosses.

II.1.6.2. Thermogravimetric analysis

Oxynitrides are not stable in air at high temperature as they decompose to form oxides. The lower free energies of formation of nitrides with respect to oxides are a consequence of the high bond energy of the N_2 molecule compared with O_2 and the large electron affinity of nitrogen with respect to oxygen. Determination of the nitrogen contents and thermal stabilities was performed by using a TG/DSC NETZSCH STA 449 F1 Jupiter thermal analysis system while heating up to 1400 °C using heating rates of 5 and 10 °C/min under flowing O_2.

Heating in oxygen the oxynitride samples leads to a weight increase as a result of oxidation of Eu^{2+} and Ce^{3+} and to the substitution of N by O. Results were generally close to those previously reported for undoped nitrided apatites [5] [6]. An example of the obtained curve coupled with Differential Scanning Calorimetry (DSC) is shown in Figure II-10. The weight gain observed is concomitant with an exothermic peak.

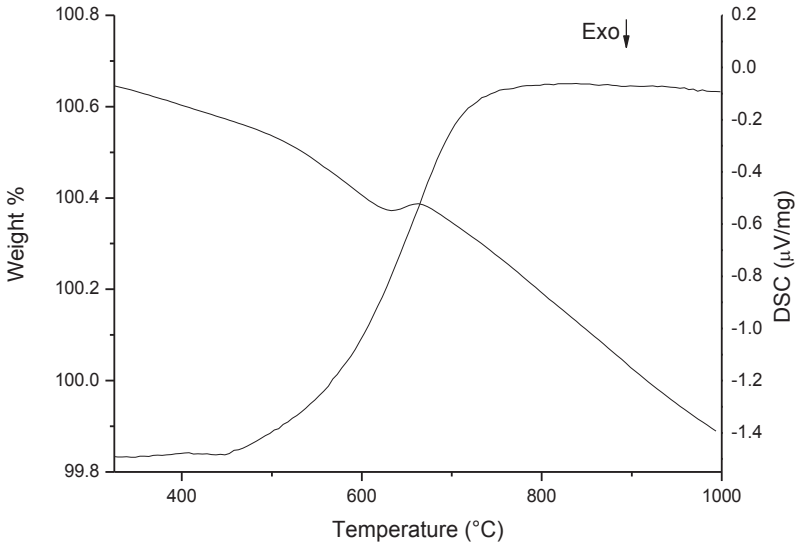

Figure II-10. TGA and DSC curve for $La_9Sr_{0.9}Eu_{0.1}Si_6N_{1.77}O_{23.85}$.

Figure II-11 shows TGA obtained for silicates and germanates ammonolysed at different temperatures. The silicon apatite oxynitride samples begin to decompose into the corresponding oxides at c.a. 500°C (T onset). For some germanium samples the oxidation takes place in two steps, starting at 250°C and 500°C (T onset) respectively. The weight increases up to a maximum and remains constant for temperatures higher than 800°C. In some samples the decomposition continued at temperatures above 1000°C. This behavior is typical

for many oxynitrides and is due to the substitution of nitrogen by oxygen to give the corresponding oxides. The observation of two steps in some germanium samples may be related with the existence of the two types of anions in the apatite structure, placed at the channel sites and the BX_4 tetrahedra. As germanium is slightly more electronegative than silicon the covalency of Ge-N bond is higher than for Si-N. As a consequence the differences of stability between the BX_4 tetrahedra and the channel sites should be more important for the germanates then leading to the observation of two steps in the decomposition into the oxidic apatites. Nitride anions at the channel site should be easier to remove than those bonded to the B atoms. The low temperature step would correspond to the substitution of channel nitrides by oxides whereas the step with onset at 500°C would correspond to the substitution of nitrogen atoms at the BX_4 tetrahedra. Following this hypothesis in germanates nitrogen would be positioned in both channel sites and BX_4, with a larger occupancy of the tetrahedral sites.

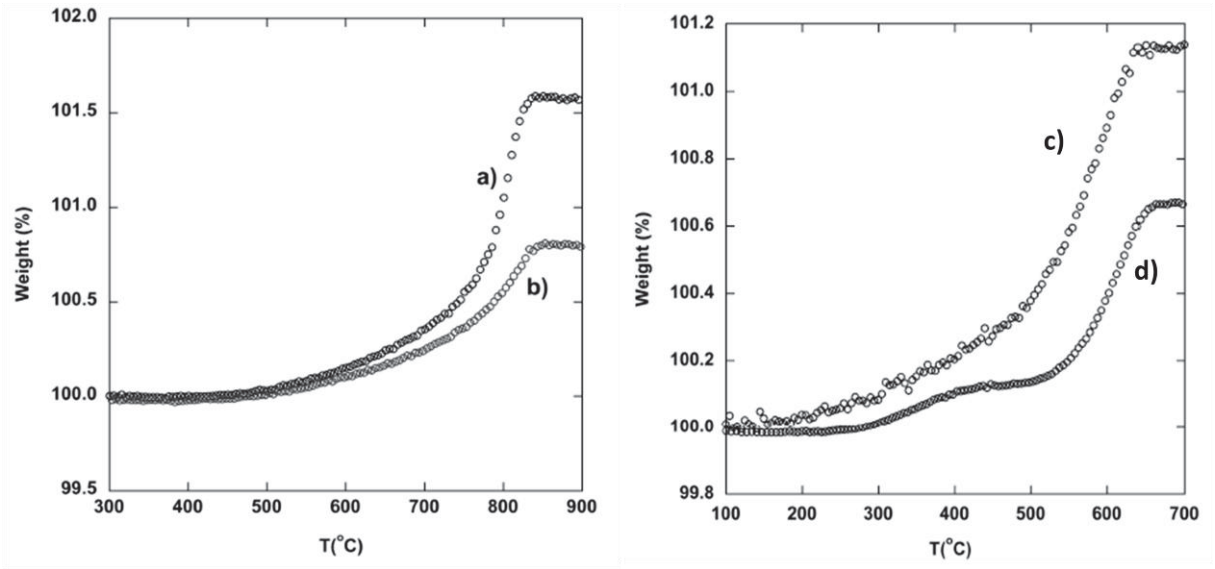

Figure II-11. Examples of thermogravimetric analyses in $O_{2(g)}$. a) $La_{9.23}Ce_{0.1}Si_6N_{2.85}O_{21.72}$, b) $La_{9.23}Ce_{0.1}Si_6N_{1.50}O_{23.75}$, c) $La_{9.9}Ce_{0.1}Ge_6N_{2.46}O_{23.31}$ and d) $La_{9.23}Ce_{0.1}Ge_6N_{1.55}O_{23.67}$.

Some samples showed loss of water and carbon dioxide at around 300°C. Lanthanum silico-apatite structure has been proved to be able to incorporate water in its structure [10] [11].

The nitrogen content was determined by considering the increase in mass of the sample while heating in O_2. Because the rare-earth cations are reduced during the ammonolysis, their oxidation has to be taken in account when determining the nitrogen content. The following formula was used:

$$y = \frac{(m_2 - m_1)M_{0xide}}{m_2 * (M_N - 1.5\ M_O)} - \frac{x/2 * M_O}{M_N - 1.5\ M_O}$$

With y the nitrogen content per formula, m_1 and m_2 are the initial and final masses respectively, M_{Oxide} is the molar weight of the final obtained oxide and x the rare-earth doping content per formula.

Table II-1. Nitrogen contents determined by TGA in O_2 for the investigated apatite oxynitrides.

Starting oxide compound	Synthesis conditions (Temperature-Duration-Ammonia Flow)	Nitrogen quantity y (mole per formula)
$La_{9.23}Ce_{0.1}Si_6O_{26}$	950 °C -20 h-270 ml/min	1.41
$La_{9.23}Ce_{0.1}Si_6O_{26}$	1050 °C-20 h-270 ml/min	2.85
$La_9Sr_{0.9}Eu_{0.1}Si_6O_{26.55}$	800 °C-20 h-350 ml/min	0.60
$La_9Sr_{0.9}Eu_{0.1}Si_6O_{26.55}$	1050 °C-20 h-660 ml/min	1.77
$La_{8.9}Ce_{0.1}SrSi_6O_{26.5}$	800 °C-20 h-350 ml/min	0.37
$La_{8.9}Ce_{0.1}SrSi_6O_{26.5}$	1050 °C-20 h-660 ml/min	1.06
$La_9Ba_{0.9}Eu_{0.1}Si_6O_{26.55}$	800 °C-20 h-350 ml/min	0.59
$La_9Ca_{0.9}Eu_{0.1}Si_6O_{26.55}$	800 °C-20 h-350 ml/min	0.57
$La_{9.23}Ce_{0.1}Ge_6O_{26}$	600 °C-20 h-660 ml/min	1.56
$La_{9.9}Ce_{0.1}Ge_6O_{27}$	600 °C-20 h-660 ml/min	2.46
$La_{9.5}Sr_{0.4}Eu_{0.1}Ge_6O_{26.8}$	600 °C-20 h-660 ml/min	1.42

TGA results for the investigated compositions are given in table II-1. Several tendencies can be observed. First of all, for a constant reaction time the nitrogen content increases with the temperature of ammonolysis. In order to investigate the influence of the other synthesis parameters on the nitrogen stoichiometry, another set of ammonolysis reactions were performed starting with the same oxidic precursor sample. In experiments performed for a starting sample with composition $La_{8.9}Ce_{0.1}SrSi_6O_{26.5}$, the nitrogen content changed with the reaction time (t). At 1050°C and flow rate of 350 ml/min the nitrogen content was 0.24 for t=5 hours and 2.24 for t=12h, showing that equilibrium is reached slowly at a given flow rate. Increasing the flow rate and temperature increased the nitrogen uptake. In

samples treated at 1050°C for 5 hours, the obtained nitrogen content was 2.41 when using a flow rate of 660 ml/min. For a same duration t=12 hours, with T=800°C and a flow rate of 660 mL/min, the nitrogen uptake was 0.22, in contrast with 2.24 obtained at T=1050°C with a flow rate of 350 mL/min.

The cationic stoichiometry of the apatite oxidic precursor has an influence on the nitrogen content of the corresponding oxynitride. Pure rare earth apatite oxides incorporated more nitrogen than the corresponding alkaline-earth substituted precursors at similar temperatures. Another observed trend is that pure rare-earth apatites with a higher cationic content (*e.g.* $La_{9.9}Ce_{0.1}Ge_6O_{27}$ compared with $La_{9.23}Ce_{0.1}Ge_6O_{26}$) showed higher nitrogen contents after ammonolysis. Both trends can be related with the quantity of excess oxygen in the precursor apatite that showed to be correlated with the nitrogen content in the oxynitride. The higher the quantity of excess oxygen in the precursor, the higher is the nitrogen content after ammonolysis. In contrast, variation of the alkaline-earth nature (Ca, Sr, Ba) for a given alkaline-earth/lanthanum ratio (*ie* a given oxygen excess content in starting oxide precursor) had no influence on the final nitrogen uptake.

II.1.6.3. Combustion Analysis

TGA measurements under flowing O_2 have been used as a general method to determine nitrogen content in our compounds. Nevertheless, combustion analyses have also been carried out on a set of compounds (Table II-2). Elemental analyses of nitrogen contents were performed on a Thermo Fisher Scientific EA 1108 instruments. Nitrogen contents found by these analyses were below those obtained by TGA, but followed the same trend described in the previous section.

Table II-2. Comparison between nitrogen content determined by TGA and elemental analysis

Starting oxide and ammonolysis conditions	Nitrogen content y determined by Elemental Analysis (mole per formula)	Nitrogen content y determined by Thermo-Gravimetric Analysis (mole per formula)
$La_{9.23}Ce_{0.1}Si_6O_{26}$ 950 °C-20 h-270 ml/min	0.69	1.41
$La_{9.23}Ce_{0.1}Si_6O_{26}$ 1050 °C-20 h-270 ml/min	1.49	2.85
$La_9Sr_{0.9}Eu_{0.1}Si_6O_{26.55}$ 800 °C-20 h-350 ml/min	0.30	0.60
$La_9Sr_{0.9}Eu_{0.1}Si_6O_{26.55}$ 1050 °C-20 h-660 ml/min	0.85	1.77
$La_{8.9}Ce_{0.1}SrSi_6O_{26.5}$ 800 °C-20 h-350 ml/min	0.30	0.37
$La_{8.9}Ce_{0.1}SrSi_6O_{26.5}$ 1050 °C-20 h-660 ml/min	0.64	1.06
$La_{9.23}Ce_{0.1}Ge_6O_{26}$ 600 °C-20 h-660 ml/min	0.77	1.56
$La_{9.9}Ce_{0.1}Ge_6O_{27}$ 600 °C-20 h-660 ml/min	1.01	2.46
$La_{9.5}Sr_{0.4}Eu_{0.1}Ge_6O_{26.8}$ 600 °C-20 h-660 ml/min	1.00	1.42

The possible source of errors in the elemental analysis results is the high temperature of decomposition of the oxynitrides that may cause incomplete combustion in the analyzer that operates at 1000 °C. In the TGA experiments some samples continued to decompose in flowing oxygen at temperatures well above 1000 °C.

II.1.6.4. Scanning Electron Microscopy

Grain sizes of the samples were investigated by scanning electron microscopy. Similar particle size distribution between 2 and 30 microns were observed for all oxynitride samples without significant differences with respect to the precursor oxidic apatites. Ammonolysis at different temperatures did not affect the particle sizes that were caused by the higher temperatures used for the synthesis of the precursors.

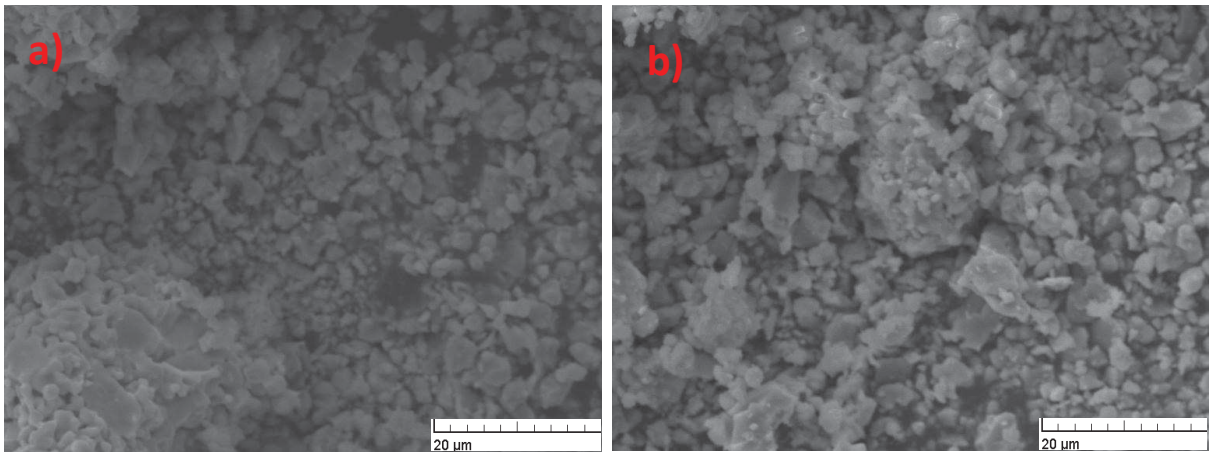

Figure II-12. Scanning electron microscopy images for $La_9Sr_{0.9}Eu_{0.1}Si_6O_{26.5}$ before (a)), and after (b)) ammonolysis at 800 °C-20 h-350 ml/min.

II.2. Structural characterization of oxynitridosilicates and oxynitridogermanates

II.2.1. Introduction

The introduction of nitrogen into a host lattice may have an important effect on the local environment of the cations. Two positions can be considered for nitrogen atoms in the apatite structure: substituting oxygen atoms in channel positions or in the silicon tetrahedra. Channels inside the apatite structure and more especially in the case of lanthanum silico-apatites have proven to be able to accommodate different anions. On the other side, while considering the second Pauling rule [12], which states that: "*In a stable coordination structure the electric charge of each anion tends to compensate the strength of the electrostatic valence bonds reaching to it from the cations at the centres of the polyhedral of which it forms a corner*", the channel anionic position is the one which provides the lowest total bond strength, making difficult the compensation of the higher nitrogen formal charge.

The first example of nitrided apatite was $Sm_{10}Si_6N_2O_{24}$ reported by Gaudé *et al* [13]. In the determination of the crystal structure from X-ray powder diffraction data using the space group $P6_3$ the nitrogen atoms were suggested to occupy the silicon tetrahedra sites because this led to more similar thermal parameters for anion sites. Later, oxynitride apatites containing transition metals with high oxidation states as V^{5+} and Ti^{4+} and showing nitrogen content higher than two moles per formula were investigated by Guyader *et al* [14]. Nitrogen contents as high as 4.7 moles per formula were obtained. Such high nitrogen content is not compatible with nitrogen atoms being only in channel position. Nevertheless no neutron diffraction study was carried out. These samples were synthesized by solid-state reaction between rare-earth oxides, SiO_2 and Si_3N_4. The method of synthesis and the cooling rates may have an influence on the distribution of anions. Samples prepared at high temperatures by solid state reaction may show different anion contents and distributions than those prepared by ammonolysis of oxidic apatites.

Strontium substituted and strontium free lanthanum silicon or germanium oxynitride apatites have been recently investigated by Slater et al [5] [6] following growing interest in the use of ammonia as a fuel in solid oxide fuel cells. They can be formulated as solid solutions $La_{8+x}Sr_{2-x}T_6O_{26-x/2-3/2y}N_y$ (T= Si, Ge) with nitrogen contents up to y=2. For the strontium free silicon compound some lanthanum deficiency has been observed (La/Si= 9.33/6) as well as higher nitrogen contents, up to y=3. The structure of these oxynitrides is formed by isolated $[TX_4]$ (T= Si, Ge) tetrahedra and 7^{th} or 9^{th}-coordinated strontium and lanthanum cations that are bonded to the anions of the tetrahedra and to the free channel anions. Nitrogen atoms may occupy either the channel sites or the positions at the SiX_4 or GeX_4 tetrahedra.

For the unsubstituted apatite of formula $La_{9.33}Si_6O_{26}$, nitrogen was found both in the channels and silicon tetrahedra notably by Rietveld refinement of neutron diffraction pattern [6]. For $La_{8+x}Sr_{2-x}(Si/Ge)_6O_{26+x/2}$, a correlation was found between the interstitial oxygen content (determined by the alkaline-earth substitution rate) and the quantity of nitrogen incorporated [5]. This lead to suggest a mechanism of replacement of three oxygen atoms by two nitrogen atoms in the channel sites with suppression of the interstitial position (Figure II-13).

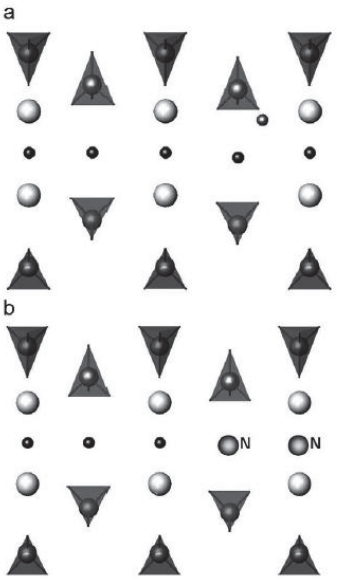

Figure II-13. Suggested substitution at anion sites for nitrogen introduction into the lanthanum apatite structure. a) Oxidic apatite b) Oxynitride apatite were two nitrogen atoms replaced three oxygen atoms including the interstitial site. Figure reproduced from reference [5].

In this work, we have characterized the crystal structures of the oxynitride apatites by electron diffraction, X-ray diffraction and neutron diffraction. The homogeneity of nitrogen compositions has been studied by Auger electron spectroscopy and electron microprobe. The local environment of silicon atoms has been investigated by infrared spectroscopy and Raman spectroscopy.

II.2.2. Cell parameters

Cell parameters were determined by Le Bail fitting using FullProf [15] (Table II-3 and II-4) and the space group $P6_3/m$ (n°176), except for oxide germanates that were investigated using the space group $P\bar{1}$ (n°2). According to the differences in the ionic radii of N^{3-} and O^{2-} (r N^{3-}=1.46 Å; r O^{2-}=1.38 Å for C.N.=4 [16]) the introduction of nitrogen should lead to an increase of the cell parameters. However these may be affected by other factors such as the formation of anion vacancies, which is concomitant to the substitution of oxygen by nitrogen, and the reduction of Eu^{3+} to Eu^{2+}. Reduction of cations, as nitriding, would increase the cell parameters whereas the formation of anion vacancies would have an opposite effect.

Reduction of Eu^{3+} in Eu^{2+} leads indeed to an increase of both cell parameters for $La_9Sr_{0.9}Eu_{0.1}Si_6O_{26.5}$ before and after reduction under Ar/H_2. We observed a clear increase in parameters a and c with increasing nitrogen content for lanthanum strontium-substituted silicoapatites. More generally, for all compounds, the c parameter is particularly impacted by nitrogen introduction and increases. In conclusion, the effect of anion vacancies creation seems overcompensated in our case by both the effect of higher nitrogen radius and doping rare-earth reduction. A similar behaviour has been reported for nitrided ceria obtained by treatment of CeO_2 in NH_3. For the solid solution $Ce^{4+}_{1-y}Ce^{3+}_yO_{2-3x/2-y/2}N_xV_{(x+y)/2}$ a linear correlation of the cubic lattice parameter with a combination of two variables, the nitrogen content and the concentration of Ce^{3+}, [17] was observed. Increasing the size of the alkaline-earth ion increased drastically both cell parameters.

Table II-3. Cell parameters obtained by Le Bail fitting of powder X-ray diffraction data for oxide and oxynitride lanthanum strontium silicon apatites obtained in different conditions. For nitrided and reduced samples the treatment temperature of the precursors is indicated.

Compound	***Synthesis conditions***	***a (Å)***	***c (Å)***
$\mathbf{La_9Sr_{0.9}Eu_{0.1}Si_6O_{26.55}}$	air(precursor)	9.6958(8)	7.2035(11)
$\mathbf{La_9Sr_{0.9}Eu_{0.1}Si_6O_{26.5}}$	Ar/H_2/1000 °C	9.7051(2)	7.2137(3)
$\mathbf{La_9Ca_{0.9}Eu_{0.1}Si_6N_{0.57}O_{25.64}}$	NH_3/800 °C	9.6777(6)	7.1877(5)
$\mathbf{La_9Sr_{0.9}Eu_{0.1}Si_6N_{0.60}O_{25.6}}$	NH_3/800 °C	9.7031(12)	7.2279(14)
$\mathbf{La_9Ba_{0.9}Eu_{0.1}Si_6N_{0.59}O_{25.61}}$	NH_3/800 °C	9.7355(2)	7.2711(2)
$\mathbf{La_9Sr_{0.9}Eu_{0.1}Si_6N_{1.77}O_{23.85}}$	NH_3/1050 °C	9.7107(16)	7.2460(19)
$\mathbf{La_{8.9}Ce_{0.1}SrSi_6O_{26.5}}$	air(precursor)	9.7037(5)	7.2137(7)
$\mathbf{La_{8.9}Ce_{0.1}SrSi_6O_{26.5}}$	Ar/H_2/1000 °C	9.7007(3)	7.2130(4)
$\mathbf{La_{8.9}Ce_{0.1}SrSi_6N_{0.37}O_{25.95}}$	NH_3/800 °C	9.7068(5)	7.2314(6)
$\mathbf{La_{8.9}Ce_{0.1}SrSi_6N_{1.06}O_{24.91}}$	NH_3/1050 °C	9.7086(4)	7.2465(6)
$\mathbf{La_{9.23}Ce_{0.1}Si_6O_{26}}$	air(precursor)	9.7172(4)	7.1829(5)
$\mathbf{La_{9.23}Ce_{0.1}Si_6N_{2.85}O_{21.72}}$	NH_3/1050 °C	9.6969(7)	7.2452(11)

Table II-4. Cell parameters obtained by Le Bail fitting of powder X-ray diffraction data for oxide and oxynitride lanthanum strontium germanium apatites obtained in different conditions. For nitrided and reduced samples the treatment temperature of the precursors is indicated.

Compound	***Synthesis conditions***	***a (Å)***	***b (Å)***	***c (Å)***
$\mathbf{La_{9.5}Sr_{0.4}Eu_{0.1}Ge_6O_{26.8}}$	air(precursor)	9.8831(14)	9.6803(18)	7.299(3)
$\mathbf{La_{9.5}Sr_{0.4}Eu_{0.1}Ge_6N_{1.42}O_{24.62}}$	NH_3/600 ^oC	9.9049(5)		7.2991(6)
$\mathbf{La_{9.9}Ce_{0.1}Ge_6O_{27}}$	air(precursor)	9.9416(18)	9.9183(15)	7.3153(14)
$\mathbf{La_{9.9}Ce_{0.1}Ge_6N_{2.46}O_{23.31}}$	NH_3/600 ^oC	9.9110(5)		7.3202(7)

The refined angles for the germanium oxidic precursors were: $La_{9.9}Ce_{0.1}Ge_6O_{27}$, α= 90.869(17)^o, β=88.138(19)^o, γ=120.835(14)^o; $La_{9.5}Sr_{0.4}Eu_{0.1}Ge_6O_{26.8}$: α=92.16(2) ^{o}, β=89.08(2) ^{o}, γ=119.665(16) ^{o}.

II.2.3. Electron diffraction

Electron diffraction micrographs were obtained in a JEOL 1210 transmission electron microscope operating at 120 kV, equipped with a side-entry 60/30^o double tilt GATHAN 646 specimen holder. The samples were prepared by dispersing the powders in ethanol and depositing of a droplet of this suspension on a carbon coated holey film supported on a copper grid.

The electron diffraction patterns along the [001] and [100] zone axes of a representative crystal of the sample $La_{9.9}Ce_{0.1}Ge_6\ N_{2.46}O_{23.31}$ are shown in Figure II-14. The reconstruction of the reciprocal lattice by tilting around the c* axis led to the extinction condition 00l, l=2n compatible with the space groups $P6_3$ and $P6_3/m$. No extra reflections or superstructures that could be indicative of anion ordering were observed in these patterns.

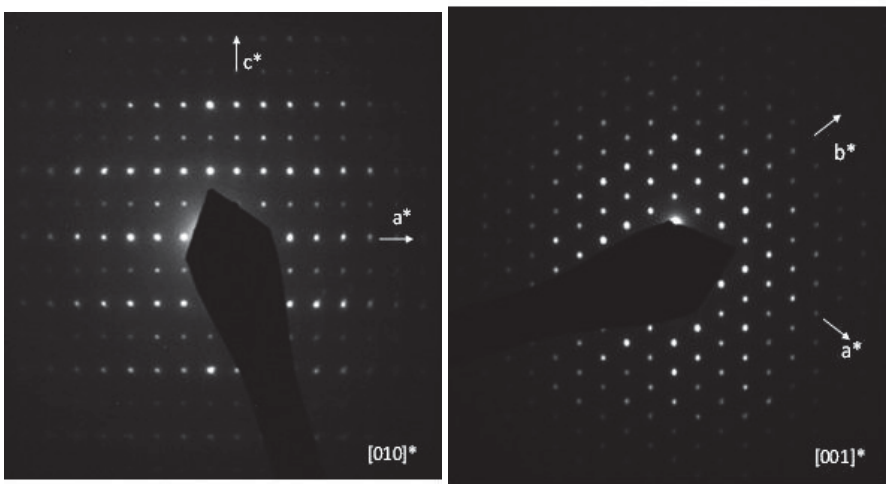

Figure II-14. Electron diffraction planes along [001]* (bottom) and [100]* zone axes (top) of $La_{9.9}Ce_{0.1}Ge_6N_{2.46}O_{23.31}$.

II.2.4. Rietveld refinement

II.2.4.1. X-ray diffraction

Rietveld refinement of the crystal structure of the compound $La_{8.9}Ce_{0.1}SrSi_6N_{1.06}O_{24.91}$ from X-ray diffraction data was performed in the space group $P6_3/m$ using the atomic coordinates of $La_8Sr_2Si_6O_{26}$ as starting model [18]. The composition of the compound was fixed to $La_{8.9}Ce_{0.1}SrSi_6NO_{25}$. As X-rays do not provide enough contrast to distinguish between the two anions, nitrogen was positioned statistically over the four anion sites of the apatite structure with fixed occupancies. Variation of occupancies in 6h sites gave no Sr content. So strontium atoms were positioned at 4f sites. Cerium was distributed statistically between 4f and 6h sites. The refined structure showed bond distances very close to those of $La_8Sr_2Si_6O_{26}$ from neutron diffraction data [18].

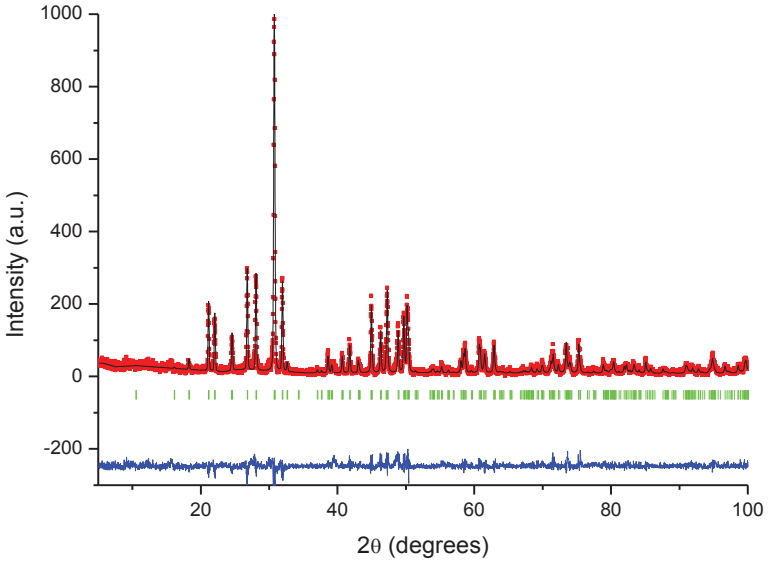

Figure II-15. Observed (Red), calculated (Black) and difference (Blue) X-ray diffraction profile for $La_{8.9}Ce_{0.1}SrSi_6N_{1.06}O_{24.91}$.

Table II-5. Rietveld refinement parameters for $La_{8.9}Ce_{0.1}SrSi_6NO_{25}$

Compound			
Space group	$P6_3/m$ (Nº 176), Z=1		
a(Å)	9.7008(4)		
c(Å)	7.2401(4)		
Cell volume	590.06		
Calculated density	5.459		
N_p, N_{refl}, N_{irefl}	4750	502	252
P_p, P_i, P_g	5	13	10
R_{Bragg}, R_F, χ	13.2	11.5	11.70
R_p, R_{wp} , R_{exp}	33.2	36.8	28.17

Table II-6. Final refined structural parameters for $La_{8.9}Ce_{0.1}SrSi_6NO_{25}$

Atom	Wyckof site	x/a	y/b	z/c	occ. factor	B iso
La(1)	4f	0.33330	0.66670	-0.00321(15)	0.493	0.500
Sr(1)	4f	0.33330	0.66670	-0.00321(15)	0.167	0.500
Ce(1)	4f	0.33330	0.66670	-0.00321(15)	0.007	0.500
La(2)	6h	0.0121(7)	0.2449(5)	0.25000	0.990	0.500
Ce(2)	6h	0.0121(7)	0.2449(5)	0.25000	0.110	0.500
Si	6h	0.403(2)	0.377(3)	0.25000	1.000	0.500
O(1)	6h	0.329(5)	0.479(5)	0.25000	0.962	0.500
N(1)	6h	0.329(5)	0.479(5)	0.25000	0.038	0.500
O(2)	6h	0.597(5)	0.473(5)	0.25000	0.962	0.500
N(2)	6h	0.597(5)	0.473(5)	0.25000	0.038	0.500
O(3)	12i	0.342(3)	0.261(3)	0.072(4)	1.922	0.500
N(3)	12i	0.342(3)	0.261(3)	0.072(4)	0.077	0.500
O(4)	2a	0.00000	0.00000	0.25000	0.320	0.500
N(4)	2a	0.00000	0.00000	0.25000	0.013	0.500

Table II-7. Selected interatomic distances (Å) for $La_{8.9}Ce_{0.1}SrSi_6NO_{25}$

Bond	Bond distances (Å)
d (La1/Sr1/Ce1-O(1)/N(1)) (x3)	2.57(4)
d (La1/Sr1/Ce1-O(2)/N(2)) (x3)	2.53(4)
d (La1/Sr1/Ce1-O(3)/N(3)) (x3)	2.91(3)
d(La2/Ce2-O(1)/N(1))	2.76(4)
d(La2/Ce2-O(2)/N(2))	2.47(6)
d(La2/Ce2-O(3)/N(3)) (x2)	2.48(3)
d(La2/Ce2-O(3)/N(3)) (x2)	2.64(3)
d(La2/Ce2-O(4)/N(4))	2.319(6)
d(Si-O(1)/N(1))	1.48(7)
d(Si-O(2)/N(2))	1.63(5)
d(Si-O(3)/N(3)) (x2)	1.62(3)

II.2.4.2. Neutron diffraction measurements

The neutron diffraction pattern of $La_9Sr_{0.9}Eu_{0.1}Si_6N_{1.77}O_{23.85}$ was acquired in the *Laboratoire Leon Brillouin* (LLB), on the 3T2 high resolution diffractometer. This two-axis diffractometer was used with a thermal neutron source (room temperature). Incident wavelength was 1.225 Å, with step size of 0.05°.

X-ray diffraction does not allow distinguishing between nitrogen and oxygen because of the small differences in scattering lengths. However neutron diffraction provides enough

contrast between both elements (b_O= 5.803 fm, b_N= 9.36 fm [19]), and is the most relevant technique to investigate the distribution of anions in oxynitrides.

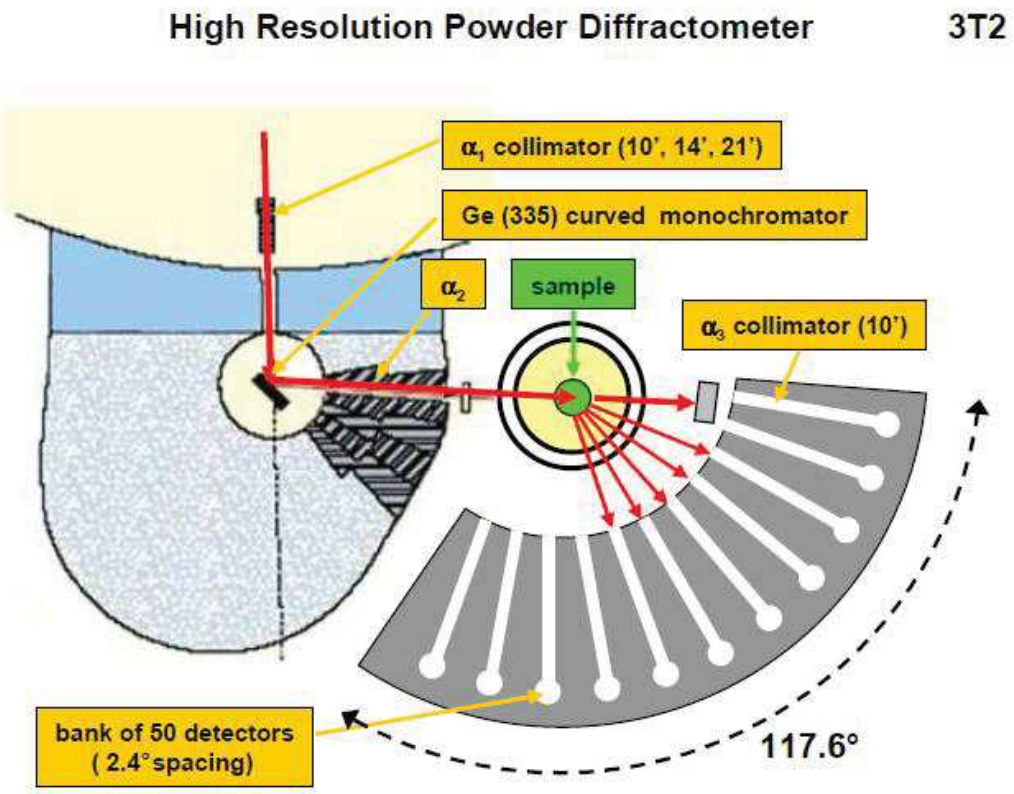

Figure II-17. Scheme of the 3T2 high-resolution diffractometer (LLB)

A Rietveld refinement of neutron powder diffraction pattern for the compound with formula $La_9Sr_{0.9}Eu_{0.1}Si_6N_{1.77}O_{23.85}$ was carried out with FullProf software. An instrumental parameter file was used. The background was taken in account by considering a linear interpolation between a set of 25 points with fixed 2θ positions. Their intensities were refined at each step of the refinement. Peak shape was taken as Thompson-Cox-Hastings pseudo-Voigt * Axial divergence asymmetry (Prf=7). Kendrick *et al.* found that the space group $P6_3$ (n°173) [6] gave a better fit for $La_{9.7}Si_6O_{22.6}N_{2.7}$ than the space group $P6_3/m$ (n°176). The differentiation of the 4f sites in two 2b sites with different distances respective to nitrogen atoms was the main reason suggested for the reduction in symmetry. Furthermore, previous studies for lanthanum strontium-substituted silicate apatites reported a preferential occupation for the alkaline-earth in one of the two 2b positions resulting from 4f site splitting while changing from $P6_3/m$ to $P6_3$ [20] [21]. In this thesis we report the preliminary results found

using the space group $P6_3$. Further work will be performed in the space group $P6_3/m$ in order to compare the resulting structural models using both space groups.

First of all, we have considered an oxidic apatite, with a fixed La/Sr ratio in the 2b sites. The small amount europium was not introduced in the refinement in order to avoid an excessive number of variable parameters. Cell parameters, atomic coordinates and B isotropic were refined in this order. The occupancy of La and Sr in the two 2b positions was refined. A clear preference of strontium for one 2b site was highlighted, with the other fully occupied by lanthanum atoms. The refined La/Sr ratio was different from the nominal composition with full occupation of this 2b site by strontium, leading to a total La/Sr ratio of 8/2. We carried out in parallel Inductively Coupled Plasma Atomic Emission Spectroscopy (ICP-AES) on the oxide precursor used for the ammonolysis: $La_9Sr_{0.9}Eu_{0.1}Si_6O_{26.55}$. Three measurements gave the same cationic ratio: La/Sr=9.15/0.85, which closely fits the targeted values. An explanation for the observed difference could be the formation of a small quantity of $La(OH)_3$ impurity, which has been detected in some X-ray diffraction patterns.

Anionic occupancies were then refined. Full occupancies resulted for O(1) and O(2) sites whereas for O(4) and O(5) occupancies of 0.89 and 0.92 were found respectively, and O(3) showed an occupancy of 1.19. As the neutron scattering length of nitrogen is significantly larger than that of oxygen, this could be explained by the presence of some nitrogen in O(3) position. We then introduced one nitrogen atom in this crystallographic site and refined the occupancies of O(3) and N(3) and the total occupancy of the site was fixed to one. On the other hand, considering that we did not found any evidence of the existence of $[Si_2NO_6]^{7-}$ units in Raman spectroscopy (section II.2.6.1.), we fixed the occupancy of O(4) to one. The refined occupancy for N(3) gave a total nitrogen content of 0.79, which was below the nitrogen content found from TGA analysis. Introducing N(5) in channel sites led finally to a total nitrogen content close to the value found by TGA. (1.82 with Rietveld Refinement, compared to 1.77 by TGA)

As previously observed by *Kendrick et al.*[6], in contrast with previous studies of oxidic apatites by neutron diffraction, the channel position O(5)/N(5) does not show a large temperature factor (the highest value is always found along the direction [001]). For instance, values as large as $100xU_{33}=0.22$ $Å^2$ [22] have been found for apatites of formula $La_{9.52}Si_6O_{26.28}$. The small temperature factors found in our samples are consistent with the presence of vacancies in the channel sites. Introduction of nitrogen in channels leads

automatically to vacancies because of the charge neutrality. The presence of nitrogen, oxygen and vacancies on a same position cannot be reasonably refined with neutron diffraction studies carried out on powders. The approximation of introducing only N(5) atoms and no O(5), can thus be justified.

Table II-10 shows the different interatomic distances in the refined structural model. Comparing the interatomic distances for the two cationic positions (1) and (2) lead to interesting conclusions. The only anionic position of the silicon tetrahedra where nitrogen atoms replace oxygen atoms is also the one with larger bond distance to Sr(1) position (Wickoff symbol 4f, A^I in the description of Chapter I). On the other hand, La(2) forms shorter bonds with O(4) atoms. 4f sites can be described as [6+3] coordination sites because 3 distances are clearly longer than the others: the longer distances correspond to La(2)-O(4) and Sr(1)-O(3)/N(3). The observed interatomic distances involve a change of coordination for 4f sites depending on whether they contain strontium or lanthanum cations. The average bond distance La(3)-O(3)/N(3) is shorter than La(3)-O(4). These structural features are important to understand the luminescence properties shown in Chapter III.

Table II-8. Refinement parameters for $La_9Sr_{0.9}Eu_{0.1}Si_6N_{1.77}O_{23.85}$.

Compound	**$La_9Sr_{0.9}Eu_{0.1}Si_6N_{1.77}O_{23.85}$**
a=b (Å)	9.7033(1)
c (Å)	7.2399(2)
Space Group	$P6_3$
λ (Å)	1.22515
Reliability Factors:	
χ^2	0.669
$R_p/R_{wp}/R_{exp}$	16.6/15.3/18.70
Reflection number	594
Number of refined parameter	56

Table II-9. Final refined structural parameters for $La_9Sr_{0.9}Eu_{0.1}Si_6N_{1.77}O_{23.85.}$ Corresponding composition is $La_8Sr_2Si_6N_{1.82}O_{23.34}$

Atom	Site	x	y	z	U_{iso} x 100	Occupancy
La(1)/Sr(1)	2b	0.33333	0.66670	0.01123	0.8(5)	0/1
La(2)/Sr(1)	2b	0.66670	0.33333	0.013(2)	1.1(5)	1/0
La(3)	6c	0.2312(6)	-0.0130(7)	0.261(4)	0.71(9)	1
Si	6c	0.4024(11)	0.3721(10)	0.262(6)	0.7(2)	1
O(1)	6c	0.3213(7)	0.4849(8)	0.264(5)	0.8(2)	1
O(2)	6c	0.5945(8)	0.4701(8)	0.269(5)	0.8(2)	1
O(3)/N(3)	6c	0.3303(12)	0.2489(15)	0.435(4)	1.1(2)	0.89(6)/0.11(6)
O(4)	6c	0.3579(14)	0.2593(16)	0.074(4)	1.0(2)	1
N(5)	2a	0	0	0.245(4)	0.4(4)	0.58(2)

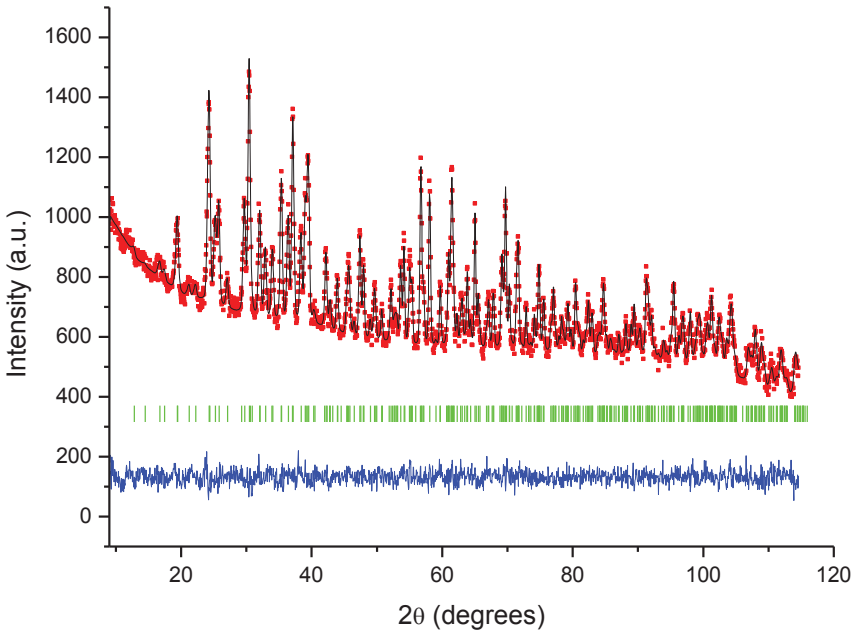

Figure II-18. Observed (Red), calculated (Black) and difference (Blue) neutron diffraction profile for $La_9Sr_{0.9}Eu_{0.1}Si_6N_{1.77}O_{23.85.}$

Table II-10. Selected interatomic distances (Å) for $La_9Sr_{0.9}Eu_{0.1}Si_6N_{1.77}O_{23.85}$

Bond	**Bond distance (Å)**
La(1)/Sr(1)-O(1) x3	2.51(4)
La(1)/Sr(1)-O(2) x3	2.50(3)
La(1)/Sr(1)-O(3)/N(3) x3	2.996(13)
La(2)-O(1) x3	2.48(4)
La(2)-O(2) x3	2.58(3)
La(2)-O(4) x3	2.742(15)
La(3)-O(1)	2.732(10)
La(3)-O(2)	2.515(9)
La(3)-O(3)/N(3)	2.55(3)
La(3)-O(3)/N(3)	2.48(5)
La(3)-O(4)	2.66(3)
La(3)-O(4)	2.47(5)
La(3)-N(5)	2.306(7)
Si-O(1)	1.637(15)
Si-O(2)	1.615(11)
Si-O(3)/N(3)	1.61(5)
Si-O(4)	1.68(5)

II.2.5. Study of the homogeneity of nitrogen composition by Auger spectroscopy and electron microprobe analysis

Two kinds of nitrogen distributions were considered: between grains and inside grains. As the nitriding method involves a solid-gas reaction, the surface of the oxide precursor is a relevant factor affecting the completeness of the ammonolysis and the homogeneity of the sample. Ideally, a layer of oxide precursor powder as thin as possible should be disposed in the crucible to ensure complete and homogeneous reaction of all grains. In practice, crucible surface is limited, and temperature homogeneity cannot be conserved all over the tube in the furnace. In order to produce large samples, layers of several millimetres

were used and the nitrogen content might vary from the top to the surface. In this thesis the distribution of nitrogen in the samples has been investigated by Auger electron spectroscopy and electron microprobe analysis.

II.2.5.1. Auger electron spectroscopy

Auger electron spectroscopy is a technique for surface analysis using the mechanism of Auger electron generation: an incident beam of particles (electrons, X-rays or ions) eject an electron linked to the atom and a vacancy in the atomic orbitals is created. Then, a less strongly bonded electron of the outer layers goes deeper to fill the vacancy. The spontaneously emitted energy is then transferred to a third electron, called Auger electron, which will leave its initial atom with a characteristic kinetic energy. The auger effect is thus a non radiative effect. It competes with the emission of X photon, when the energy of the first two steps is not transferred to the Auger electron.

An electron beam of some kiloelectronvolt (5 to 25 keV) is finely focused on the sample, which in this case is a polycrystalline powder spread on carbon tape. As the materials investigated in this work are insulators, a 2.5 nm layer of gold atoms was deposited on the sample to allow a better evacuation of charges. The etching was carried out on a scanned surface of 1 mm² in order to obtain a flat surface. A spectrum of electron energy was obtained with each peak corresponding to a transition for one element, and the evolution of their intensities have been followed. A MICROLAB VG 310-F from CECAMA (ICMCB) has been used.

The electron source was focused on one grain and measurements intersected by etching with argon (Ar^+) gun were carried out. Thus, it was possible to study the concentration of each element as a function of depth.

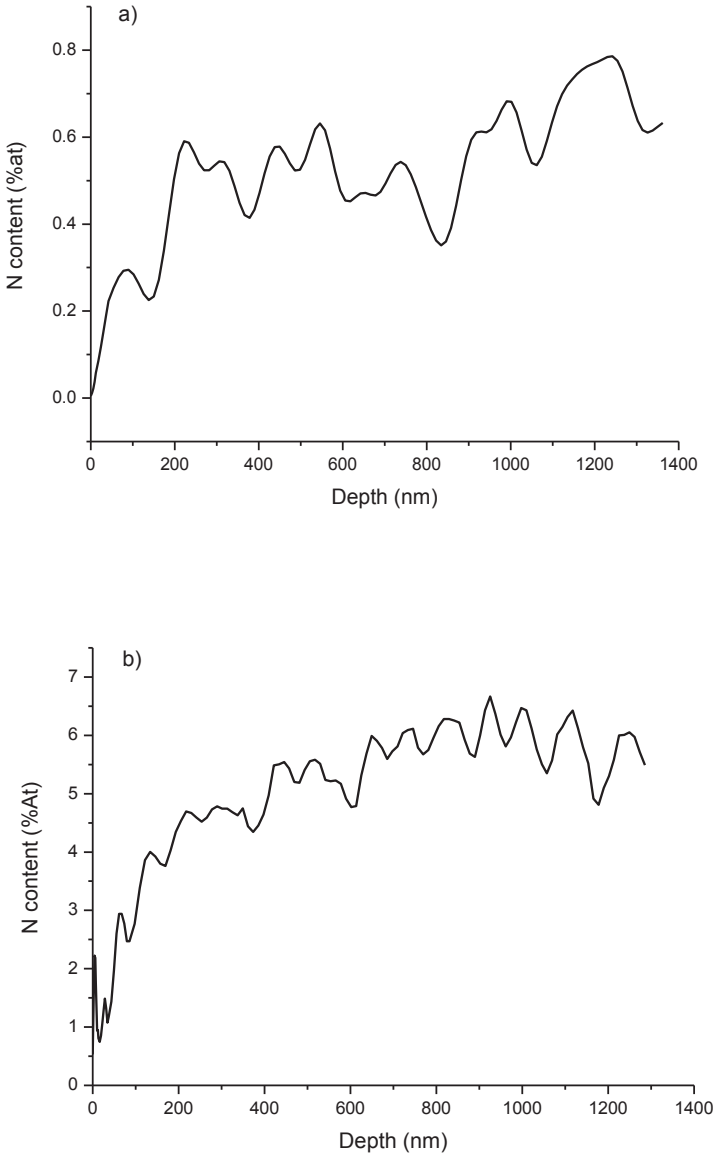

Figure II- 19. Auger electron spectroscopy for two samples: a) $La_{8.9}Ce_{0.1}SrSi_6N_{0.37}O_{25.95}$ and b) $La_{9.23}Ce_{0.1}Si_6N_{2.85}O_{21.72}$.

For several samples, we observed a quick increase in nitrogen content in the first 200 nm, followed by a slower increase in the next 400 nm until stabilization. Final values are close to nitrogen contents found by TGA. Indeed, $La_{8.9}Ce_{0.1}SrSi_6N_{0.37}O_{25.95}$ corresponding atomic percent of nitrogen is 0.87%, close to the stabilized content obtained by Auger electron spectroscopy which is c.a. 0.75%. $La_{9.23}Ce_{0.1}Si_6N_{2.85}O_{21.72}$ corresponding atomic percent of nitrogen is 7.14% and the stabilized content is c.a. 6.5%.

For the first 100 nm all element's content increase very quickly with depth except for oxygen which decreases. We believe that this behavior is a consequence of adsorbed CO_2 at the surface of the sample. Traces of carbon atoms in surface have also been found by XPS. Some grains without nitrogen were found.

II.2.5.2. Electron microprobe analysis

Electron microprobe is a non destructive elemental analysis method where the sample interacts with an electron beam and the emitted X-rays spectrum is analyzed. The electron beam irradiates a small surface of the order of some microns square. During the irradiation, a core electron is ejected. A valence electron then transfers to fill the electronic hole generated giving rise to the emission of a photon X. The photons emitted are characteristics of an element. The spectrum obtained is thus characteristic of the different elements constituting the material. The apparatus which has been used is a CAMECA SX 100 from CeCaMa (ICMCB).

The sample $La_{8.9}Ce_{0.1}SrSi_6N_{1.06}O_{24.91}$ has been studied. The powder was dispersed in an epoxy resin, which was subsequently heated overnight and solidified by polymerization. The solid resin containing the powder was then finely polished after several steps until a surface with cut particles was obtained. It was then possible to measure nitrogen and other elements concentration over the cross section of a particle. In the same way as in Auger spectroscopy, the samples were metalized with gold to reduce electron charging. We have considered different points forming lines through the particle. Figure II-20 shows the results obtained. The atomic percentage of each element has been studied except for cerium which was not detected because of its too low concentration in the sample. Nitrogen atomic % fluctuates between c.a. 2.4 and 3.6 atomic %, but the trend seems to be stable around 3%, corresponding to a nitrogen content of 1.27 per mole of formula. Other elements have their atomic % stabilizing around values that correspond to the nominal compositions: 2.3%, 14%, 21% and 62.3% for Sr, Si, La and O respectively.

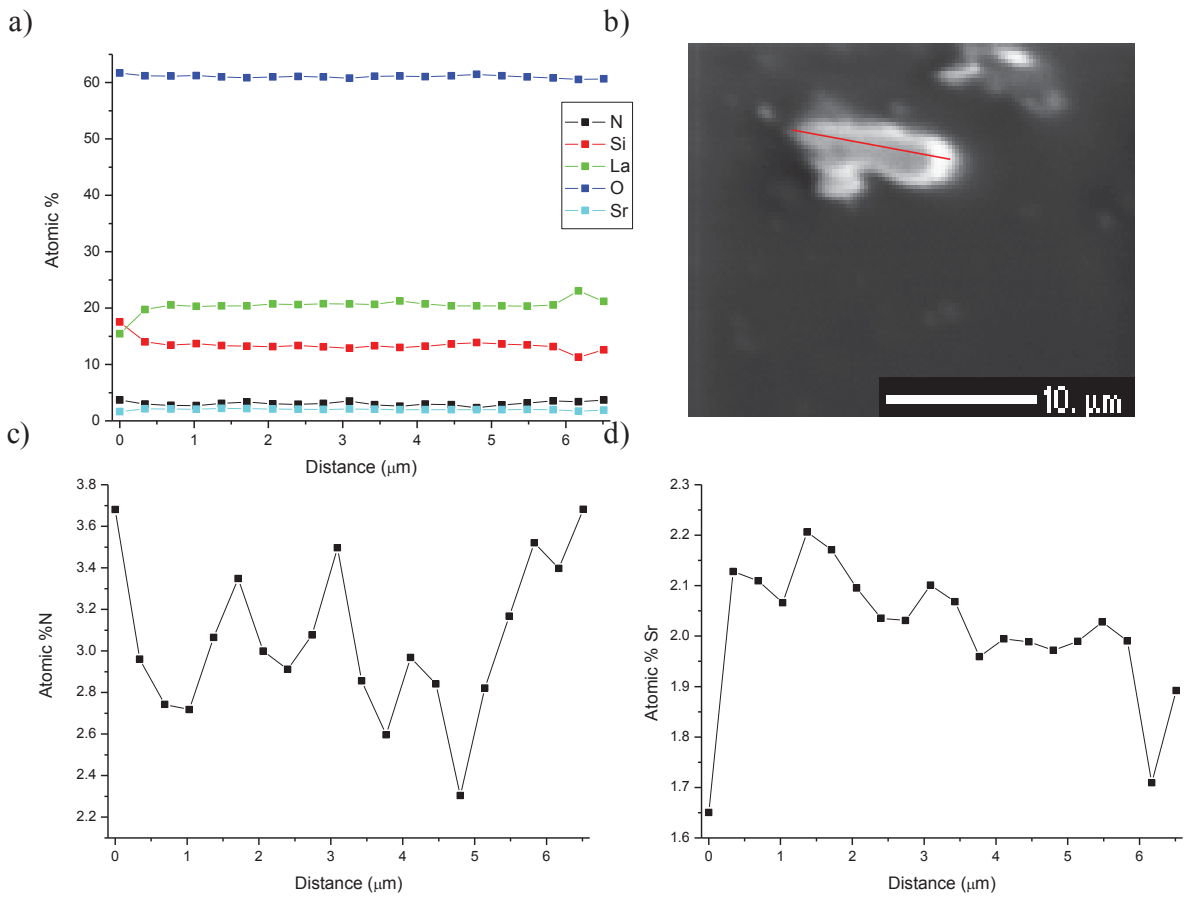

Figure II-20. Evolution of atomic % within the particle. a) All elements b) SEM picture of the particle with the chosen line in red c) Focus on N distribution d) Focus on Sr distribution.

II.2.6. Local structure studies by vibrational spectroscopy

The vibrational modes of molecules in a given compound can be studied by Infrared (IR) and Raman spectroscopy. In the samples investigated in this work we have studied the influence of nitrogen introduction on the vibrational spectra.

II.2.6.1. Raman spectroscopy

II.2.6.1.1. Apparatus and working principle

The Raman Effect was discovered in 1928 by Sir C. V. Raman and K. S. Krishnan. Raman scattering occurs during the interaction between a monochromatic and coherent light source with matter. While the main part of the incident beam is scattered elastically by the sample (Rayleigh scattering), a small quantity of photons excites molecules' vibrational modes within the matter.

Two processes of scattering occur with Raman Effect (Figure II-15). The first is characterized by a scattering from a lower energy vibrational level to a higher energy level (Stokes Effect), whereas the other one correspond to the scattering from a vibrational level of higher energy to a vibrational level of lower energy (Anti-Stokes effect). As a result of electron population distribution over the different vibrational energy levels in the excited state, the lowest energy level is more filled, and Stokes Raman scattering signal is more intense. Its study is thus generally preferred to the Anti-Stokes Raman scattering signal. Rayleigh scattering and has a considerably higher probability of occurring than Raman because the most probable event is the energy transfer to molecules in the ground state and reemission by the return of these molecules to the ground state. Fluorescence phenomena give also generally much more intense signal than Raman, and must be avoided in the window of studied wavelengths.

Raman signal will not vary qualitatively while changing the wavelength of the exciting source, but the intensity will vary as $1/\lambda^4$. Two laser sources were available: 532 nm and 785 nm. Because 532 nm is too close to some of the fluorescence excitation bands in our compounds we chose the 785 nm. Raman spectroscopy measurements were carried out in the *Institut des Sciences Moléculaires* (ISM- Université Bordeaux I) in collaboration with Dr. M. Dussauze.

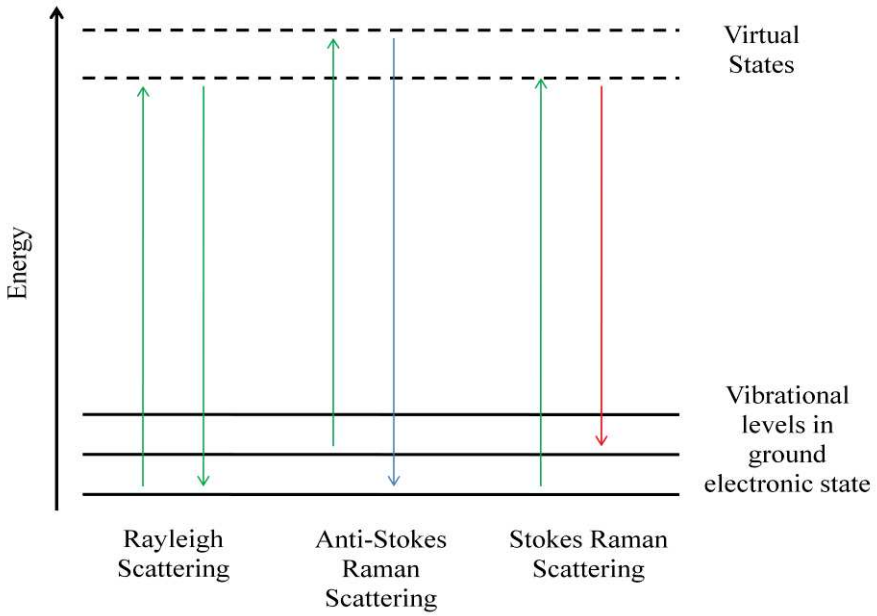

Figure II-21. Comparison between Raman scattering (Stokes and Anti-Stokes) and Rayleigh scattering

II.2.6.1.2. Experimental results

By carrying out Raman measurements on silicate samples we obtained typically the spectra shown in Figure II-22. The spectra are similar to previously reported for silico-apatites [22] [23] [24] [25]. According to these studies, the spectrum can be divided in two parts: peaks below 350 cm^{-1} correspond to the internal modes of the network, as well as vibration between rare-earth/alkaline-earth and their neighbouring anions. At higher frequency, the peaks can be assigned to the internal mode of SiO_4 units in the apatite structure. Because SiO_4 tetrahedra are relatively isolated, these peaks are very close to the spectra observed for free SiO_4 groups. These molecules show the punctual group Td with four possible vibrational modes: symmetric stretching, asymmetric stretching, symmetric bending and asymmetric bending. In our case, these modes can be respectively assigned to peaks around 854 cm^{-1}, 921 cm^{-1}, 388 cm^{-1} and 522-565 cm^{-1}.

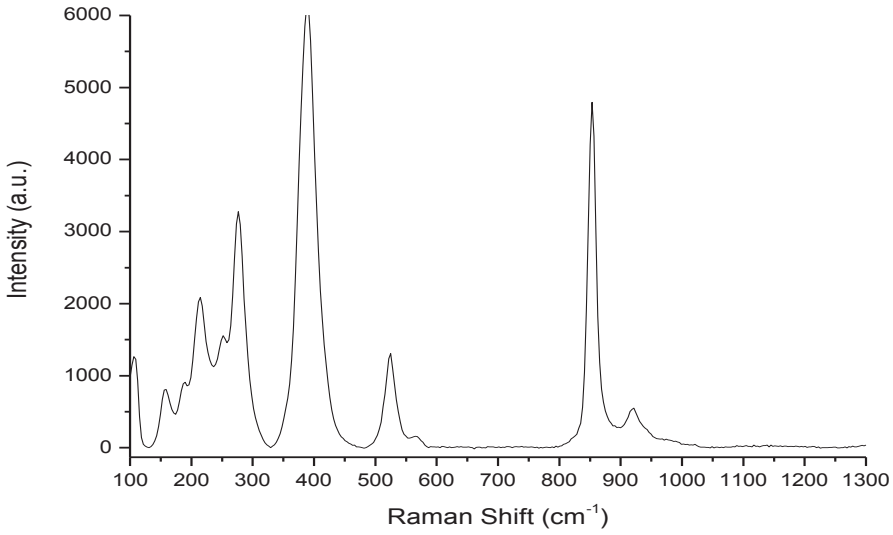

Figure II-22. Raman spectrum for $La_{8.9}Ce_{0.1}SrSi_6N_{0.37}O_{25.95}$.

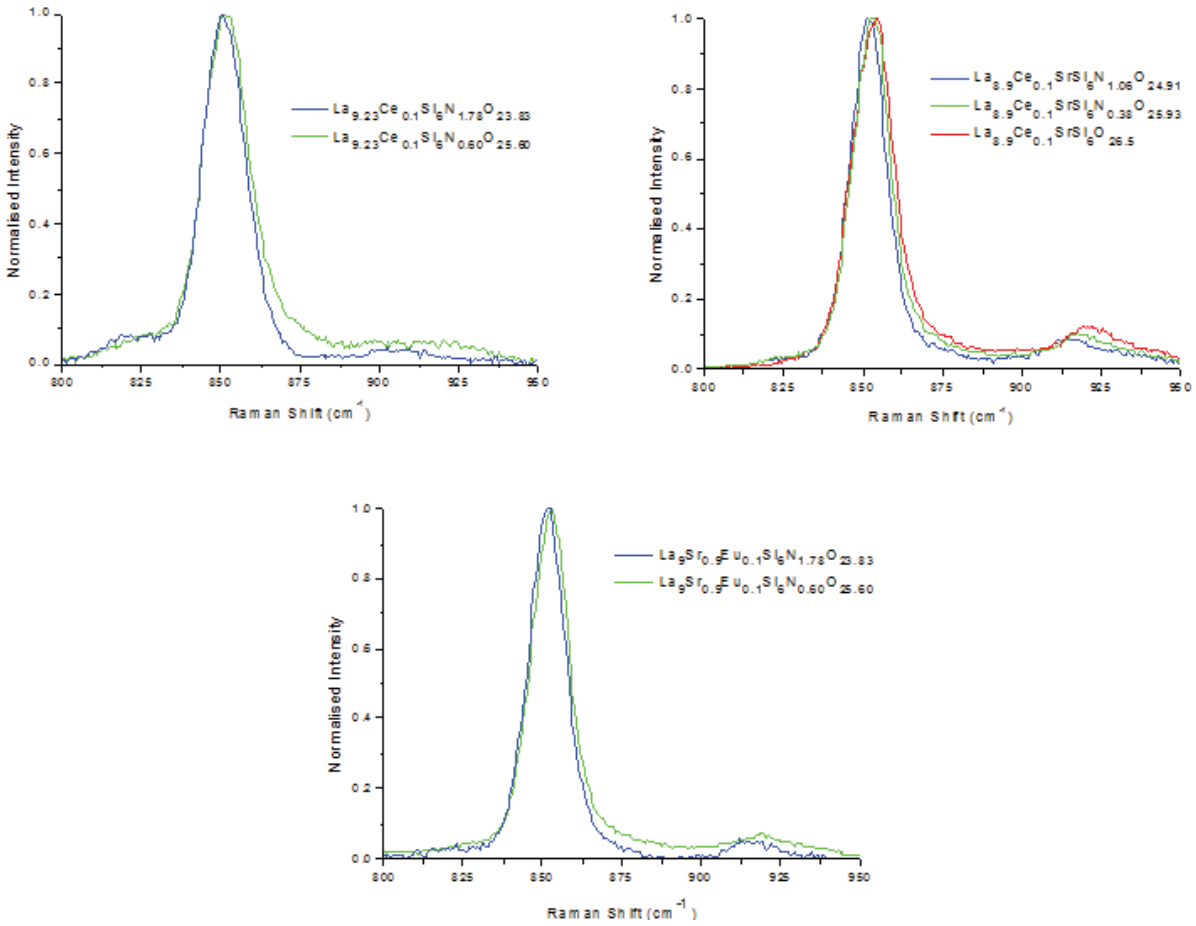

Figure II-23. Raman spectra for oxynitridoapatite compounds with different nitrogen content. Focus on SiO_4 symmetric and asymmetric stretching.

We observed that nitrogen introduction sensibly modifies the silicon tetrahedra environment. The peaks at higher energy, which are weakly coupled with the other modes in the structure, corresponding to symmetric and asymmetric stretching were slightly shifted to lower energy with increasing nitrogen content (Figure II-23).

II.2.6.2. Infrared spectroscopy

Infrared spectroscopy measurements were carried out in a spectrometer NEXUS 670 (Thermo Optek). Measurements have been carried out directly on the powder samples by attenuated total reflectance. We obtained typically the spectra shown in Figure II-24. We chose to focus on the area 600 cm^{-1}-1200 cm^{-1} where the most intense absorption bands were localized. For silico-apatite samples, nitrogen incorporation was concomitant with the presence of new peaks at lower energy, and a general higher complexity of the signal (Figure II-19).

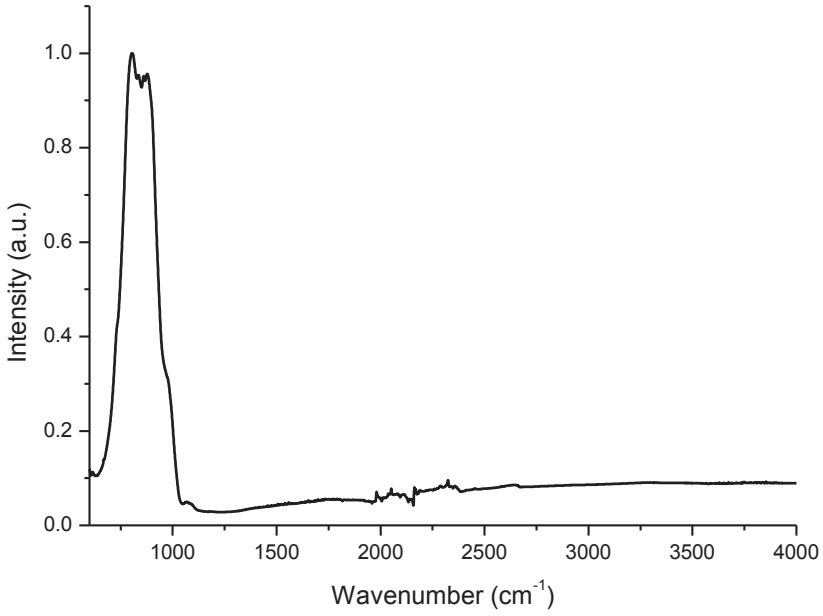

Figure II-24. IR spectrum for $La_{9.23}Ce_{0.1}Si_6N_{1.42}O_{23.87}$.

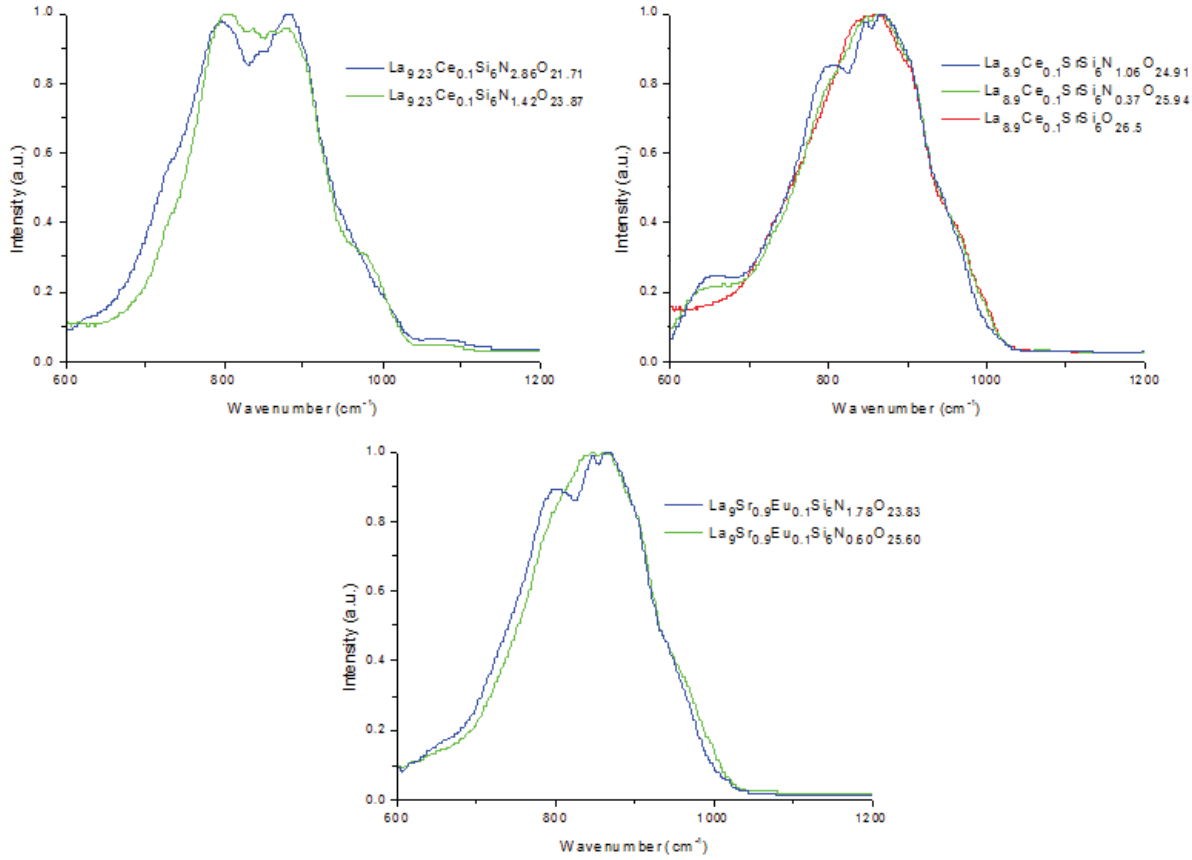

Figure II-25. Infrared spectroscopy carried out on silico-apatite samples.

II.2.6.3. DFT calculations of infrared and Raman spectra

In parallel with these measurements, *ab initio* calculations were carried out following the principles of density functional theory in collaboration with Dr. D. Cavagnat from the ISM, simulations were made with the software GAUSSIAN 0.9 with a hybrid functional density B3PW91 in the base of Pople 6-31G. Two simple molecules were considered in a vacuum environment: SiO_4H_4 and SiO_3NH_5. Hydrogen atoms were necessary for charge compensation. Theoretical Raman and Infrared spectra are shown in Figure II-26 and II-27. The use of such a simple model can be justified by the fact that silicon tetrahedra in the apatite structure are relatively isolated. Moreover, we have chosen to focus on the highest energy frequency peaks in the case of the Raman spectra (which would correspond to peaks at 854 cm^{-1} and 921 cm^{-1} in the experimental spectra) because they correspond to the vibrational modes which present less coupling with the other vibrational modes of the molecule.

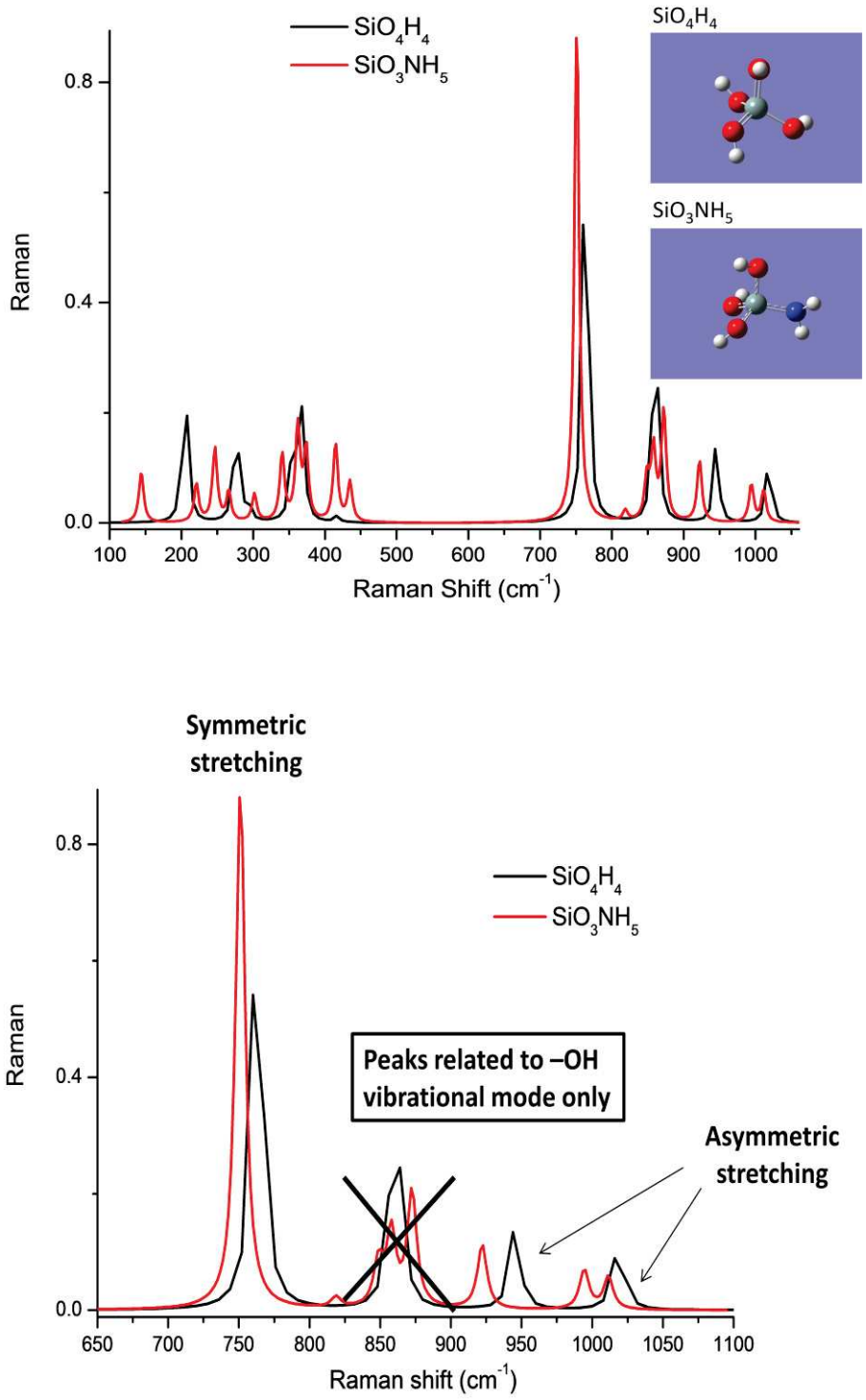

Figure II-26. Theoretical Raman spectra for SiO_4H_4 and SiO_3NH_5 by *ab initio* calculations. a) Entire spectrum. b) Focus on the area 650-1100 cm^{-1}.

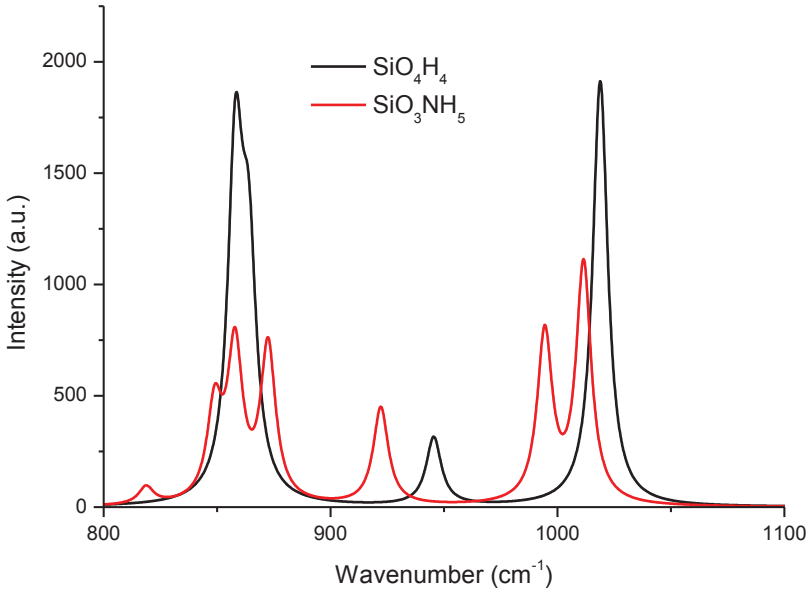

Figure II-27. Theoretical IR spectra for SiO_4H_4 and SiO_3NH_5 by calculation *ab initio*.

In the case of the simulated Raman spectra, a clear shift to the lower frequencies is visible, as well as an increase in number of peaks (Figure II-26). In the case of the simulated infrared spectra, an increase of the number of peaks can be observed, with a general shift to lower energies (Figure II-27).

Comparisons between experimental and simulated spectra have to be taken carefully. The simplicity of the model used for simulation, as well as the weakness of the variations observed in experimental spectra prevent from drawing strong conclusions. Nevertheless, the similarities between the experimentally observed and calculated variations indicate that the environment of silicon tetrahedra is sensibly modified by nitrogen introduction in the structure. These measurements suggest the presence of nitrogen in the silicon tetrahedra of the oxynitridosilicate apatites, which is coherent with the results found by neutron diffraction.

II.2.7. Local structure studies by ^{29}Si NMR

Many comparative ^{29}Si NMR studies have been carried out on silicon apatites. The main goal is to correlate isotropic chemical shifts with variations of the structural environment of the silicon. Sansom et al [26] have carried out a systematic study on eleven different lanthanum silicon oxide apatite compounds, investigating the effect of oxygen excess, alkaline-earth substitution and cationic vacancies on the ^{29}Si NMR spectra. Fully

stoechiometric samples with no oxygen exhibited a single ^{29}Si NMR peak at chemical shift ≈ -77.8 ppm. Compounds with oxygen excess showed a supplementary peak at chemical shift ≈ -80.5 ppm. Orera et al. [23] correlated the increase of this second ^{29}Si NMR peak intensity with an increase of interstitial oxide ion content as well as with an increase in conductivity by considering lanthanum silicon apatites with various alkaline-earth contents.

Silicon coordinated mostly to nitrogen tends to resonate at higher frequency than silicon coordinated mostly to oxygen. Harris et al [27] observed no differences between ^{29}Si NMR spectra of $La_{9.33}Si_6O_{26}$ and $La_5Si_3O_{12}N$. Recently, Orera et al. [5] have observed a significant reduction of the peak at chemical shift ≈-80.5 ppm after ammonolysis of $La_9SrSi_6O_{26.5}$, correlated with a loss of interstitial oxide anions by introduction of nitrogen atoms. An additional peak at lower chemical shift (≈ -73.5 ppm) was also observed, consistent with the presence of a small amount of $[SiO_3N_5]^{5-}$. We have carried out our own measurements on two selected samples: $La_{8.9}Ce_{0.1}SrSi_6O_{26.5}$ and $La_{8.9}Ce_{0.1}SrSi_6N_{1.06}O_{24.91}$.

Solid state ^{29}Si (natural abundance) NMR spectra have been acquired on a Bruker Advance 500 spectrometer operating at 99.3 MHz with a 2.5 mm (magic spinning angle) Bruker MAS probe. Direct-polarisation experiments with a 1.4 microsecond 90° pulse and recycle delays of 120s were used with sample spin-rates of 30 kHz. (Accumulation of 1400 scans)

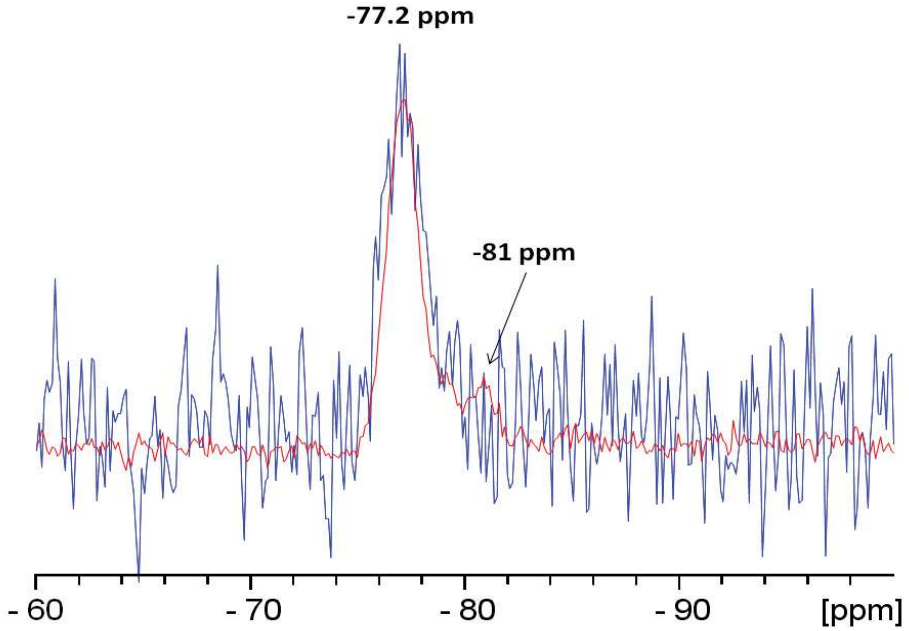

Figure II- 28. ^{29}Si NMR spectra for $La_{8.9}Ce_{0.1}SrSi_6O_{26.5}$ (Red) and $La_{8.9}Ce_{0.1}SrSi_6N_{1.06}O_{24.91}$ (Blue).

Figure II-28 shows the ^{29}Si NMR spectra of $La_{8.9}Ce_{0.1}SrSi_6O_{26.5}$ and $La_{8.9}Ce_{0.1}SrSi_6N_{1.06}O_{24.91.}$ The latter gave a substantially lower signal than the former, which account for the low signal/noise ratio obtained. In accordance with the literature, the second peak at chemical shift ≈ -81 ppm disappeared after ammonolysis, which confirms a loss of interstitial oxygen by nitriding. A third peak at lower chemical shift was hardly detectable.

II.3. Conclusion

In this study, we have been able to prepare oxynitride phosphors with apatite structure at relatively low temperature by ammonolysis of oxide precursors. The different samples have been characterized by X-ray diffraction. Nitrogen contents were determined by TGA and combustion analysis. For a given duration, increasing the flow rate and temperature of ammonolysis increased the nitrogen uptake. A general correlation between the quantity of interstitial oxygen in the precursor and nitrogen content after ammonolysis has been highlighted. Nitrogen concentration has been found homogeneous inside the particles by Auger spectroscopy and electron microprobe analysis.

Two crystallographic sites are available for nitrogen in the apatite crystal structure: silicon tetrahedra and channel sites. The distribution of nitrogen atoms in the anion sites of the crystal structure has been investigated. Vibrational spectroscopy measurements compared with DFT calculations suggest that nitrogen introduction would modify the silicon tetrahedra environment. ^{29}Si NMR study has confirmed a loss of interstitial oxygen after nitrogen introduction. The study of $La_9Sr_{0.9}Eu_{0.1}Si_6N_{1.77}O_{23.85}$ by neutron diffraction led to the conclusion that nitrogen occupies both the tetrahedra and the channel sites

References for Chapter II:

[1] Fuertes, A. *Journal of Materials Chemistry* **22**, 3293–3299 (2012).

[2] Clarke, S. J., Guinot, B. P., Michie, C. W., Calmont, M. J. C., and Rosseinsky, M. J. *Chemistry of Materials* **14**(1), 288–294 (2002).

[3] Yang, M., Oro-Solé, J., Fuertes, A., and Attfield, J. P. *Chemistry of Materials* **22**(14), 4132–4134 (2010).

[4] Jorge, A. B., Oro-Sole, J., Bea, A. M., Mufti, N., Palstra, T. T. M., Rodgers, J. A., Attfield, J. P., and Fuertes, A. *Journal of the American Chemical Society* **130**(38), 12572–12573 (2008).

[5] Orera, A., Headspith, D., Apperley, D., Francesconi, M., and Slater, P. *Journal of Solid State Chemistry* **182**(12), 3294 – 3298 (2009).

[6] Kendrick, E., Headspith, D., Orera, A., Apperley, D. C., Smith, R. I., Francesconi, M. G., and Slater, P. R. *Journal of Materials Chemistry* **19**, 749–754 (2009).

[7] Celerier, S. *Synthèse par voie sol-gel, mise en forme et caractérisation de nouveaux matériaux d'électrolyte et d'anode pour piles à combustible SOFC: Oxyapatite à charpente silicatée et Ni/Oxyapatite*. PhD thesis, Université Toulouse III - Paul Sabatier, (September 22nd 2005).

[8] Dierre, B., Xie, R.-J., Hirosaki, N., and Sekiguchi, T. *Journal of Materials Research* **22**(7), 1933–1941 (2007).

[9] Celerier, S., Laberty, C., Ansart, F., Lenormand, P., and Stevens, P. *Ceramics International* **32**(3), 271 – 276 (2006).

[10] Panchmatia, P. M., Orera, A., Kendrick, E., Hanna, J. V., Smith, M. E., Slater, P. R., and Islam, M. S. *Journal of Materials Chemistry* **20**, 2766–2772 (2010).

[11] Orera, A. and Slater, P. *Solid State Ionics* **181**(3-4), 110 – 114 (2010).

[12] Pauling, L. *Journal of the American Chemical Society* **51**, 1010–1026 (1929).

[13] Gaudé, J., L'haridon, P., Hamon, C., Marchand, R., and Laurent, Y. *Bulletin de la Société Française de Minéralogie et de Cristallographie* **98**, 214–217 (1975).

[14] Guyader, J., Grekov, F. F., Marchand, R., and Lang, J. *Revue de Chimie Minérale* **15**, 431–438 (1978).

[15] Rodriguez-Carvajal, J. *"FULLPROF: A Program for Rietveld Refinement and Pattern Matching Analysis"*. Abstracts of the Satellite Meeting on Powder Diffraction of the XV Congress of the IUCr, Toulouse, France, (1990).

[16] Shannon, R. D. *Acta Crystallographica Section A* **32**, 751–767 (1976).

[17] Jorge, A. B., Fraxedas, J., Cantarero, A., Williams, A. J., Rodgers, J., Attfield, J. P., and Fuertes, A. *Chemistry of Materials* **20**(5), 1682–1684 (2008).

[18] Masubuchi, Y., Higuchi, M., Takeda, T., and Kikkawa, S. *Solid State Ionics* **177**, 263–268 (2006).

[19] Sears, V. F. *Neutron News* **3**(3), 26–37 (1992).

[20] Sansom, J. E. H., Richings, D., and Slater, P. R. *Solid State Ionics* **139**, 205–210 (2001).

[21] Lambert, S., Vincent, A., Bruneton, E., Beaudet-Savignat, S., Guillet, F., Minot, B., and Bouree, F. *Journal of Solid State Chemistry* **179**, 2602–2608 (2006).

[22] Guillot, S. *Etude des paramètres principaux gouvernant les propriétés de conduction dans les apatites, électrolytes pour piles SOFC*. PhD thesis, Université de Lille, (September 29th 2009).

[23] Orera, A., Kendrick, E., Apperley, D. C., Orera, V. M., and Slater, P. R. *Dalton Transactions* , 5296–5301 (2008).

[24] Rodriguez-Reyna, E., Fuentes, A., Maczka, M., Hanuza, J., Boulahya, K., and Amador, U. *Journal of Solid State Chemistry* **179**(2), 522 – 531 (2006).

[25] Lucazeau, G., Sergent, N., Pagnier, T., Shaula, A., Kharton, V., and Marques, F. M. B. *Journal of Raman Spectroscopy* **38**(1), 21–33 (2007).

[26] Sansom, J. E. H., Tolchard, J. R., Islam, M. S., Apperley, D., and Slater, P. R. *Journal of Materials Chemistry* **16**, 1410–1413 (2006).

[27] Harris, R. K., Leach, M. J., and Thompson, D. P. *Chemistry of Materials* **1**(3), 336–338 (1989).

Chapter III:

Study of the luminescence properties

Chapter III: Study of the luminescence properties

III.1. Introduction

III.1.1. Concepts and definitions

III.1.1.1. Luminescent materials

Luminescent materials, also called phosphors, are solids which have the ability to emit light after absorption of energy. This initial excitation can take several different forms: electromagnetic radiation (Photoluminescence), beam of energetic electrons (Cathodoluminescence), electric voltage (Electroluminescence), mechanical energy (Triboluminescence), X-rays (X-ray luminescence), or chemical reaction (Chemiluminescence) for instance.

A phosphor can be schematically described by introducing two entities: the host lattice and the luminescent center. The host lattice is the crystalline matrix containing the luminescent center, usually a specific element in very low concentration substituting for other atoms in the material. It is called the doping agent. An example is Y_2O_3: Eu^{3+}, widely used as a red emitter in lighting industry, where Y_2O_3 is the host lattice, and Eu^{3+} ions are the luminescent center.

The host lattice characteristics will influence the center to modify the luminescence properties of the phosphor. The scientists are thus looking for crystal structures that, in combination with the appropriate optical center, can give the desired optical features. A good knowledge of the mechanisms governing the luminescence properties of the optical center is necessary for designing new phosphors with high efficiency and suitable for commercial use.

III.1.1.2. Mechanisms of luminescence

Luminescence phenomenon takes place in several steps. First, the energy of excitation is absorbed. This absorption can actually either correspond to the transition of an electron from the valence band to the conduction band of the host lattice (Absorption over the band gap), or to the transfer of a charge from a ligand to the optical center (Charge-transfer absorption), or also to the promotion of an electron of the activator from a certain energy level to an other, within its orbitals. The absorbed energy may finally transfer to the activator, which goes from a ground state, to an excited state. During the return to the fundamental state,

energy can be released in a radiative way, which is responsible for the observed luminescence properties.

The overall phenomenon of absorption-emission by an activator is often described by a configurational coordinate diagram (Figure III-1): it represents the potential energy curves of the different energy levels of a luminescent center as a function of a configurational coordinate. If one considers that the central ion is immobile while the ligands around it are moving in phase, the configurational coordinate can be written as R, which varies proportionally to the metal-ligand distance. The resulting curve has a parabolic shape, because in the approximation of a harmonic vibrational motion, the problem is equivalent to a harmonic oscillator: $E = \frac{1}{2}k\,(R - Ro)^2$, Ro being the position of lowest energy, *i.e.* the equilibrium position. Quantum mechanics indicates that the system can take only discrete values in the potential curve, corresponding to some frequencies of the oscillator: $E_V = \left(V + \frac{1}{2}\right)\hbar\omega$ with V=0, 1, 2… and ω is the frequency of the oscillator. This frequency can change between the ground and the excited state. The force constant k of the parabolas changes in consequence.

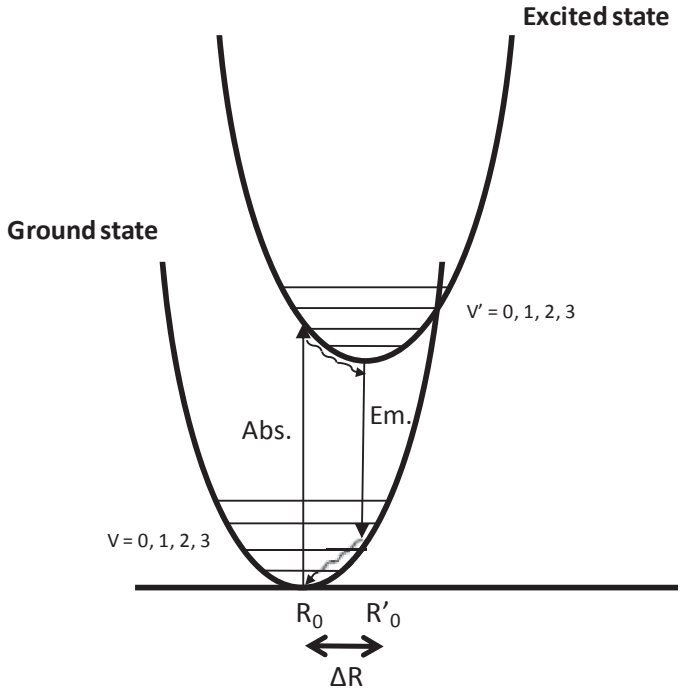

Figure III-1. Configurational coordinate diagram illustrating the absorption-relaxation-emission cycle.

In the beginning, the luminescent center is in the ground state. By absorbing energy, it raises to a higher energy level, thus being in an excited state, which have its own potential curve. This excited state does not generally correspond to the ground vibrational state of the excited state. After a non radiative deexcitation through the different vibrational levels of the excited state, the luminescent center can relax to the ground state either directly by vibrational deexcitation, or by emitting a photon. This is a key-step when one does consider synthesizing an efficient phosphor. Indeed, the production of good luminescent materials requires keeping the ratio radiative deexcitation/vibrational deexcitation as high as possible in order to obtain the highest efficiencies.

This representation brings to light several important parameters which have to be looked at when one is considering the luminescent properties of a phosphor:

-The Franck-Condon offset, which is the difference between the equilibrium positions of the fundamental state (R_0) and the excited state (R). In Figure III-1, it is noted as ΔR. Schematically, it is the difference of gravity center position between ground and excited state. If ΔR is large, the absorption band will be automatically large because absorption will take place from the lowest vibrational state of the ground state to a large amount of different vibrational states of the excited state with nearly equal probabilities. If $\Delta R=0$, for instance in the case of intra-configurational transitions, both parabolas are superimposed. Moreover, if the force constant of both parabolas is the same, it ensues that the exact same energy is necessary for each transition from the ground state to the excited state and in this case absorption and emission spectra are composed of lines (FWHM~1-3 nm).

-The Huang-Rhys coupling constant, also noted S, is representative of the strength of the electron-lattice coupling. Depending on its value, the luminescent center can be considered as in a weak, intermediate, or strong coupling regime. If the two parabolas have the same force constant k, $S\hbar\omega$ is the quantity of energy lost during the relaxation step in each parabola. It is a multiple of the energy difference between two vibrational levels. The higher the constant S, the stronger the coupling between the electrons of the luminescent specie and the lattice.

-The Stokes shift, which is the energy difference between the excitation and the emission. It provides direct information about the actual shift between excitation and emission band in the luminescence spectra. The higher the crystal-field, the higher the Stokes shift value. In the simple case where both parabolas have the same force constant, the Stokes shift is equal to $2S\hbar\omega$. A currently widely spread design for white LEDs is constituted by the combination of

an InGaN blue diode with one or several down converters (phosphors). In order to obtain a warm white light, phosphors with high Stokes shift are required: an excitation in the blue for an emission in the orange with a wide spectral distribution would be ideal for instance.

It is important to understand that those parameters cannot actually be considered separately. They are playing all together a part in the actual luminescent features of an activator in a host lattice and also are correlated. For instance, when ΔR is large, the Stokes shift is automatically larger, and S is proportional to $(\Delta R)^2$.

III.1.1.3. Selection rules for optical transition

Radiative transitions are governed by some rules which are called selection rules. These rules are determined by the wave function of the different energy levels and the nature of the operator governing the transition between these levels. They express the conditions for the highest and lowest probabilities of radiative transition in a compound. The purpose of this introduction is not to be exhaustive about these rules, neither to explain precisely how they are obtained. It will just remind two of them, which are easy to use and important:

-First, the parity selection rule forbids electronic transitions between levels with the same parity in the case of a dipolar electric operator. This rule is also called Laporte's rule.

-Electronic transitions between levels with different spin state are forbidden. This rule is known as spin selection rule.

These rules are not absolute, and the transitions that are actually "forbidden" can occur. But, they will occur with a very low rate compared to transitions "allowed" by these rules. Furthermore, in some cases, these rules can be bypassed if the wave functions of the system are mixed with another of different parity.

III.1.1.4. Nonradiative return to the ground state

After absorption and relaxation, the nonradiative return to the ground state always competes with the radiative one. Actually, dissipation of energy via the vibrational modes of the crystal lattice is in general much more probable than via photon emission. The rate for nonradiative desexcitation is indeed much higher than for radiative desexcitation (a very fast emission has a rate of 10^8 s^{-1} whereas the vibrational state is about 10^{13} s^{-1}).

Several mechanisms have been described to explain radiativeless return to the ground state. A first interpretation involves the existence of a crossing point between the two parabolas of the excited state and ground state (see Figure III-2.a)). In the excited state, thermal agitation can promote the electron from a vibrational state to a higher energy vibrational state close to this crossing point. The system can then transfer to a vibrational state of the ground state and finally relax from there. The rate of this type of nonradiative transition was described by Mott's activation energy formula which takes the form of a classical Arrhenius law[1]:

$$N = A_M \, e^{(-\frac{E_X}{kT})}$$

Where A_M is a rate constant of the order $10^{13}s^{-1}$ and E_x the energy difference between the lowest energy level of the excited state and the crossover. The higher the temperature, the more likely this non radiative process. As a consequence, this mechanism is usually called thermal quenching. In general, white LEDs work at temperatures around 80°C - 90°C, so phosphors have to be designed in order to not be affected significantly by thermal quenching at these temperatures. When the crossing point is localized close to the base of the excited state potential curve, "configurational quenching" may exist. In this case luminescence is not possible. A very high ΔR will favor the luminescence quenching.

A second description involves only the energy levels of the parabolas. If the difference of energy between the minimum of both parabolas is equal to or less than 4-5 times the vibrational frequency of the surroundings, the energy absorbed can directly excite a few high-energy vibrations dispersing the energy in the crystal lattice. This loss of energy by phonon emission to the host lattice vibrational mode is called multiphonon emission, and its rate has been described by Kiel's formula [2]:

$$N = A_K \varepsilon^p (1 + \frac{1}{e^{\left(\frac{\hbar\omega_0}{kT}\right)} - 1})^p$$

Where $\hbar\omega_0$ is the lattice-phonon energy, p the number of phonons necessary to bridge the band gap, A_k a rate constant and ε is a small coupling constant. Finally, Struck and Fonger [3] have proposed a unified model for temperature depending mechanisms allowing a nonradiative return to the ground state from the excited state which comprises the above two descriptions. It introduces a third interpretation by tunneling when the lowest vibrational level

of the excited state is nearly resonant with a high vibrational level of the ground state. (Figure III-2.b))

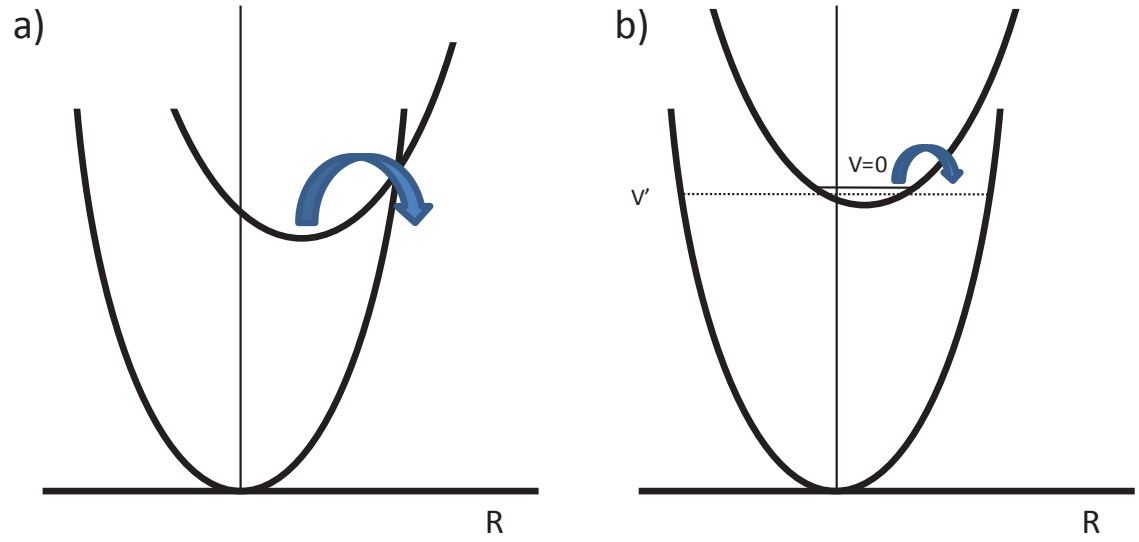

Figure III-2. Different descriptions for nonradiative return to the ground state. a) Thermal quenching with crossover. b) Tunneling between vibrational levels of the excited and ground state.

Nonradiative return to the ground state can also happen via mechanisms involving directly the host lattice's characteristics. If the excited state level is too close, or even in the conduction band of the host matrix, the phenomenon of photoionization can take place. With a sufficient thermal agitation, an electron in the excited state can be transferred into the conduction band, stay trapped, and come back to the ground state via radiativeless electron-hole recombination. Typical examples are La_2O_3: Ce^{3+}, Y_2O_3: Ce^{3+}, La_2O_2S: Ce^{3+}. Host lattices band gaps are too small, or rare-earth energy levels are located at high energy in the conduction band and photoionization takes place. [4] [5]

III.1.1.5. Rare-earth as doping elements for phosphors

Many types of ions can be used as luminescent centers: alkali halides, transition metal ions (Mn^{2+}, Cr^{3+})... One class of elements has proven to provide efficient emitting centers in many host lattices: rare-earth ions. Rare-earth elements correspond to the 15 elements of the lanthanide line plus scandium and yttrium. Lanthanides constitute a class of chemical elements characterized by the filling of the 4f shell. As this shell is inner, and shielded by $5s^2$ and $5p^6$ orbitals, the different lanthanides show close chemical properties. For instance, many

of them form cations in the trivalent state and are very electropositive. This homogeneity in chemical properties is remarkable. On the contrary, they show differences in physical properties, notably regarding the luminescence. Some of them show line emission as Eu^{3+}, Er^{3+}, Tb^{3+} and Pr^{3+} whereas others present band emission like for instance Ce^{3+}, Eu^{2+} and Sm^{2+}. In order to explain the differences of emission broadness between these cations, we will take the example of Eu^{2+} and Eu^{3+}.

Eu^{3+} shows the electron configuration [Xe] $4f^6$ $6s^0$. Transitions can occur only within the 4f shell. Because of the high oxidation state of the cation the electrons of the 4f shell are strongly bound to the nucleus and transitions to the 5d shell are difficult. As 4f electrons are shielded from the crystal field, the energy of electronic levels are rather insensitive to the chemical environment. As a consequence the differences between the constant forces of the ground state and the excited state are small. ΔR is nearly equal to 0, and absorption and emission will take place as sharp lines. Furthermore, transitions nearly always occur at the same energy between different host lattices.

Eu^{2+} shows the electron configuration: [Xe] $4f^7$ $6s^0$. Because of the lower oxidation state electrons are less bound to the nucleus, and easier to transfer from the 4f shell to the 5d shell. On the other hand, the half-filled 4f layer is very stable, with all the spin aligned according to Hund's first rule. As a consequence, among all the rare-earth cations in the oxidation state +2, Eu^{2+} shows the highest energy transition from 4f to 5d orbitals [6]. The absorption energy is in the UV/Blue range, which is an adequate feature for phosphors. The transfer of electrons from the 4f inner shell to the 5d levels is allowed by the parity selection rule and the spin selection rule. As stated before, the 5d orbitals are outer and very sensitive to modifications of the environment of the cation: coordination site geometry, ligand charge, and covalence. Thus, a large crystal field splitting can decrease the lowest energy 5d levels leading to excitation and emission in the visible. $4f \rightarrow 5d$ transitions are characterized by a large ΔR, resulting from the changes in binding between the ground and the excited states. As a result, Eu^{2+} gives generally broad excitation and emission bands. This property is targeted in phosphors for white LEDs. However, in the case of a small crystal-field splitting, the lowest component of the $4f^6 5d^1$ configuration can be high in energy, so as the $^6P_{7/2}$ level of the $4f^7$ configuration would lie below it. As a consequence, a sharp line emission of Eu^{2+} can also sometimes be observed as it happens for instance in SrB_4O_7: Eu^{2+} [7].

III.1.2. Scientific approach

The apatite structure used in this work as a host lattice for phosphors shows two different cation sites. The introduction of nitrogen in the structure might generate various crystallographic environments for the activators. To allow an interpretation of the luminescence spectra we compared the optical properties of oxidic and nitride samples. Oxidic phosphors were obtained by treating in Ar/H_2 the same precursors used to obtain the nitrided phosphors by ammonolysis. The treatment in Ar/H_2 leads to reduction of the rare-earths Eu and Ce.

Some nonradiative processes are temperature depending, and less probable with decreasing temperature. Measurements at very low temperatures allow observing emissions that cannot be observed at room temperature because of thermal quenching mechanisms. As explained previously, this is particularly useful to assign the observed emission and excitation bands to the available crystallographic sites. In this work measurements under liquid helium were carried out using a specific set-up described in the Appendices of this thesis.

III.1.3. Experimental techniques

Photoluminescent properties were analyzed using a spectrofluorimeter SPEX FL212. Excitation spectra were corrected for the variation of the incident flux as well as emission spectra for the transmission of the monochromator and the response of the photomultiplier. This equipment is composed of a 450W xenon lamp, an excitation and emission double monochromator and a thermoelectricity cooled photomultiplier tube.

The SPEX FL212 was also used for recording the diffuse reflectance spectra of the luminescent samples. In this case, the emission and the excitation monochromator are set in a synchronous mode, in order to collect all the diffuse reflection of the xenon lamp without catching any fluorescence photon. Diffuse reflection spectra give the intensity of diffused light by a given sample for each wavelength received from the luminous source. In practice, measurements are carried out with a spectrofluorimeter specifically designed to adopt a configuration where both monochromators of excitation and emission are in synchronous scanning mode, so that the wavelength received by the photomultiplier (output of the emission monochromator) is the same as the one received by the sample (output of the excitation monochromator).

A black reference (B: Blacktoner), and a white reference (W: Magnesia MgO) were scanned in the same condition as the sample (S) and the diffuse reflection (D) was obtained using the following relation: D= (S-B) / (W-B). Due to the fact that MgO is not a perfect white sample (r_{MgO}=0.97, reflection at 400 nm) the corrected diffuse reflection value is r = 0.97D. Absorption can be deduced from those spectra following this equation: a = 1-r. All the diffuse reflection spectra given in this work show the evolution of D versus the wavelength.

III.1.4. Crystallographic sites for cations in the apatite structure

III.1.4.1. Introduction

A precise study of phosphor properties requires a good knowledge of the host lattice crystal structure, and more precisely, of the crystallographic sites available for substitution with doping elements. Indeed in a phosphor the luminescent properties and the crystal structure are closely related, and it is possible to identify the determining factors that account for the observed luminescence properties relative to the arrangement of the atoms in the crystal. Generally, two factors are considered: covalency and crystal-field.

The covalency of the bonds formed between the optical center and its ligands is the interpenetration of their atomic orbitals to form molecular orbitals. When the two atoms show similar electronegativities, the molecular orbitals are larger, and the repulsion between the electrons decreases. The corresponding energy levels are stabilized and present a small shift towards lower energy. This is called the nephelauxetic effect. The interelectronic repulsion plays a role in the total splitting of the different atomic levels. Indeed, each orbital will not be affected in the same way by the nephelauxetic effect: internal orbitals will see the nephelauxetic effect shielded by more external orbitals, which in turn will be much more affected. As a consequence, in a rare-earth cation as Eu^{2+} or Ce^{3+}, the energy of 5d levels will decrease more than that of 4f. For large covalency, the resulting 5d $\rightarrow$ 4f transitions will occur at lower energies.

The crystal-field, depending on the spatial arrangement of the electron cloud around the optical center, also plays a very important role in the observed luminescence properties. The interactions between the electron clouds of both optical center and ligands depend on the coordination polyhedron as well as on the nature and number of ligands. For a given optical center, the molecular orbitals energy will split depending on their interactions with the orbitals of the ligand. A high crystal-field splitting of the 5d orbitals will lower the lowest

energy 5d level and increase the total splitting between the lowest and the highest energy 5d level. Subsequently, the optical center emission will be at higher wavelength, and the excitation area (comprising several 4f→5d transitions) will be wider.

The crystal-field determines the splitting of 5d levels. A strong crystal field splitting is generally characterized by:

- Ligands with high formal charge. For instance, the crystal-field is expected to be larger for a site coordinated to nitride anions than for oxide anions.

- Different interactions between the 5d orbitals and the ligands. A larger crystal-field splitting is expected for an anisotropic coordination polyhedron.

The following section is dedicated to the study and comparison of the two cationic crystallographic sites A^I and A^{II} in an apatite structure crystallizing in the space group $P6_3/m$. The objective is to acquire some ideas of how should behave a rare-earth element with luminescent properties localized in one or the other site by considering both factors mentioned above.

III.1.4.2. Coordination polyhedra and bond length considerations

For an apatite of formula $[A^I]_4[A^{II}]_6[(TO_4)_6][X]_2$ crystallizing in the space group $P6_3/m$, two cation sites can be considered for the rare-earth or alkaline-earth metals: A^I (Wyckoff symbol 4f) and A^{II} (Wyckoff symbol 6h). A^I shows coordination number IX, with tricapped trigonal prismatic geometry, whereas A^{II} shows coordination number VII, with pentagonal bipyramidal geometry. In the space group $P6_3$ the A^I site is split into two positions with slightly different z coordinates (the mirror plane is suppressed), but these two sites show the same geometry of the coordination polyhedra as $P6_3/m$. For the same ligands the resulting crystal-field splitting is larger for 6h sites than for 4f sites (Figure III-3) with a difference of 6.45 $\Delta_O/10$ (where Δ_O is the total crystal-field splitting in an octahedral geometry).

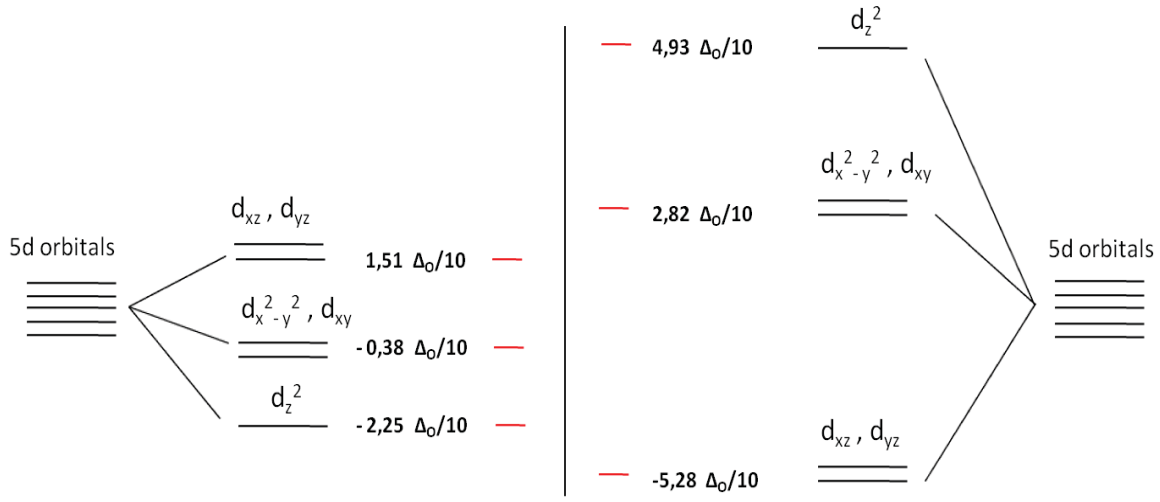

Figure III-3. Representation of the relative d-orbitals energy levels in two crystal-field symmetries: tricapped trigonal prism (left) and pentagonal bipyramid (right). (Values are taken from [8])

The 6h sites show six bonds with anions located in silicon tetrahedra and a shorter bond with the anion O(4) located in channels running along the c-axis (Table III-1 and Figure III-4). The anion O(4) is not bonded to the silicon atoms and is usually called the free anion. The larger covalency of A-O(4) bond induces a larger nephelauxetic effect for 6h sites compared to 4f sites.

As a consequence, the following hypothesis can be made: the activators Ce^{3+} or Eu^{2+} in 6h sites should emit at longer wavelengths and should show a broader excitation spectrum than if located in 4f sites. This interpretation is in agreement with previous studies on luminescent silicate apatites [26] [10] [97] [8].

Table III-1. Selected interatomic distances (Å) for the apatite of formula $La_{9.33}Si_6O_{26}$ (X-Ray powder diffraction, Rietveld refinement in space group $P6_3/m$, taken from [13]).

Bond	**Bond distance (Å)**
La(4f)-O(1) x3	2.496(4)
La(4f)-O(2) x3	2.547(4)
La(4f)-O(3) x3	2.878(4)
La(6h)-O(1)	2.744(5)
La(6h)-O(2)	2.523(4)
La(6h)-O(3) x2	2.476(2)
La(6h)-O(3) x2	2.610(3)
La(6h)-O(4)	2.271(9)
Si-O(1)	1.621(4)
Si-O(2)	1.619(6)
Si-O(3) x2	1.621(3)

III.1.4.3. Spatial distribution of the activators

The spatial distribution of the activators affects the optical properties. Indeed, if the sites are too close a lower limit for concentration quenching should be expected. In the case of the apatite structure, the tricapped trigonal prisms of 4f sites share triangular faces forming chains running along [001] with short cation-cation distances between neighbour polyhedra (around 3.59 Å). In the ab plane the minimum separation between these cations is 5.61 Å (for $La_{9.33}Si_6O_{26}$). On the other hand, the pentagonal bipyramids of 6h sites share corners. The free anions at the channels are bonded to three 6h sites whereas the anions in the silicon tetrahedra are bonded to two 6h sites. The minimum distances between 6h sites are 7.19 Å along the c-axis and 4.25 Å in the ab plane.

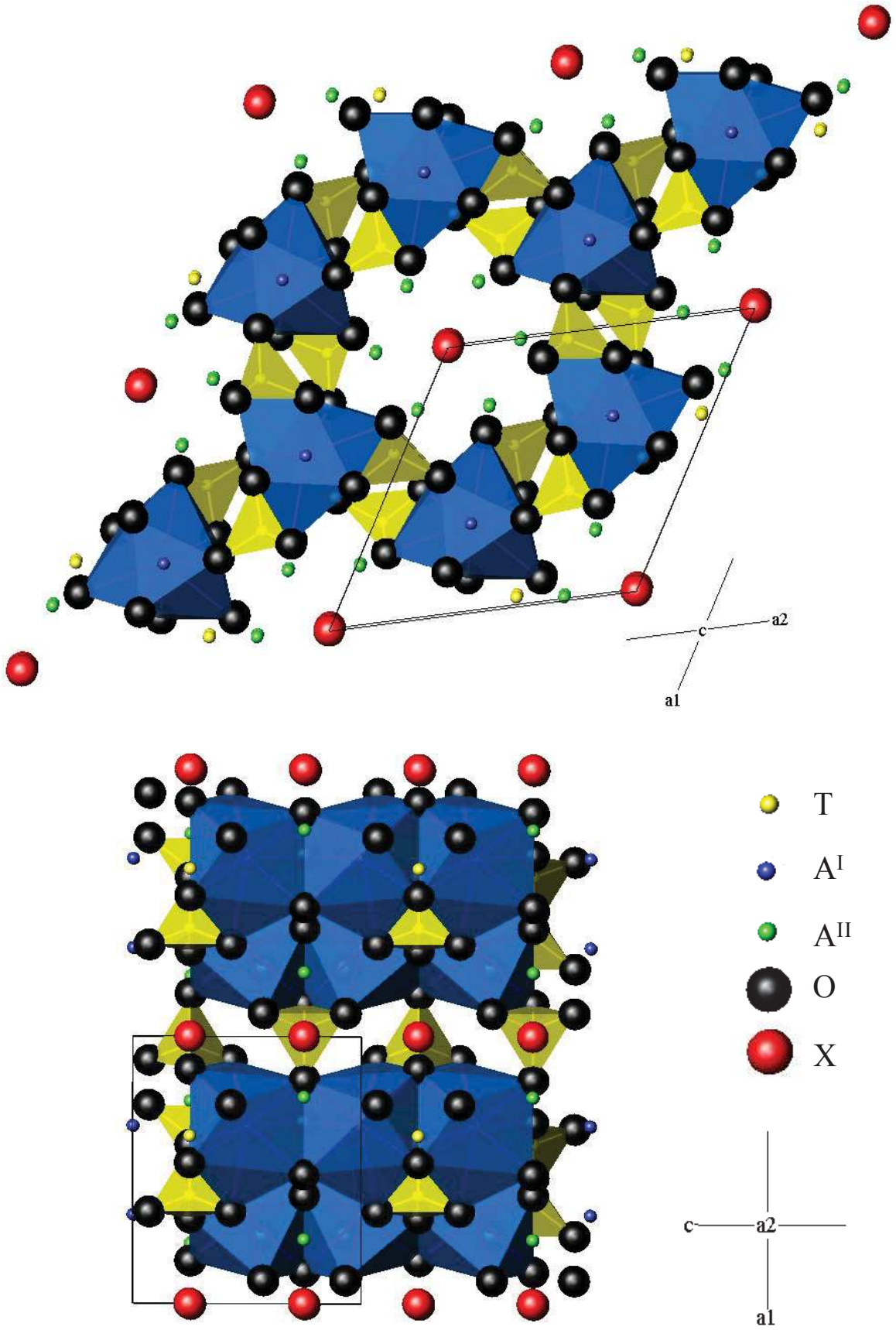

Figure III-4. The apatite structure showing the A^I coordination polyhedra depicted in blue.

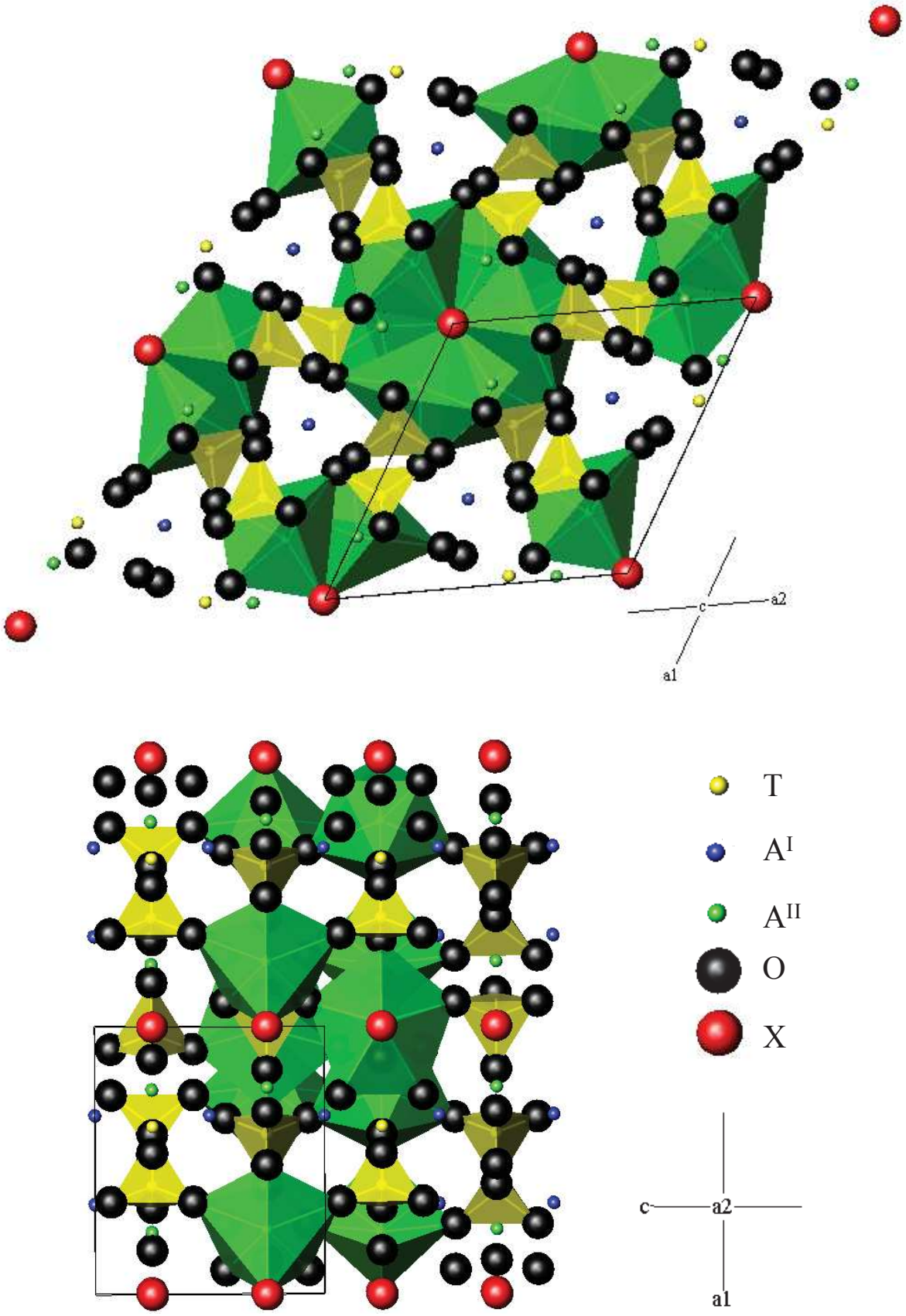

Figure III-5. The apatite structure showing the A^{II} coordination polyhedra depicted in green.

In the following section of the manuscript are described and studied the optical properties we have observed for the different materials synthesized. While considering our initial hypothesis, we have drawn relationships between the crystal structure and the optical properties by trying to attribute emission/excitation spectra to crystallographic sites, taking in account the modifications brought by nitrogen atoms.

III.2. Europium-doped compounds

III.2.1. Europium-doped oxynitridosilicates

III.2.1.1. Luminescence features at room temperature

III.2.1.1.1. $La_9Sr_{0.9}Eu_{0.1}Si_6N_{0.60}O_{25.60}$ luminescence: comparison with $La_9Sr_{0.9}Eu_{0.1}Si_6O_{26.5}$ reduced under Ar/H_2

Europium shows two oxidation states Eu^{3+} and Eu^{2+}. In the most stable oxidation state +3, europium exhibits a luminescence composed of narrow lines, consequence of electronic transitions within the non-bonding $4f^6$ shell (also called 4f-4f transitions). In the oxidation state +2, it exhibits on the contrary a band luminescence, consequence of 5d-4f transitions with a high sensitivity to external crystal field modification. Broad band excitation and emission are the targeted properties in this work, and then we aim to stabilize the divalent oxidation state.

Figure III-6 shows the excitation and emission spectra at room temperature of $La_9Sr_{0.9}Eu_{0.1}Si_6O_{26.5}$ reduced under Ar/H_2, $La_9Sr_{0.9}Eu_{0.1}Si_6N_{0.60}O_{25.60}$ and $La_9Sr_{0.9}Eu_{0.1}Si_6N_{1.77}O_{23.85}$. Both reduced oxide and ammonolyzed compounds show a broad band emission centered at 513 nm (yellow-green), which can be excited in a set of broad bands ranging from 300 nm to 475 nm. No qualitative difference in luminescence features has been observed between the oxide compound reduced under Ar/H_2 and the nitride samples. It can thus be stated that nitrogen introduction does not affect the luminescence features at room temperature of europium-doped lanthanum strontium silicoapatites.

Eu^{2+} and Sr^{2+} show similar crystallochemical features. For coordination number IX, rSr^{2+}=1.31 Å and rEu^{2+}=1.30 Å [16]. Previous structural studies by neutron diffraction of $La_{8+x}Sr_{2-x}Si_6O_{26+x/2}$ ($0 < x < 2$) suggest the location of Sr^{2+} at 4f sites [18] [21] [20]. The 4f site shows a larger coordination number than the 6h site and should be preferably occupied by

larger cations (In coordination VII, rLa^{3+}=1.10 Å and rSr^{2+}=1.21 Å [16]). Also, according to the second Pauling's rule: "*In a stable coordination structure the electric charge of each anion tends to compensate the strength of the electrostatic valence bonds reaching to it from the cations at the centers of the polyhedra of which it forms a corner*" [12]. As Sr^{2+} shows a lower formal charge than La^{3+} it occupies preferably the 4f sites with a lower bond strength than the 6h sites. Our results show that nitriding does not affect significantly the optical properties of $La_9Sr_{0.9}Eu_{0.1}Si_6O_{26.5}$ that in turn are close to those recently reported for the solid solutions Eu^{2+}: $La_{10-x}Sr_x(SiO_4)_6O_{3-x/2}$ [98]. Only one combination of emission/excitation spectra has been observed at room temperature. It is likely that Eu^{2+} substitutes Sr^{2+} at the 4f sites as expected from the similar ionic radii and coordination preferences of both cations. 4f sites are only bonded to the anions of the silicate group. The study of $La_9Sr_{0.9}Eu_{0.1}Si_6N_{1.77}O_{23.85}$ by neutron diffraction (section II.2.4.2.) suggests that nitrogen is going both in silicon tetrahedra and channel sites. As previously stated, 4f sites can be described as [6+3] coordination sites because 3 ligands are clearly at longer distances from the cation than the others. Nitrogen has been found to be located in these sites; with an even longer distance respective to 4f sites than in the oxidic apatite (see Table III-1). We suggest that this could account for the observed luminescent properties.

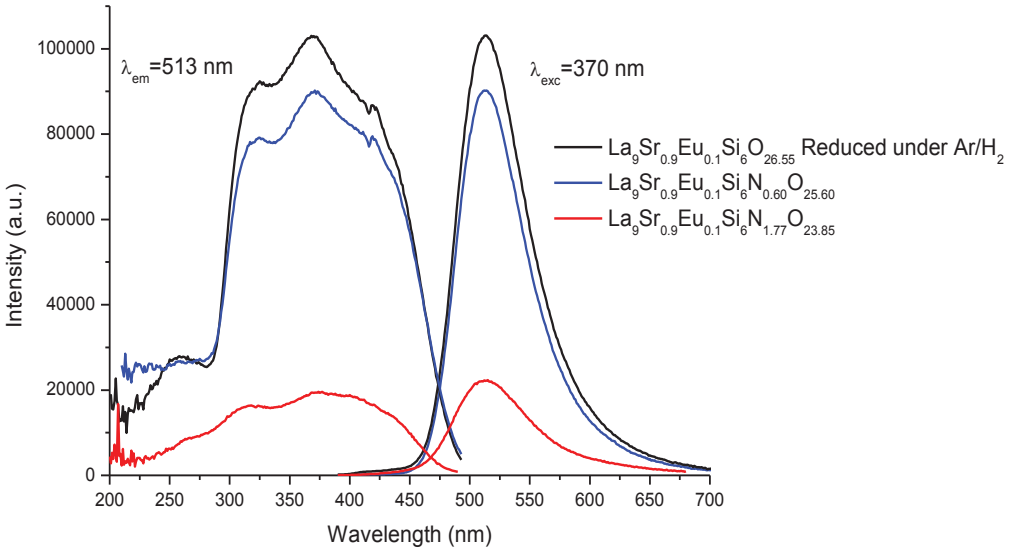

Figure III-6. Excitation and emission spectra of $La_9Sr_{0.9}Eu_{0.1}Si_6O_{26.5}$ reduced under Ar/H_2 (dark), $La_9Sr_{0.9}Eu_{0.1}Si_6N_{0.60}O_{25.60}$ (blue) and $La_9Sr_{0.9}Eu_{0.1}Si_6N_{1.77}O_{23.85}$ (Red).

Measurements at room-temperature indicate that 4f sites are not influenced by nitrogen introduction. In order to confirm this statement, and highlight some other luminescent characteristics, optical measurements have been carried out on various other compositions at low temperature and room temperature. These studies will be the subject of the rest of this Eu-doped silicates section.

III.2.1.1.2. Diffuse reflection spectra

The diffuse reflection spectrum of $La_9Sr_{0.9}Eu_{0.1}Si_6N_{0.60}O_{25.60}$ (Figure III-7) shows an absorption band matching with the excitation spectrum of Figure III-6 and ranging from 300 to 450 nm. Additional absorption bands that could be attributed to the luminescence of other sites are not observed. Considering the spectrum observed for the undoped compound $La_{9.33}Si_6O_{26}$ the absorption at shorter wavelength can be attributed to the host lattice (transfer of an electron from the valence band to the conduction band).

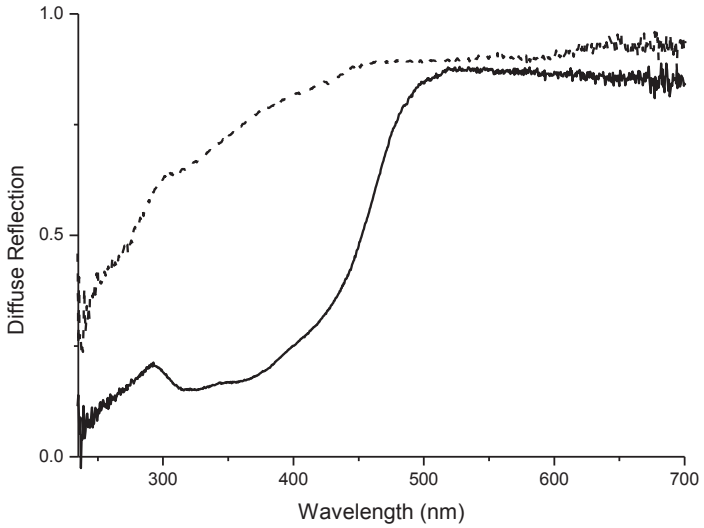

Figure III-7. Diffuse reflection spectra of undoped $La_{9.33}Si_6O_{26}$ (dashed line) and $La_9Sr_{0.9}Eu_{0.1}Si_6N_{0.60}O_{25.60}$ (solid line).

III.2.1.1.3. Influence of the alkaline earth

The variation of alkaline-earth radii (for coordination number IX, rBa^{2+}= 1.47 Å, rSr^{2+}= 1.31 Å, rCa^{2+}= 1.18 Å [16]) affect the luminescence features. A simple correlation could be done with the observed emission wavelength for isostructural compounds with different alkaline-earth metals:

Smaller alkaline-earth metal → Smaller crystallographic site → Larger crystal-field splitting → Longer emission wavelength

In some cases the crystal structure changes for the different alkaline-earth cations and the above correlation is not so straightforward. For example in Eu-doped $MSi_2O_2N_2$, (M=Ba, Sr, Ca), the three compounds show monoclinic symmetry but different space groups [20]. Not all parameters vary in the same trend going from Ba to Ca, and a trend is barely respected regarding emission maxima.

In such cases the sites for the activators may show different geometries, cation-ligand bond lengths and coordination numbers. If there is more than one site available for the activator, preferential occupation can occur according to the size of the alkaline-earth and the luminescence feature will change in consequence.

Apatites are flexible structures that can easily accommodate different cations without significant modification of the crystal structure. For instance the compounds $La_9MSi_6O_{26.5}$ with different alkaline-earth cations are isostructural [21]. In apatite phosphors, this characteristic leads to simple correlations between the luminescent properties and the ionic radius of the alkaline-earth cation. A good example is $M_5(PO_4)_3Cl$: Eu^{2+}, (M=Ba, Sr, Ca) [21], where emission maxima are at 436, 447 and 457 nm for M= Ba, Sr and Ca respectively. In some binary compounds where the alkaline-earth nature directly affects the size of the crystallographic sites in the same way, simple trends can also be found: decreasing the radius will increase the crystal-field splitting of the Eu^{2+} site, and the emission will be red-shifted. For example in: MO: Eu^{2+} (M=Sr, Ca), where in going from SrO: Eu^{2+} to CaO: Eu^{2+} the emission band shifts from 625 nm to 733 nm. [22] [23] But counter-example also exist where there is not a simple correlation, for instance in MS: Eu^{2+} (M= Sr, Ca, Mg) [24].

As reported in chapter II (section II.2.2.) both cell parameters a and c decrease with the alkaline-earth radius in nitrided $La_9M_{0.9}Eu_{0.1}Si_6O_{26.5}$ (M= Ba, Sr, Ca) with compositions

$La_9Ba_{0.9}Eu_{0.1}Si_6N_{0.59}O_{25.61}$, $La_9Sr_{0.9}Eu_{0.1}Si_6N_{0.60}O_{25.60}$ and $La_9Ca_{0.9}Eu_{0.1}Si_6N_{0.57}O_{25.64}$. As it can be seen in Figure III-8, the emission shifts when changing the alkaline-earth: emissions are centered in 510, 513 and 522 nm for M=Ba, Sr and Ca respectively. The increase in the emission wavelength is associated with a decrease in the emission intensity.

Decreasing alkaline-earth radius in $La_9M_{0.9}Eu_{0.1}Si_6O_{26.5}$ decreases 4f site size without changing the number and nature of ligands. It thus logically increases the crystal-field with a greater splitting of 5d levels and so the emission is naturally shifted at longer wavelength. In this case, in the configurational coordinate diagram, the parabola of the excited state is at lower energy, with a higher ΔR, and the crossing point between the ground state and the excited state parabolas is closer to the base of the excited state, making the thermal quenching easier. This could explain the observed decreasing intensity.

Excitation spectra are also modified by the crystal-field. The crystal-field splitting for Ca containing compounds is larger with 5d bands localized in the range 250-450 nm.

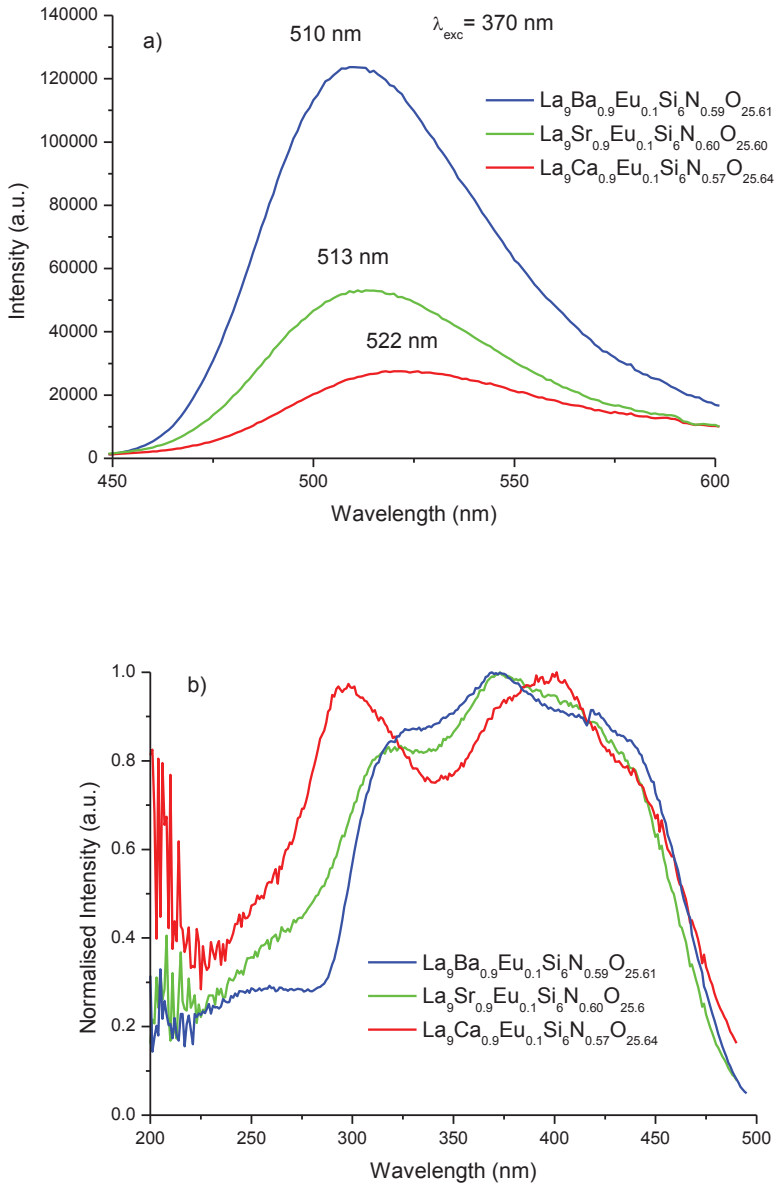

Figure III-8. a) Emission and b) excitation spectra of $La_9Ba_{0.9}Eu_{0.1}Si_6N_{0.59}O_{25.61}$ (Blue), $La_9Sr_{0.9}Eu_{0.1}Si_6N_{0.60}O_{25.60}$ (Green) and $La_9Ca_{0.9}Eu_{0.1}Si_6N_{0.57}O_{25.64}$ (Red).

III.2.1.1.4. Study of the luminescence of Eu^{3+} as trace amounts

The luminescence spectra of the sample $La_9Ca_{0.9}Eu_{0.1}Si_6N_{0.57}O_{25.64}$ showed weak narrow-line emissions that are typical of Eu^{3+}. Precise studies on these luminescence features have been carried out. Eu^{3+} luminescence is mainly composed by $4f^6 \rightarrow 4f^6$ intraconfigurational transitions. Typical energy levels diagram of Eu^{3+} cations is shown in Figure III-9. Absorption occurs between ^7F_j (j= 0, 1, 2) and ^5D_j, $^5L_6$, $^5L_7$, ^5G_j levels or by charge transfer between a ligand of the coordination site and the europium cation. After relaxation, radiative desexcitation occurs between $^5D_0$ and ^7F_j levels (j= 0, 1, 2, 3, 4, 5, 6). Eu^{3+} shows precise luminescence characteristics associated to the symmetry of the site considered, and is often used as a structural probe.

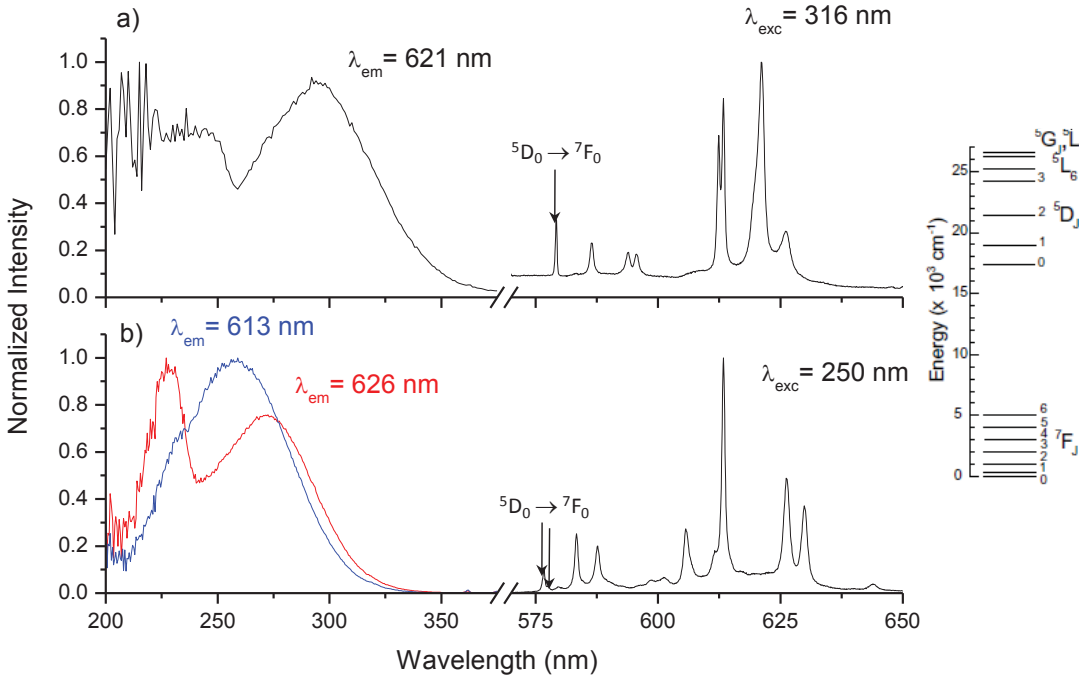

Figure III-9. Eu^{3+} ions emissions and associated charge-transfer band in $La_9Ca_{0.9}Eu_{0.1}Si_6O_{25.64}N_{0.57}$ (a), and the oxidic precursor $La_9Ca_{0.9}Eu_{0.1}Si_6O_{26.55}$ (b). Partial energy level diagram of the free Eu^{3+} ion is shown on the right.

The excited state $^5D_0$ and the ground state $^7F_0$ are singlet, so the structure of the $^5D_0 \rightarrow ^7F_0$ spectrum is composed of solely one component. For a single crystallographic environment for Eu^{3+}, there will be only one peak corresponding to the $^5D_0 \rightarrow ^7F_0$ transition. The charge transfer band (CTB) position can provide information on the ligand-Eu^{3+} bonding.

This position is influenced by the nature of the ligand: a higher electronegativity of the ligand leads to a CTB at higher energy. The ammonolysis introduces nitrogen atoms which are less electronegative than oxygen. They generally form more covalent bonding, so in oxynitride the CTB can be expected at lower energy than in oxide.

Figure III-9 shows the luminescence properties of Eu^{3+} in two compounds: $La_9Ca_{0.9}Eu_{0.1}Si_6O_{26.55}$ without reducing treatment and $La_9Ca_{0.9}Eu_{0.1}Si_6N_{0.57}O_{25.64}$. The emission spectrum of the former (Figure III-9.b)) exhibits two narrow lines assignable to two different $^5D_0 \rightarrow {}^7F_0$ transitions at 576.7 nm and 577.7 nm. It confirms that Eu^{3+} is present in both 6h and 4f crystallographic sites in the oxide apatite, as previously observed in $Ca_2La_8(SiO_4)_6O_2$ [25]. Moreover, while looking at the different excitation spectra corresponding to the different emission lines (λ_{em} = 613 nm and λ_{em} = 625 nm), two types of CTB can be found. One is composed of a single band peaking at 255 nm (Figure III-9.b) blue), while the other is composed of two bands one peaking at 225 nm and the other at 275 nm (Figure III-9.b) red). As seen previously, 6h coordination site has the particularity of being composed of six oxygen atoms linked to silicon tetrahedra and one oxygen atom considered as a "free anion" localized in channel position. As a consequence, two kinds of charge-transfer can take place for a Eu^{3+} cation in this site. Moreover, the bonding between the "free ligand" and the cation is more covalent, and thus charge transfer occurs at lower energy, and can be assigned to the part of the excitation band at longer wavelength. On the contrary, in 4f sites all oxygen atoms belong to SiO_4 tetrahedra: a more homogeneous charge transfer band is expected. In agreement with the above discussion, the charge-transfer band centered at 255 nm is assigned to trivalent europium in 4f sites whereas the modulated charge-transfer band is assigned to trivalent europium in 6h sites. Below 225 nm, a contribution coming from the host lattice is also possible.

In the ammonolyzed compound, a clearly distinct additional Eu^{3+} emission can be found (Figure III-9.a)). This time the $^5D_0 \rightarrow {}^7F_0$ wavelength area exhibits only one single peak localized at 579 nm, clearly shifted to longer wavelength compared to the oxide sample. The 4f levels, even shielded by 5d shells are still influenced in small proportion by electronic environment modifications in such a way that an increase of the crystal field and higher bond covalency (nephelauxetic effect) will actually slightly increase the emission wavelength of 4f→4f transitions. A single-site Eu^{3+} emission peculiar to the ammonolyzed compound has thus been detected. This emission spectrum has been obtained for an excitation at 316 nm, a low energy wavelength clearly shifted compared to the CTB of the oxide. It would logically

correspond to a selective excitation of a small amount of nitrided sites where the europium has not been reduced. The corresponding excitation spectrum (λ_{em}= 621 nm) present two bands, where the component at higher wavelength has been shifted to longer wavelength. This experimental observation can be understood considering the substitution after the ammonolysis of the oxygen atom in the channel sites by nitride.

III.2.1.2. Luminescence at liquid helium temperature

III.2.1.2.1. Search for other luminescence features

The main objective of the measurements at liquid helium temperature was to obtain the certainty that no other luminescence was observable in this compound. Indeed, no other luminescence feature assignable to other crystallographic site was found. Nevertheless, an important characteristic of the crystal structure has been highlighted during these measurements, which will be discussed in the following section.

III.2.1.2.2. Structural disorder

One important point which has to be taken in account is that the apatite structure is very flexible. Its structure can accommodate a large set of local modifications: vacancies, nitrogen substitution for oxygen, and anion excess in interstitial positions. Low-temperature measurements with liquid helium on two apatite compounds reduced under Ar/H_2 (Figure III-10 and Figure III-11) indicate the presence of many emission bands with the same shape (same full-width at half maximum for instance) but slightly shifted one from each other, the shift being as high as 15 nm between the two extreme peak positions. Furthermore, the corresponding excitation spectra are very similar. Two compositions were tested: $La_{8.67}\square_{0.33}Sr_{0.9}Eu_{0.1}Si_6O_{26}$ and $La_{9.9}Eu_{0.1}Si_6O_{27.}$ The latter shows high oxygen excess but full cationic occupancy, whereas the former contains cationic vacancies and no oxygen excess. In both cases we observe the same phenomena. It looks like the crystal fields are slightly different, the shape of the site being more or less distorted. This suggests the existence of different local environments for the 4f sites in the material with different emission. Regarding the optical features, the emission bands can be attributed to a “family of crystallographic sites”. This phenomenon can be compared, although in a lower proportion, to the pronounced inhomogeneous broadening occurring in glasses, where optical centers differs one from the other because of the absence of crystal periodicity.

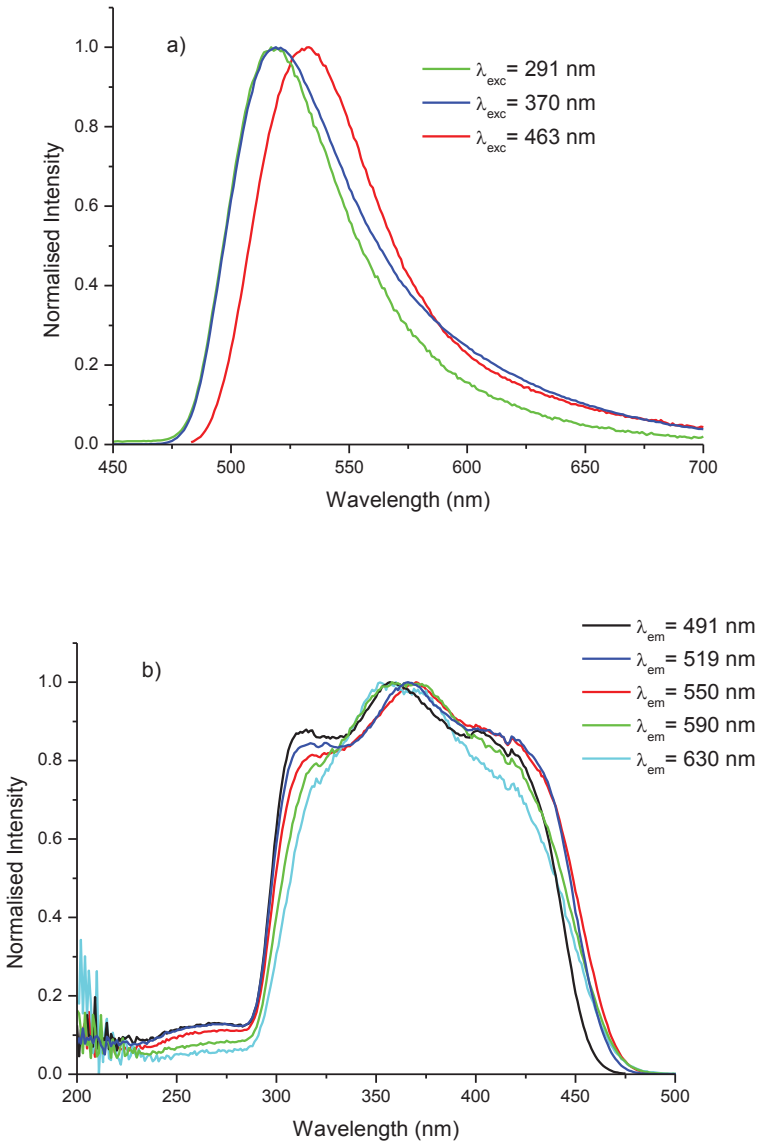

Figure III-10. Emission a) and excitation b) spectra at 4.2K of $La_{8.67}Sr_{0.9}Eu_{0.1}Si_6O_{26}$ reduced under Ar/H_2.

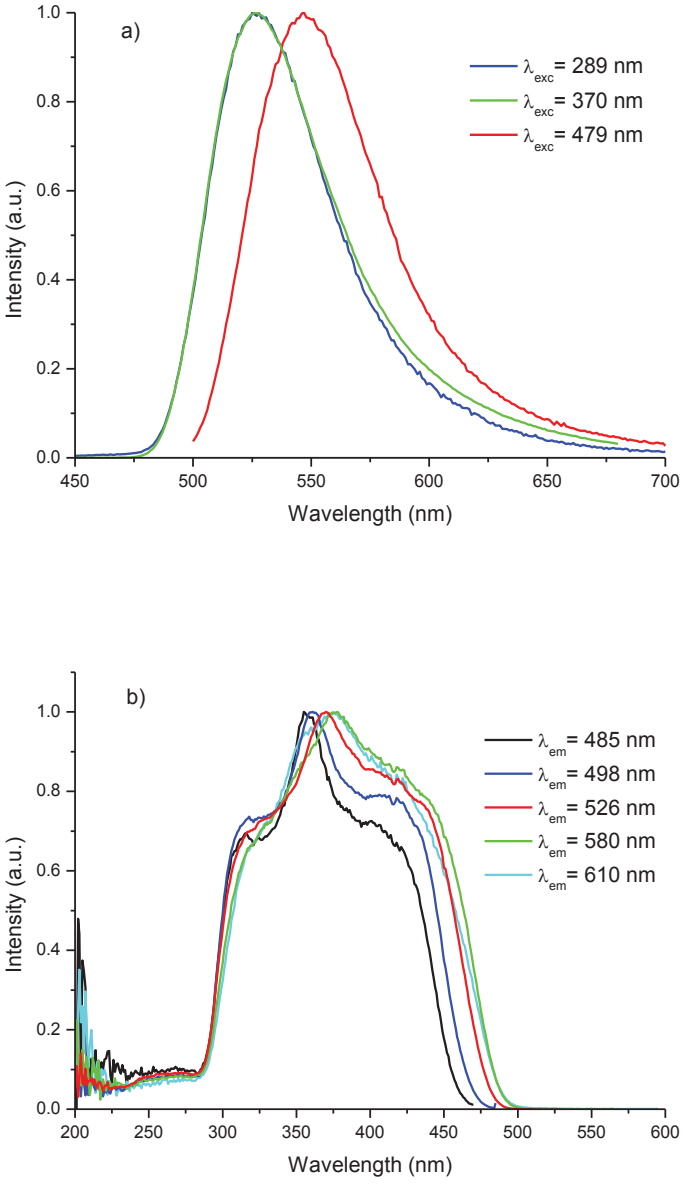

Figure III-11. Emission a) and excitation b) spectra at 4.2 K for $La_{9.9}Eu_{0.1}Si_6O_{27}$ reduced under Ar/H_2.

III.2.2. Europium-doped germanates

Germano-apatites doped with europium and ammonolyzed were also investigated. Figure III-12 shows the diffuse reflection spectra of $La_{9.5}Sr_{0.4}Eu_{0.1}Ge_6O_{26.75}$ before and after ammonolysis at 600°C. After treatment in $NH_{3(g)}$, an important absorption band ranging from 300 nm to 540 nm is observed and can be attributed to $4f^7 \rightarrow 4f^6 5d^1$ Eu^{2+} transition. For excitation in this strong absorption band, no Eu^{2+} emission is detected in the visible even for low temperature measurements that were carried out at liquid helium temperature (4.2K). The absorption band at lower wavelength is attributed to host lattice absorption.

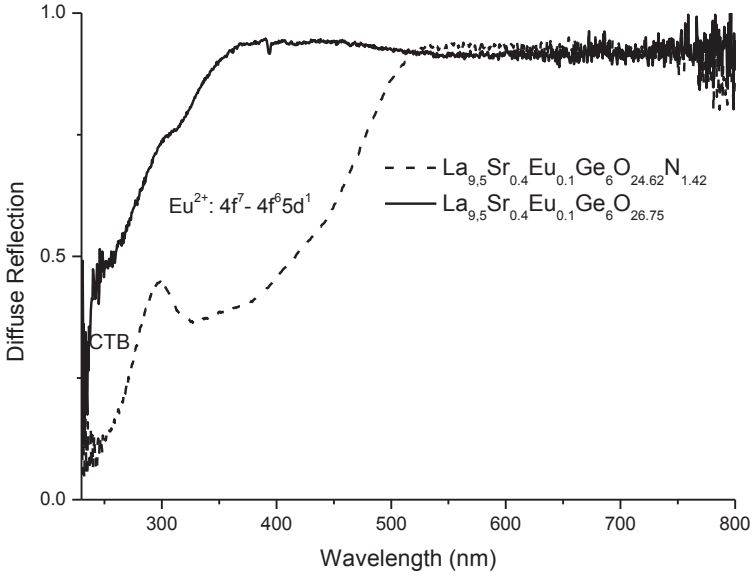

Figure III-12. Diffuse reflection spectra of $La_{9.5}Sr_{0.4}Eu_{0.1}Ge_6O_{26.75}$ (Solid Line) and $La_{9.5}Sr_{0.4}Eu_{0.1}Ge_6N_{1.42}O_{24.62}$ (Dashed Line).

Some very weak Eu^{3+} red-luminescence could be detected. Fluorescence measurements with detection of luminescence at higher wavelength were also carried out and no emission in the infrared was observed. As a consequence, it seems that europium has been reduced during the ammonolysis process, but does not present any emission, which is certainly due to a configurational quenching. In this compound the lower 5d levels may be shifted to very low energy and the absorbed excitation energy is non radiatively relaxed towards Eu^{2+} ground state through the crossing point of fundamental and excited curves of Eu^{2+} levels in the configurational diagram.

III.3. Cerium-doped compounds

Ce-doped oxynitridosilicates and germanates with apatite structure have given the most interesting properties of this study. The host lattice $La_{10}Si_6O_{24}N_2$ doped with trivalent cerium has already been investigated [8], but not the equivalent lattice with strontium substitution. Ce-doped germanate oxynitrides have also been investigated.

III.3.1. Cerium-doped oxynitridosilicates

III.3.1.1. Room temperature measurements

III.3.1.1.1. Interpretation of $La_{8.9}Ce_{0.1}SrSi_6N_{0.37}O_{25.95}$ luminescence

Cerium is the most abundant of the rare-earth elements. The most stable valence state is 4+, with electron configuration: [Xe] $4f^0$. This cation can be responsible for absorption, but it will not bring any luminescence properties to a host lattice. On the contrary Ce^{3+} shows good luminescence properties, the single electron in the 4f shell allowing 4f→5d transitions.

The $4f^1$ ground state splits into two levels, $^2F_{5/2}$ and $^2F_{7/2}$, which are separated by c.a. 2000 cm^{-1} due to spin-orbit coupling. As a consequence, radiative deexcitation from $4f^05d^1$ excited level yields two bands with the same full band width at half maximum (FWHM), and separated by 2000 cm^{-1}. Generally the band at highest energy is the most intense, but high concentration in Ce^{3+} can favor re-absorption that equilibrates both components.

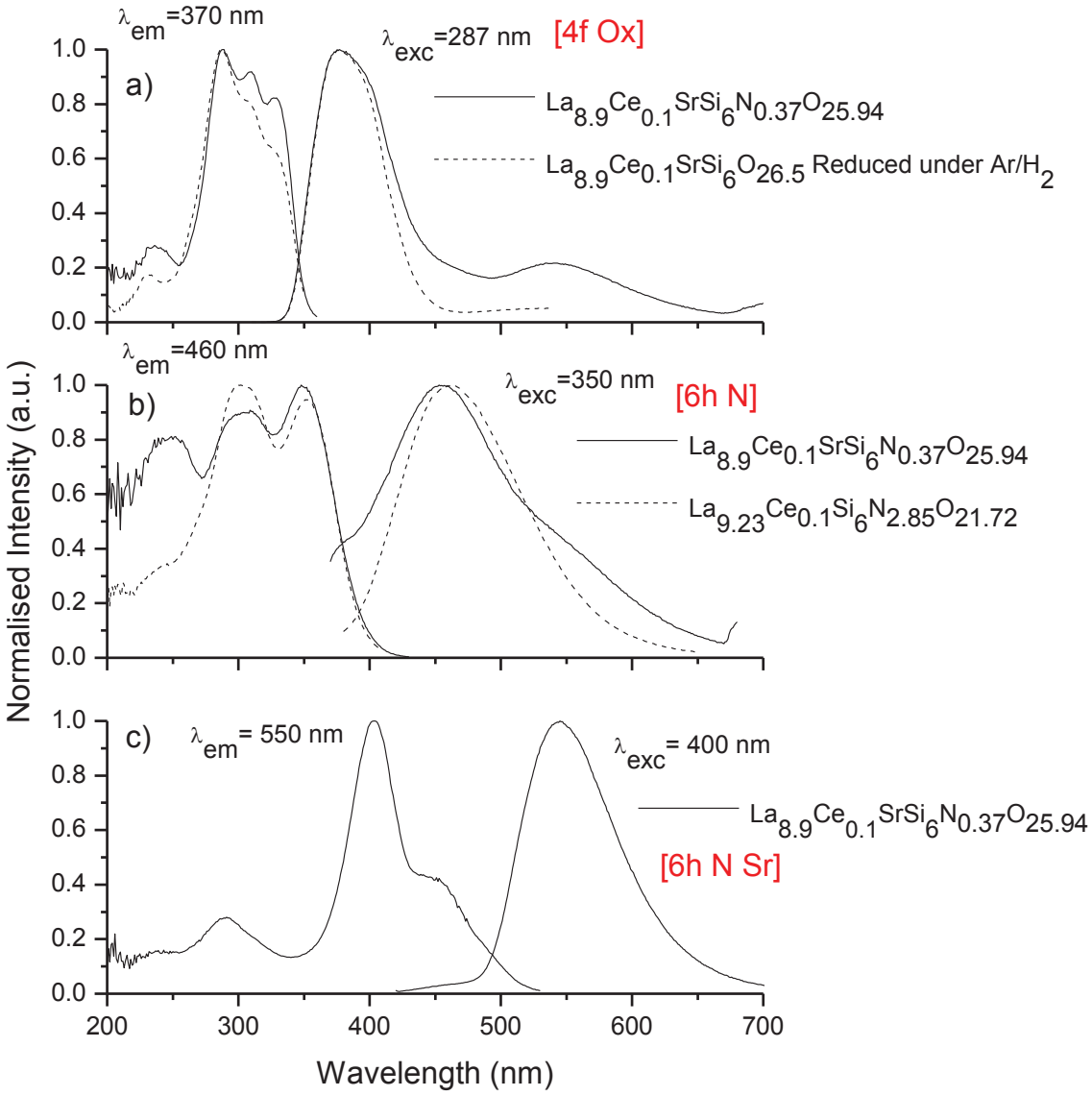

Figure III-13. Luminescence properties at room temperature of cerium doped apatite oxynitride samples with composition $La_{8.9}Ce_{0.1}SrSi_6N_{0.37}O_{25.94}$ (straight line) compared to $La_{9.23}Ce_{0.1}Si_6N_{2.85}O_{21.72}$, and the oxyapatite $La_{8.9}Ce_{0.1}SrSi_6O_{26.5}$ (dashed line) obtained by treatment under Ar/H_2.

The ammonolysis of $La_{8.9}Ce_{0.1}SrSi_6O_{26.5}$ has led to a white body color powder emitting white light under short range UV excitation. By measuring with a spectrofluorimeter many different luminescent features can be observed. In the same way as we proceeded with europium-doped compounds, we compared the optical properties of the nitrided compounds with those of the oxide precursors treated at high temperature under Ar/H_2.

La^{3+} and Ce^{3+} show close ionic radii (For coordination number VII, rLa^{3+}= 1.10 Å and rCe^{3+}= 1.07 Å, and for coordination number IX, rLa^{3+}=1.216 Å and rCe^{3+}=1.196 Å [16]) so it is expected that cerium occupies both 4f and 6h sites in the apatite structure. If we consider the results obtained with Eu-doped compounds, as well as Rietveld refinement carried out on neutron powder diffraction patterns, it seems that nitrogen is mainly affecting 6h sites. As a consequence, three different emissions can be expected from Ce^{3+} in: 4f oxide site, 6h oxide site and 6h nitrided site. As explained in section III.1.4.2. , 4f site is expected to show a lower crystal-field splitting than 6h site, regardless of the nature of the ligands.

Actually, room-temperature measurements have led to observe three different combinations of emission and excitation spectra, which can be related to three different crystallographic sites. $La_{8.9}Ce_{0.1}SrSi_6N_{0.37}O_{25.94}$ showed three different emission bands at 380 nm, 460 nm and 550 nm as can be seen in Figure III-13, each of one having a different excitation spectrum. $La_{8.9}Ce_{0.1}SrSi_6N_{1.06}O_{24.91}$ showed qualitatively the same properties (not shown here). In some cases, no single site emission spectra could have been obtained because of overlapping between the excitation spectra of the three emissions.

Cerium doped apatites with compositions $La_{9.33}Si_6O_{26}$: Ce^{3+} [97] and $La_{10}Si_6O_{24}N_2$: Ce^{3+} [8] have been previously investigated as phosphor materials. In order to carry out our own measurements to investigate the optical properties of $La_{8.9}Ce_{0.1}SrSi_6O_{25.94}N_{0.37}$, we also synthesized these compounds. The optical results we obtained are in agreement with those previous publications.

The first emission band, (Figure III-13.a)) centered at 380 nm can be separated in two Gaussian components positioned at 370 nm and 403 nm, separated by 2094 cm^{-1}, which is close to the energy difference between the $^2F_{5/2}$ and $^2F_{7/2}$ ground state levels of Ce^{3+} (2000 cm^{-1}). This emission is similar to that shown by the sample $La_{8.9}Ce_{0.1}SrSi_6O_{26.5}$ obtained by treatment under Ar/H_2. The coordination polyhedra of cerium at 4f and 6h sites are a tricapped trigonal prism and a pentagonal bipyramid respectively. The anions in the former polyhedron induce a more isotropic crystal field than in the pentagonal bipyramid thus a larger crystal-field splitting is expected for the 6h sites, and the observed short wavelength emission can be attributed to Ce^{3+} in 4f sites in agreement with previous studies of Ce^{3+} activated oxyapatites [97] and oxynitridoapatites [26] [8]. The observed narrow excitation spectrum is consistent with a weak crystal-field splitting of the 5d orbitals. The comparison with the emission of the sample $La_{8.9}Ce_{0.1}SrSi_6O_{26.5}$ obtained by treatment under Ar/H_2,

indicate that nitrogen does not affect significantly this emission. The corresponding site will be referred as [4f Ox] in the following sections.

The second emission band, (Figure III-13.b)) centered at 460 nm, can be compared with the main emission of the strontium-free oxynitridoapatite $La_{9.23}Ce_{0.1}Si_6N_{2.85}O_{21.72}$. It can also be separated in two Gaussian components positioned at 447 nm and 495 nm, separated by 2162 cm^{-1}. This emission is related to the introduction of nitrogen in the host lattice. In agreement with previous studies performed on $La_{10}Si_6O_{24}N_2$: Ce^{3+}, it can be attributed to 6h sites [8] [26]. Given the ratio La/Sr=3 for the 4f sites in $La_{8.9}Ce_{0.1}SrSi_6N_{0.37}O_{25.94}$ or $La_{8.9}Ce_{0.1}SrSi_6N_{1.06}O_{24.91}$, some of the 6h sites could be influenced by strontium at 4f sites. However the similar emission of strontium-free oxynitrido apatite indicates that strontium is not influencing this emission. In $La_{8.9}Ce_{0.1}SrSi_6N_{0.37}O_{25.94}$ and $La_{8.9}Ce_{0.1}SrSi_6N_{1.06}O_{24.91}$, the emission at 460 nm corresponds to the portion of 6h nitrided sites which are not influenced by strontium. The corresponding site will be referred as [6h N] in the following sections.

To the best of our knowledge, the third emission band centered at 545 nm (Figure III-13.c)), has not been previously observed in cerium doped apatite oxides or oxynitrides. It is mainly excited at 400 nm and it is not shown by $La_{8.9}Ce_{0.1}SrSi_6O_{26.5}$ reduced under Ar/H_2. A decomposition of this emission in two Gaussian components separated by 2000 cm^{-1} with the same width was reasonably possible. At long wavelengths the decomposition is difficult because the two Gaussians becomes too wide, and also the component at highest energy is re-absorbed by the excitation spectra. This yellowish green emission is quite remarkable and few Ce^{3+}-doped compounds such as YAG, $La_3Si_6N_{11}$ [39] or $(Sr,Ca)SiN_2$ [44] [45] show luminescence centered beyond 525 nm. In the samples $La_{8.9}Ce_{0.1}SrSi_6N_{0.37}O_{25.95}$ and $La_{8.9}Ce_{0.1}SrSi_6N_{1.06}O_{24.91}$ this long wavelength emission would be related to an important increase of crystal field and covalency (nephelauxetic effect) at Ce^{3+} 6h sites because of nitriding, enhanced by the introduction of strontium in the apatite network. We suggest that the less charged Sr^{2+} positioned in 4f site would lead locally to a displacement of the electron cloud towards the neighboring 6h sites, increasing the crystal-field splitting. Secondly, as Sr^{2+} is larger than La^{3+}, bond distances at 6h sites would locally decrease, increasing even more the crystal-field splitting. The corresponding site will be referred as [6h N Sr] in the following sections.

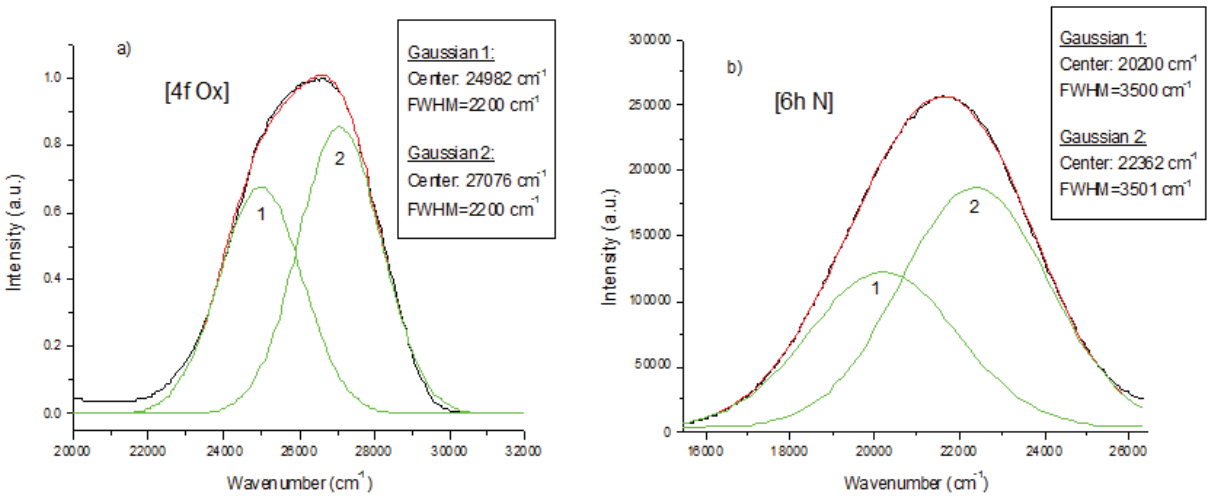

Figure III-14. Gaussian decomposition for the first two emissions centered at a) 380 nm and b) 460 nm of $La_{8.9}Ce_{0.1}SrSi_6N_{0.37}O_{25.94}$.

III.3.1.1.2. Influence of the alkaline-earth

The three different luminescence features observed for the cerium-doped oxynitrides were investigated at room temperature as a function of the alkaline-earth element (Figure III-15). The emissions attributed to Ce^{3+} in [4f Ox] sites and [6h N] sites are similar for barium and strontium-substituted compounds, whereas calcium-substituted compound exhibits emissions with a shift to higher wavelength. The emission attributed to Ce^{3+} in [6h N Sr] sites occurs at shorter wavelength with decreasing alkaline-earth radius. Although La^{3+} and Ca^{2+} show close ionic radii (For coordination number IX, rLa^{3+}=1.216 Å and rCa^{2+}=1.18 Å [16]) it is worth noting that the emission centered at c.a. 545 nm is still observed. Furthermore, the shift corresponding to the variation of alkaline-earth metal is poor. As a consequence, the lower formal charge of the alkaline-earth is certainly the most important factor contributing to this emission at long wavelength that we have only observed in lanthanum alkaline-earth substituted oxynitridosilicates.

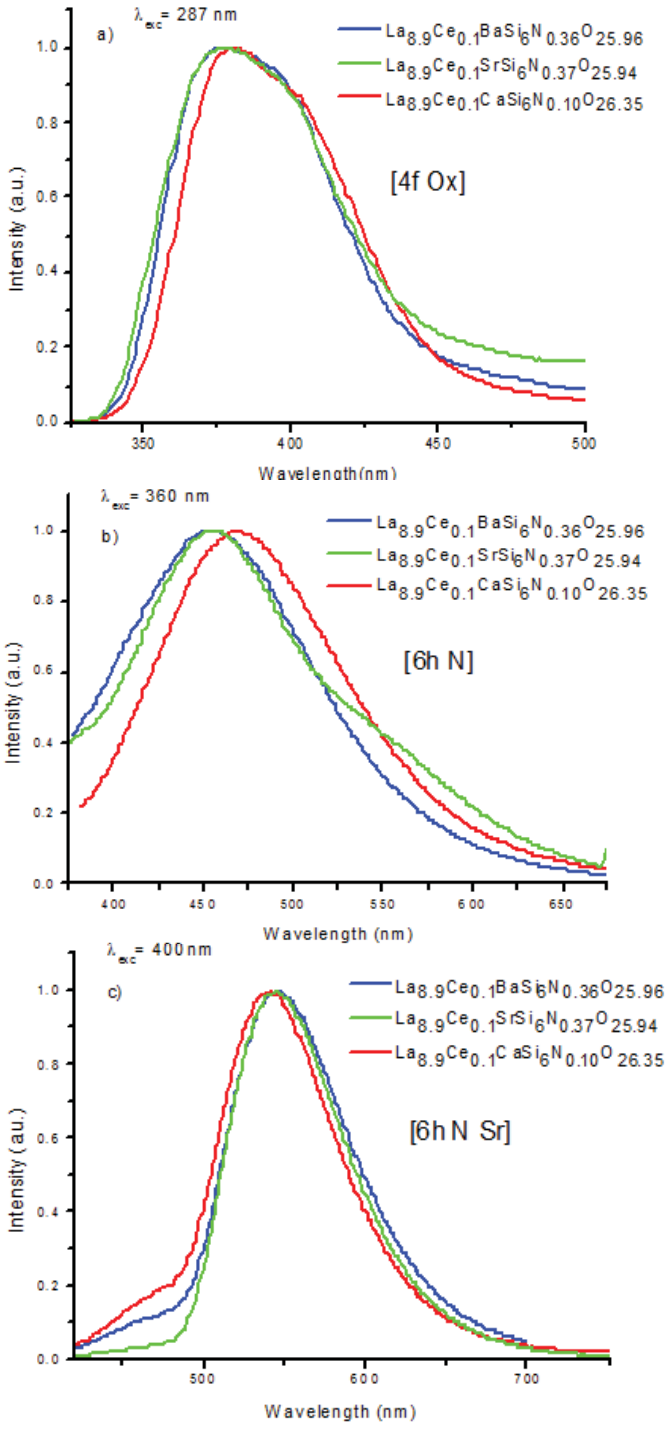

Figure III-15. Emission spectra of the three different sites in $La_{8.9}Ce_{0.1}BaSi_6N_{0.36}O_{25.96}$ (Blue), $La_{8.9}Ce_{0.1}SrSi_6N_{0.37}O_{25.94}$ (Green) and $La_{8.9}Ce_{0.1}CaSi_6N_{0.10}O_{26.35}$ (Red).

The interpretation of the luminescence spectra observed at room-temperature let a question unsolved: if Ce^{3+} is present in both 4f sites and 6h sites, is there any emission of Ce^{3+} in non-nitrided 6h sites? Low-temperature measurements results are described in the following sections to answer this question.

III.3.1.2. Low-temperature measurements

III.3.1.2.1. Study of oxidic compounds reduced under Ar/H_2

In order to find the luminescence of the 6h oxide site ([6h Ox]), we focused on different silicate oxyapatite compound doped with cerium: $La_{9.32}Ce_{0.01}Si_6O_{26}$ and $La_{8.9}Ce_{0.1}SrSi_6O_{26.5}$ reduced under Ar/H_2. At 4.2 K, both compounds present similar luminescent properties (Figure III-16 and Figure III-17). Only two excitation/emission spectra combinations have been observed. The emission that we observed at room-temperature and that we attributed to Ce^{3+} in 4f sites is observed: a band centered around 375 nm where both components of Ce^{3+} luminescence are clearly visible. This separation is in fact easier than at room-temperature because emission bands get generally narrower when the temperature goes down. Excitation spectra, peaking at 287 nm is also very similar to that observed at room-temperature. A second emission was also observed, peaking at 490 nm with a large excitation spectra ranging from 225 nm to 350 nm. This emission was totally quenched at room-temperature and appeared only while measuring at low temperature.

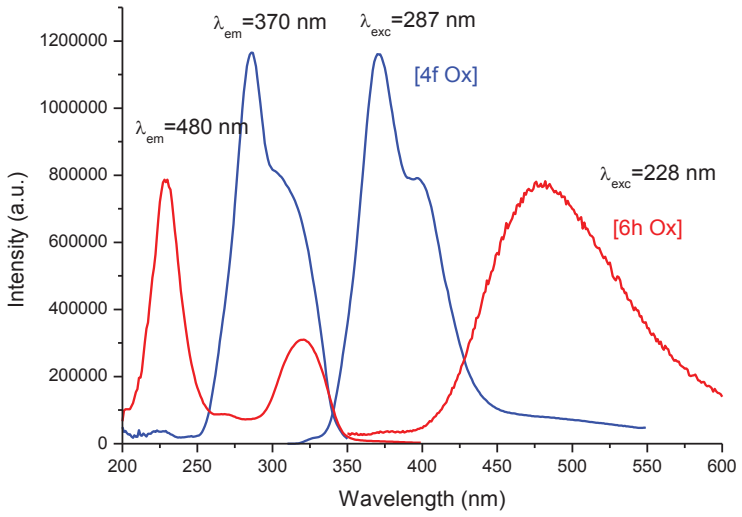

Figure III-16. Excitation and emission spectra at 4.2 K of $La_{9.32}Ce_{0.01}Si_6O_{26}$ reduced under Ar/H_2 : 4f site (blue), and 6h site (red).

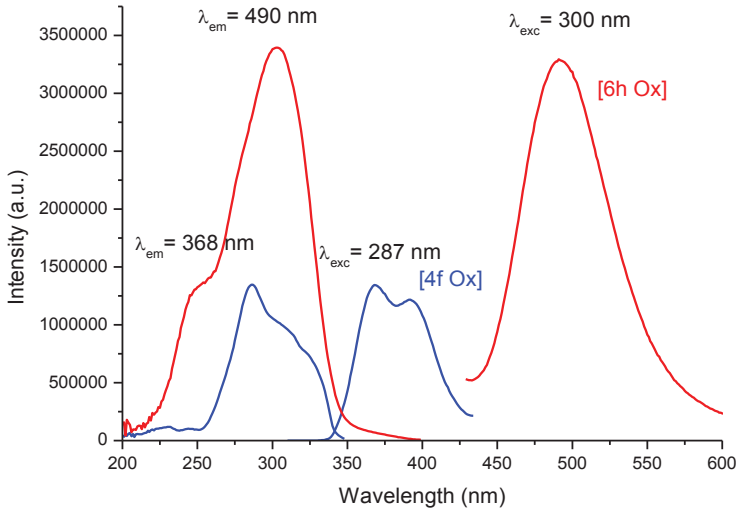

Figure III-17. Luminescence features of $La_{8.9}Ce_{0.1}SrSi_6O_{26.5}$ reduced under Ar/H_2 at liq-He temperature: 4f site (blue), and 6h site (red).

In the two silico-oxyapatite compounds, only two optically active sites are observed. They show excitation and emission spectra that are consistent with our previous analysis: the emission centered at 370 nm shows the narrower excitation spectra that can be assigned to Ce^{3+} in 4f sites. The other emission, at higher wavelength and with wider excitation spectra, can thus be attributed to 6h sites. They will be referred as [6h Ox] sites in the following sections. Presence of strontium in the host lattice modifies slightly the emissions, but does not generate a third emission. The emission attributed to 6h oxide site is shifted 10 nm towards higher wavelength (490 nm compared to 480 nm) whereas the emission of the 4f oxide site is poorly influenced. We believe this is related to the higher interstitial oxygen content δ, increasing the number of ligands coordinated to Ce^{3+} atoms in 6h sites.

III.3.1.2.2. Study of oxynitride compounds

After this analysis of the optical properties of oxides reduced under Ar/H_2 at low-temperature, it was necessary to check the differences with luminescence properties of ammonolyzed compounds at low temperature. The obtained spectra are shown in Figure III-18. We observed again the emission of Ce^{3+} in [4f Ox] sites at 370 nm, the emission of Ce^{3+} in [6h Ox] sites at 490 nm and the emission of Ce^{3+} in [6h N Sr] sites at 545 nm. At 4.2 K, the emission at 490 nm is very intense. One can notice that the excitation band of this emission,

centered at 305 nm, is responsible for the main absorption band observed in the diffuse reflection spectra (Figure III-20 and Figure III-21). The emission at 460 nm, corresponding to Ce^{3+} in [6h N] sites has been observed, but is very difficult to extract. Indeed, the emission at 490 nm is very intense at low temperature, and the corresponding excitation spectra is located in the same range as the excitation spectra of the emission at 460 nm. No single site emission/excitation spectra could have been obtained for the emission at 460 nm.

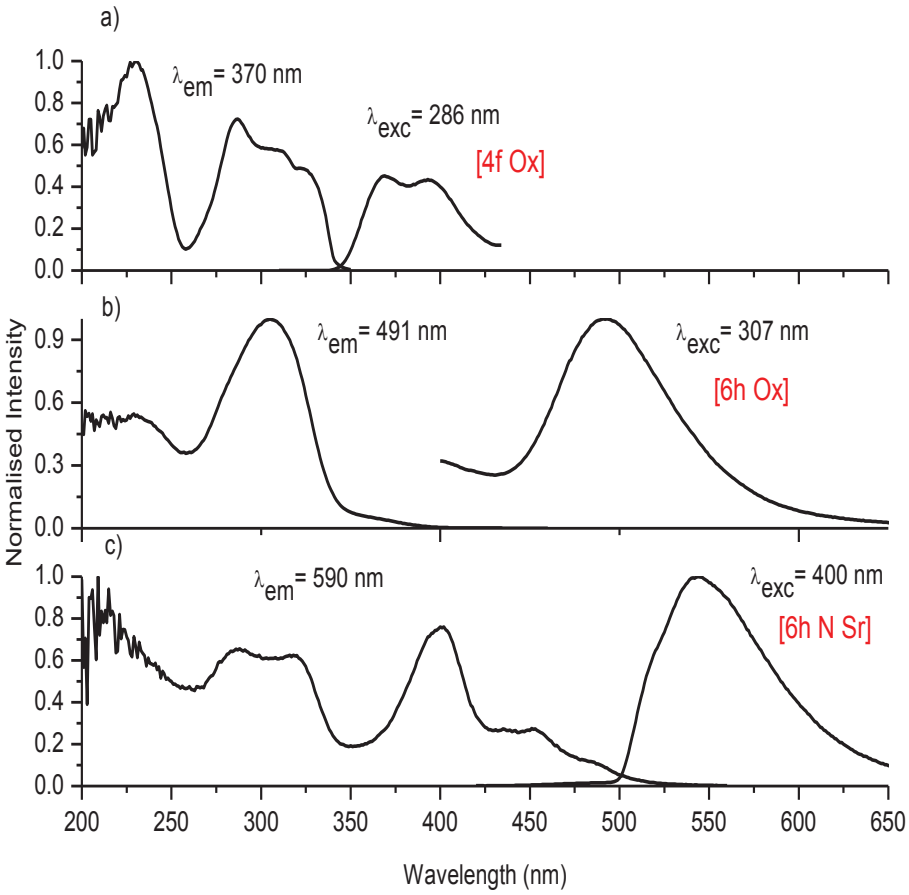

Figure III-18. Measurements for $La_{8.9}Ce_{0.1}SrSi_6N_{0.37}O_{25.94}$ at 4.2 K.

A high energy component (ranging between 200 and 230 nm) is also observed in all excitation spectra. Indeed, exciting in this area gives an emission spectra composed of all emission together (not shown here). We believe that it corresponds to an energy transfer from the host lattice to all the optical centers. This phenomenon is enhanced at low temperature.

III.3.1.2.3. 6h sites: Interpretation of the differences between oxidic and nitrided site

From the measurements at 4.2 K, two main conclusions can be made regarding Ce^{3+} luminescence in 6h sites:

1) After nitriding, the emission of Ce^{3+} in the 6h sites becomes intense at room-temperature ([6h N] and [6h N Sr] in Figure III-13 b) and c)), while it was completely quenched at room-temperature in the oxide compound ([6h Ox] in Figure III-16(Red), Figure III-17(Red) or Figure III-18 b)).

2) The emission of the nitrided site without alkaline-earth influence ([6h N]) is shifted to the shorter wavelength (around 30 nm) compared to the oxide site ([6h Ox]).

Generally, as seen in Chapter I, a red-shifted luminescence is expected for nitride phosphors, notably due to higher crystal-field splitting. Why would it be different in the case of lanthanum silicate apatites? We suggest that this phenomenon is related to the peculiar position of 6h sites regarding the ammonolysis. In chapter II, we have determined that nitrogen is probably going in both silicon tetrahedra position and in the anionic channels along the c-axis. The introduction of nitrogen occurs by substitution of oxygen atoms. The necessity for charge compensation leads to a ratio: two N^{3-} for three O^{2-}. As a consequence, the higher the nitrogen quantity introduced in the channel anions, the lower is the total anion content. For example, ammonolysis of $La_{9.23}Ce_{0.1}Si_6O_{26}$ at 1050°C leads to $La_{9.23}Ce_{0.1}Si_6N_{2.85}O_{21.72}$ which contains a high quantity of anionic vacancies: total anion content change from 26 to 24.85. In the same way, in strontium substituted compounds, ammonolysis of $La_{8.9}Ce_{0.1}SrSi_6O_{26.5}$ at 1050 °C leads to $La_{8.9}Ce_{0.1}SrSi_6N_{1.06}O_{24.91}$ with a total anion content changing from 26.5 to 25.97. Furthermore, ^{29}Si NMR measurements carried out on ammonolyzed and oxide samples suggest a lowering of the interstitial oxygen quantity by nitriding, these anions being coordinated to 6h sites (section II.2.7.). As a consequence, if one considers the influence of nitriding on the crystal-field of these sites, two competing effects have to be taken in account. On one side, the introduction of anions with higher formal charge (N^{3-} compared to O^{2-}) should increase the crystal-field, but on the other side, the total anionic content decreases, decreasing the crystal-field. We have thus observed a blue-shift while introducing nitrogen in the sample.

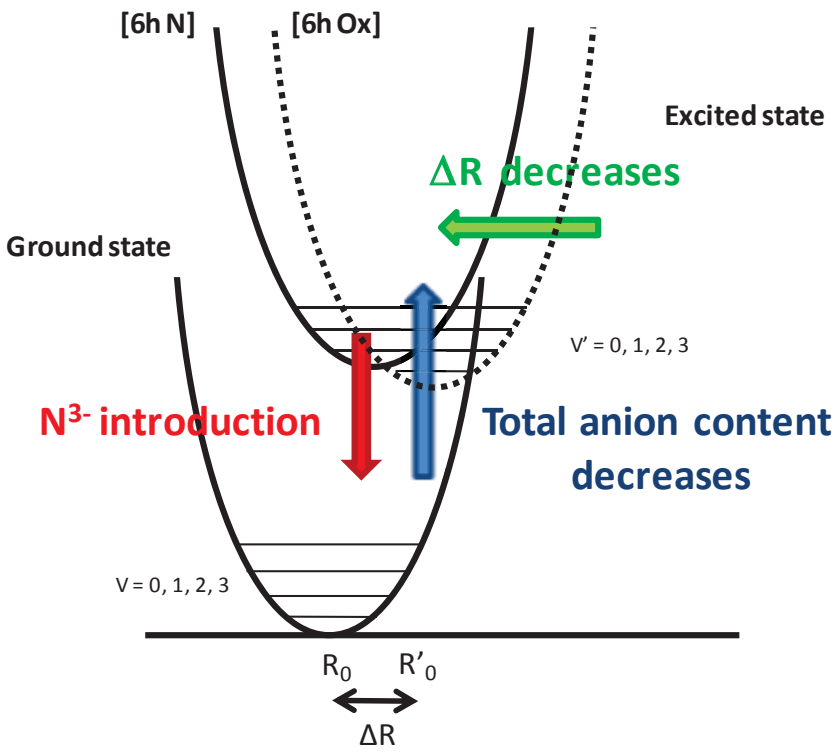

Figure III-19. Scheme for interpretation of the evolution of Ce^{3+} luminescence between 6h oxide (dashed line for excited state) and nitrided site (straight line for excited state).

Several reasons could explain the fact that in oxides, Ce^{3+} emission in 6h sites is quenched at room-temperature, in contrast with that observed for the same sites in nitrided apatites. The Franck-Condon offset (ΔR) might be higher if the optical center is in a softer coordination environment, *i.e.* if the optical center can spatially expand in its excited state compared to the ground state. The relationship between high interstitial oxygen content and high conductivities along the c-axis is well documented [20] [107] [109] [31] [32] [33] [34] . As a consequence, these oxygen atoms can reasonably be considered as mobile, and the surroundings of the luminescent center would be softer. On the other hand, if nitrogen atoms are introduced in the channel anions, one can imagine that these atoms will move less, because they generate more covalent bonding and thus the coordination environment of 6h sites would be stiffer, decreasing ΔR. Furthermore, a decreasing ΔR would be relevant with a shorter emission wavelength, the Stokes Shift automatically decreasing with decreasing ΔR.

III.3.1.3. Improvement of luminescence properties

The luminescence of a phosphor powder is a very sensitive property. It may be affected by many parameters: particle sizes, particle morphologies, crystallite sizes, concentration of dopant. As a consequence, a given phosphor can be optimized by playing on these factors. Focusing on cerium-doped silicate samples, we have carried out experiments in order to determine how this phosphor could be improved. The results of efforts to address this question are contained in the following section.

III.3.1.3.1. Influence of the dopant concentration

Rare-earth dopant concentration may play a decisive role on the luminescence features of a phosphor. Two phenomena are generally distinguishable. First of all, the intensity of a given emission will change drastically with the dopant concentration in the related crystallographic site. Phosphors often show curves of luminescence intensity as a function of concentration of dopant with a maximum for an intermediate value. An increase of the concentration of dopant involves an increase of the number of luminescent centers per unit volume. But at high concentration, a quenching of the luminescence can occur and counterbalances the first effect. Concentration quenching can be explained this way: the closer the luminescent centers are one to each other, the more they will show interaction. One center can reabsorb the energy of another center. If the distance between luminescent centers is shorter enough (less than 25 Å typically), the absorbed energy can transfer from site to site until meeting a defect or an entity allowing a non-radiative return to the ground state. [35]

The second phenomenon which can also occur with concentration variation is a qualitative variation of the emission spectra. Indeed, if several crystallographic sites are available for the dopant, at very low concentration preferential occupation for one site leads to a single site emission and an increase of the concentration can generate a broadening of the spectral distribution corresponding to the emissions of the different sites.

Regarding Ce-doped lanthanum strontium oxynitrido silico-apatites we have worked for instance with $La_{8.9}Ce_{0.1}SrSi_6N_{0.37}O_{25.94}$ and $La_{8.9}Ce_{0.1}SrSi_6N_{1.06}O_{24.91}$. Their formula correspond to a doping concentration of 1.7 10^{20} at.cm^{-3} (a value determined by considering a unit cell volume of 590.07 Å^3). This value can be considered as intermediate for a phosphor, while concentrations of the order of magnitude 10^{19} at.cm^{-3} are considered very low and concentrations of the order of magnitude 10^{21} at.cm^{-3} are considered as high concentrations.

For practical reasons, we have not been able to test enough cerium doping concentration with compounds synthesized exactly in the same conditions in order to obtain the concentration dependence of the luminescence. Nevertheless we have observed a trend while looking at couples of samples with different concentrations: with decreasing cerium concentration, the intensity of the emission attributed to Ce^{3+} in [4f Ox] sites decreases whereas the intensity of the emission attributed to Ce^{3+} in [6h N Sr] sites increases.

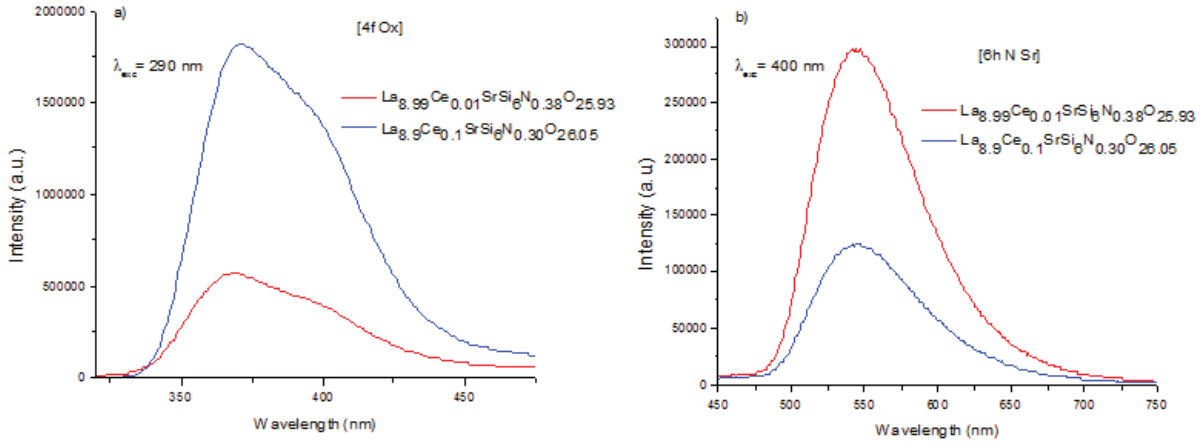

Figure III-20. Emission spectra of $La_{8.99}Ce_{0.01}SrSi_6N_{0.38}O_{25.93}$ and $La_{8.9}Ce_{0.1}SrSi_6N_{0.30}O_{26.05}$ for an excitation at a) 290 nm and b) 400 nm.

In diffuse reflection spectra for two samples with different concentrations of cerium (Figure III-21), it appears that the maximum absorption (at 320 nm) corresponds to the excitation of the emission of 6h oxide site. Absorption at 400 nm, corresponding to the maximum of excitation for an emission at 545 nm is also observed but in lower proportion. While increasing the Ce concentration, 6h oxide site absorption gets more important and the onset of the band overlap with the absorption at 400 nm. We suggest that too high Ce concentrations give rise to a high number of Ce^{3+} in 6h oxide sites with high absorption but no emission at room-temperature. The multiplication of these sites would automatically decrease the other emission intensities by competing with them during the absorption step.

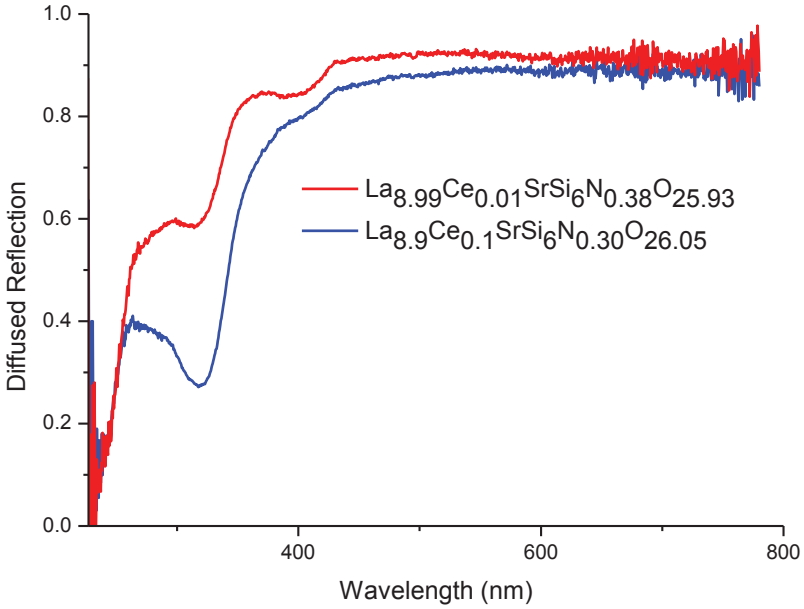

Figure III-21. Diffuse Reflection Spectra for two samples with different cerium concentrations

III.3.1.3.2. Influence of the ammonolysis conditions

III.3.1.3.2.1. Influence of highly nitriding conditions

We have seen in Chapter II that the quantity of introduced nitrogen could be increased by increasing temperature of treatment and $NH_{3(g)}$ flow. Indeed, in the case of lanthanum strontium silicate oxynitrides Eu-doped nitrogen quantity was brought from 0.60 per formula to 1.77 per formula after nitriding at 800°C and 1050°C respectively. In the case of Ce-doped compounds, nitrogen quantity was brought from 0.37 to 1.06. No qualitative difference could be observed for luminescence spectra, but a decrease of all emission's intensity was observed for both Ce-doped and Eu-doped samples obtained at higher temperatures of ammonolysis.

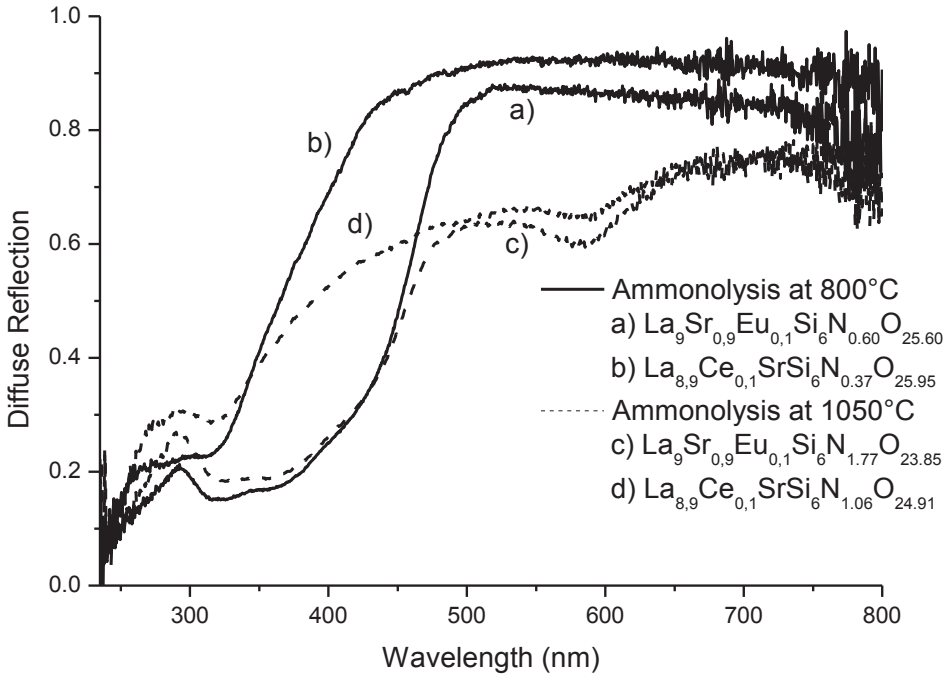

Figure III-22. Diffuse reflection spectra of Eu and Ce-doped compounds ammonolysed at 800 °C-20 h-350 ml/min (Solid line) a) $La_9Sr_{0.9}Eu_{0.1}Si_6N_{0.60}O_{25.60}$, b) $La_{8.9}Ce_{0.1}SrSi_6N_{0.37}O_{25.95}$ and at 1050 °C-20 h-660 ml/min (Dashed line) c) $La_9Sr_{0.9}Eu_{0.1}Si_6N_{1.77}O_{23.85}$ and d) $La_{8.9}Ce_{0.1}SrSi_6N_{1.06}O_{24.91}$.

Figure III-22 shows the diffuse reflection spectra of the different lanthanum strontium silicate compounds ammonolyzed at 800 °C and 1050 °C. For both europium and cerium doped oxynitride apatites the samples treated in NH_3 at 1050 °C showed a greyish body colour compared to the samples treated at 800 °C. A higher absorption between 450 and 800 nm, far from the excitation spectra, is observed for the highest temperature of ammonolysis. Creation of colour centers or defects could be responsible for this phenomenon that is detrimental to the luminescence. An important re-absorption of the emission occurs for the samples treated at 1050 °C.

III.3.1.3.2.2. Influence of cooling rate

Two different cooling conditions were used: fast cooling and slow cooling. In the first case, after ending the plateau step at the highest temperature, the sample was quenched by removing the tube from the furnace. This was made possible by using split-type furnaces (see experimental set-up in section II.1.5.1.). Depending on ammonolysis temperature, fast cooling

down to room temperature could last between 20 and 30 minutes. Cooling took place under a static ammonia gas atmosphere. Slow cooling has been used as a general technique in this work.

For slow cooling experiments, the sample was simply let in the tube, cooling with the furnace, under ammonia flow. Furnace cooling speed at the highest temperature (beginning of the cooling step) was 300 °C/h and progressively decreased while approaching room temperature.

We have compared the effect of slow cooling and quenching on the same precursor oxide $La_{8.9}Ce_{0.1}SrSi_6O_{26.5}$ after treating the sample under flowing $NH_{3(g)}$ at 800°C during 20 hours with a flow rate of 350 ml/min. We have observed higher intensities for all emissions after slow cooling compared to fast cooling. Nitrogen content was 0.37 in the case of fast cooling and 0.16 in the case of slow cooling. By using the Scherrer equation [36] in the related X-ray patterns no difference of crystallite sizes has been found between the two samples. This experiment has been carried out twice, leading to equivalent observations. Nevertheless, these results have to be taken carefully because for practical reasons, the two cooling rates have not been used with the exact same experimental set-up. Differences of tube diameter and temperature calibration between the experimental set-ups can have drastic effects on the final sample obtained.

Diffuse reflection spectra (Figure III-23) show that the sample obtained after fast cooling show a higher absorption in the range 350-540 nm than the sample obtained after slow cooling. A higher re-absorption of the light emitted by the sample explains the lower emission intensities observed. It is possible that slow cooling lead to less surface defect than fast cooling. Quantum efficiencies have been measured for the sample obtained by slow cooling (section III.3.1.2.3.).

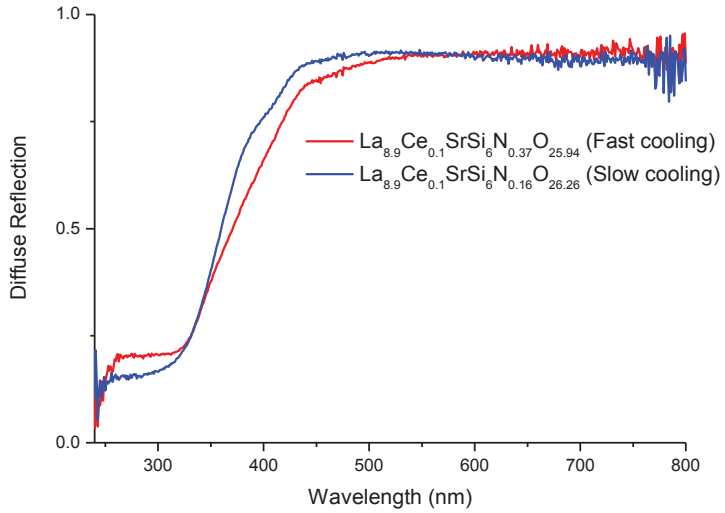

Figure III-23. Diffuse reflection spectra of two samples obtained after ammonolysis of the same oxide precursor $La_{8.9}Ce_{0.1}SrSi_6O_{26.5}$, ending by slow cooling (Blue) or fast cooling (Red).

III.3.1.3.3. External/Internal quantum efficiency and thermal quenching

In order to determine the potential of cerium-doped lanthanum strontium oxynitrido-silicates as phosphor materials, their external and internal quantum efficiencies have been measured. We have focused on the emission at 545 nm as it is the emission at longest wavelength in this compound, and thus the most interesting for application in white LEDs.

External quantum efficiency (EQE) is the ratio of emitted photons to the quantity of photons received by the sample. Quantum efficiencies have been obtained by measurements relative to two standards from the National Bureau of Standards (NBS): NBS1026 ($CaWO_4$: Pb^{2+}) and NBS1028 (Zn_2SiO_4: Mn^{2+}). They can be excited in a charge transfer band at 260 nm and show wide emission bands centered at 445 nm and 530 nm for NBS1026 and NBS1028 respectively. Their absolute external quantum efficiencies have been determined by the NBS to be 71%. The complete spectral distributions of our samples and NBS standards have been acquired in the same conditions (same spectrofluorimeter and same slit sizes) with a detector (photomultiplier tube) working in photon counting mode. Excitation wavelengths have been selected considering the excitation maxima for each emission: 400 nm for our samples and 260 nm for NBS standards. All the spectral distributions were fully corrected: the spectral response of the spectrofluorimeter in excitation and emission was taken in account, as well as the variations of the lamp flux with the wavelength. In these conditions, the ratio of the

integrated spectral distributions is equal to the ratio of their EQE and the EQE of our samples can be deduced:

$$\frac{Sample\ Emission}{NBS\ Emission} = \frac{Sample\ EQE}{NBS\ EQE}$$

Internal quantum efficiency (IQE) is the ratio of emitted photons to the quantity of photons absorbed by the sample. It thus takes in account the absorption of the sample at the excitation wavelength. Absorption can be deduced from diffuse reflection spectra and the IQE can be calculated:

$$IQE = \frac{EQE}{a} = \frac{EQE}{1 - 0.97D}$$

Table III-2 shows EQE and IQE for three selected samples. All efficiencies are relatively low. It is possible to determine which factors are deciding for the low IQE observed. We will take the example of $La_{8.99}Ce_{0.01}SrSi_6N_{0.38}O_{25.93}$ which shows the best IQE.

$La_{8.99}Ce_{0.01}SrSi_6N_{0.38}O_{25.93}$ shows a total absorption of 19.4 % at 400 nm (Figure III-20). This absorption is not only due to [6h N Sr] site absorption, but also to the general absorption of the sample, which can be deduced by looking at the absorption of the sample from 500 nm to 800 nm and is equal to 9.8%. The absorption only relative to the Ce^{3+} ions in the sites associated with this emission is thus equal to a_{Ce}=9.6%. Hence, it is possible to evaluate the IQE relative to the cerium atoms involved in this emission:

$$IQE_{Ce} = \frac{EQE}{a_{Ce}} = 35.4\%$$

The ratio between the integrated emission spectra at liquid helium temperature and room temperature is equal to 2.33. A decrease of 42.3 % can thus be associated with a quenching of the luminescence related with temperature. To finish, it can be considered that 9.8% of the emitted photons are re-absorbed by the sample (absorption between 500 nm and 800 nm). In conclusion, c.a. 90% of the whole process from absorption to emission has been described and we have identified the two main limiting factors responsible for the low EQE observed:

-A marked temperature quenching

- A weak cerium absorption

It is worth noting that the weak absorption is probably due to the small number of cerium atoms in [6h N Sr] sites.

Table III-2. External and internal quantum efficiencies for an excitation at 400 nm of three silicate samples

Sample	External Quantum Efficiency (λ_{exc}= 400 nm)	Absorption (λ = 400 nm)	Internal Quantum Efficiency (λ_{exc}= 400 nm)
$La_{8.9}Ce_{0.1}SrSi_6N_{0.37}O_{25.94}$ (Quenching)	2.7 %	36%	7.5 %
$La_{8.9}Ce_{0.1}SrSi_6N_{0.15}O_{26.27}$ (Slow cooling)	3.5 %	27%	13 %
$La_{8.99}Ce_{0.01}SrSi_6N_{0.38}O_{25.93}$ (Quenching)	3.4 %	19.4%	17.5 %

III.3.2. Cerium-doped germanates

III.3.2.1. Luminescence at room-temperature

Ce-doped germanates were also investigated. $La_{9.9}Ce_{0.1}Ge_6N_{2.46}O_{23.31}$ showed only one emission band at room temperature (Figure III-24) centered at 590 nm (orange) with three corresponding excitation bands centered at 290, 390 and 480 nm. As stated in Chapter II (section II-2.6.1.), some strontium have been found lately by carrying out ICP-AES measurements on this sample. A ratio La/Sr=9.64/0.55 has been found.

In order to determine whether this luminescence was related to nitrogen introduction or not, the corresponding oxide precursor $La_{9.9}Ce_{0.1}Ge_6O_{27}$ was also reduced under $Ar/H_{2(g)}$ at 600°C (this temperature was chosen lower than with silicates in order to avoid damaging the sample). No luminescence has been observed at room-temperature for the sample obtained, which led to conclude that the emission at 590 nm was actually related to nitrogen introduction.

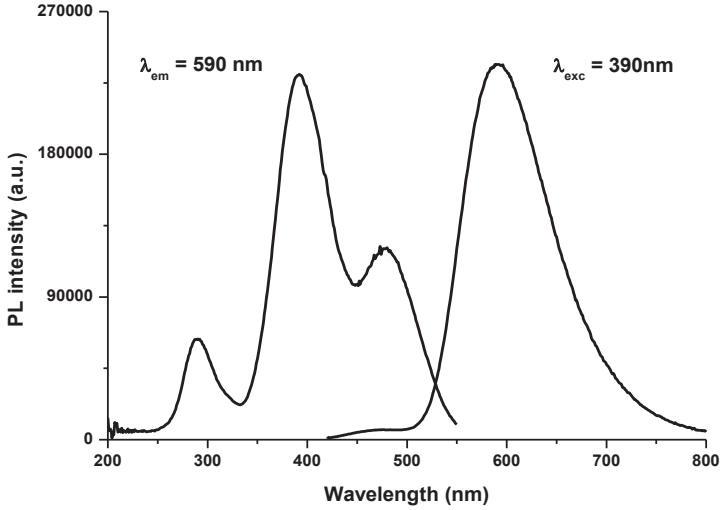

Figure III-24. Excitation and emission spectra of $La_{9.9}Ce_{0.1}Ge_6N_{2.46}O_{23.31}$ at room temperature.

III.3.2.2. Luminescence at low-temperature

Luminescence measurements at liquid helium temperature with these two samples were carried out. For the oxynitride $La_{9.9}Ce_{0.1}Ge_6N_{2.46}O_{23.31}$, three different combinations of excitation/emission spectra have been observed (Figure III-25):

- An emission with a maximum at 425 nm which can be excited in a wide band ranging from 250 nm to 350 nm.

- An emission with a maximum at 525 nm which can be excited in a band with a maximum at 255 nm.

- An emission similar to the emission observed at room temperature.

It was possible to decompose the emission spectra in order to find the two components of Ce^{3+} emission for the first and third emission, separated by 2000 cm^{-1} and 1800 cm^{-1} respectively (Figure III-26). The second emission was more difficult to decompose because no selective excitation could be found. Indeed, the emission band resulting from an excitation at 255 nm also contains a part of the emission band at 590 nm.

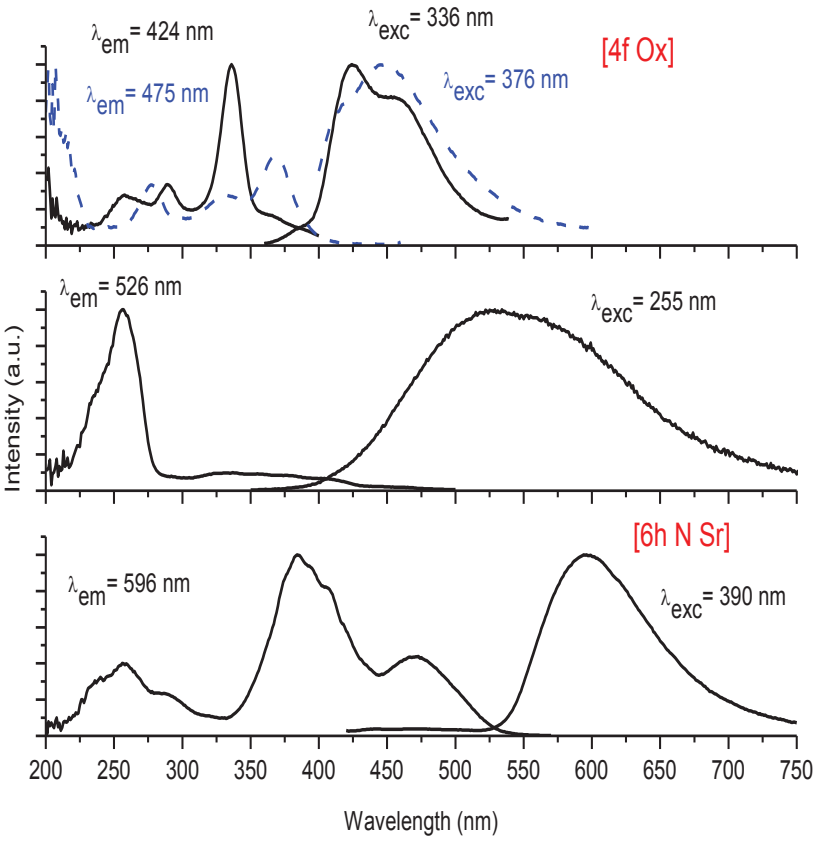

Figure III-25. Luminescence spectra at liquid helium temperature of $La_{9.9}Ce_{0.1}Ge_6N_{2.46}O_{23.31}$ (straight line), and $La_{9.9}Ce_{0.1}Ge_6O_{27}$ reduced under Ar/H_2 (blue dashed line).

$La_{9.9}Ce_{0.1}Ge_6O_{27}$ reduced under Ar/H_2 showed several emissions, but only one which can be compared with the observed luminescence features of $La_{9.9}Ce_{0.1}Ge_6N_{2.46}O_{23.31}$: the emission centered at *c.a.* 450 nm. The other emission bands were centered at lower wavelength (not shown here). Changes in symmetry between oxides and nitrided samples (from monoclinic to hexagonal) could explain these differences.

By analogy with cerium-doped silicate samples, we can assign the different couples of excitation/emission spectra. The emissions at 425 nm and 590 nm can be attributed to 4f oxide site ([4f Ox]) and 6h nitrided site with strontium influence ([6h N Sr]) respectively. The 6h nitrided site with no influence coming from strontium atoms [6h N] and the 6h oxide site [6h Ox] would be localized in the 500-550 nm range. Compared to silicates, it is worth noting that all corresponding emissions in germanates are red-shifted.

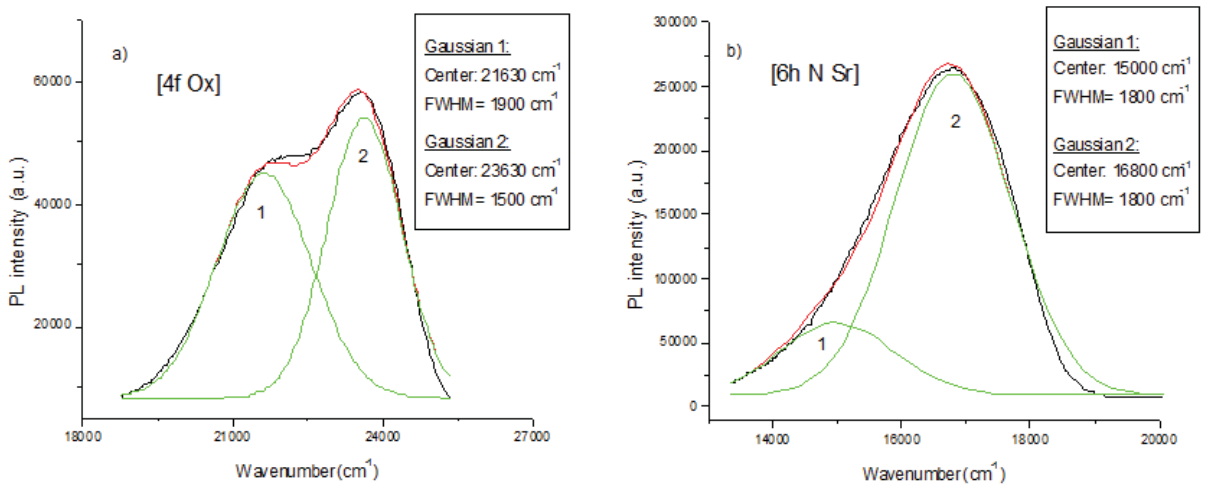

Figure III-26. Gaussian decomposition for the first and third emission centered at a) 445 nm and b) 590 nm of $La_{9.9}Ce_{0.1}Ge_6N_{2.46}O_{23.31}$.

Diffuse reflection spectrum of $La_{9.9}Ce_{0.1}Ge_6N_{2.46}O_{23.31}$ (Figure III-27) does not show absorption at 400 nm. On the other side, a high absorption is visible at around 325 nm, which correspond to the maximum of excitation of the emission of 4f oxide sites (445 nm). It can be deduced that as in the silicates, the main absorption in this sample is due to the 6h oxide sites, and that the quantity of sites emitting at 590 nm is actually very small.

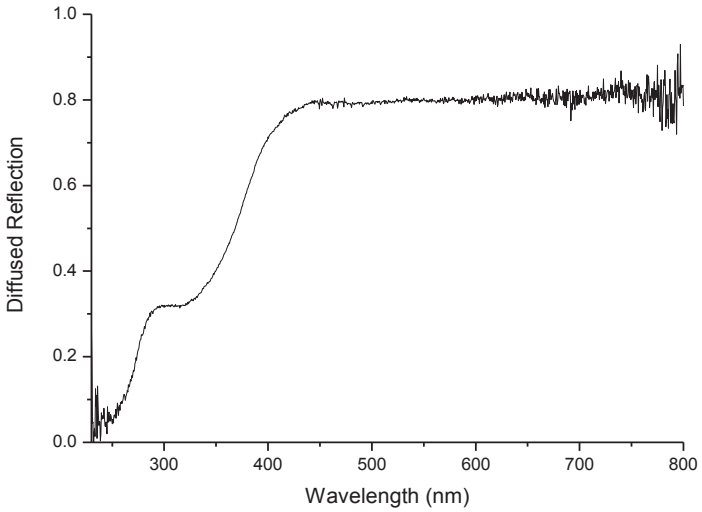

Figure III-27. Diffuse reflection spectra of $La_{9.9}Ce_{0.1}Ge_6N_{2.46}O_{23.31}$.

III.3.2.3. Study about the luminescence of La_2GeO_5: Ce^{3+}

While synthesizing $La_{9.9}Ce_{0.1}Ge_6O_{23.31}N_{2.45,}$ X-ray diffraction pattern showed a non-negligible content of impurity which set of diffraction peaks can be attributed to La_2GeO_5. In order to be sure that this impurity was not responsible for any observed luminescence, we synthesized the following compound: $La_{1.98}Ce_{0.02}GeO_5$. The concentration of dopant relative to the total lanthanum content is equivalent between $La_{9.9}Ce_{0.1}Ge_6O_{23.31}N_{2.45}$ and $La_{1.98}Ce_{0.02}GeO_5$. After ammonolysis in the same conditions as with the germanate oxide precursor (600°C-20h-660mL/min) this sample was not showing any luminescence under UV/Blue lamp irradiation. A TGA carried out on this sample showed no weight gain, indicating that no nitrogen had been introduced by ammonolysis. It ensues that the luminescence observed could not be attributed to this impurity.

III.4. Summary and Conclusions of the chapter

A study of the luminescent properties of the Ce^{3+} and Eu^{2+}-doped oxynitride silicate and germanate samples has been proposed. By comparison with samples reduced under Ar/H_2 it has been possible to assign the different luminescence features observed to the different crystallographic sites available in the apatite structure, together with an interpretation of the influence of the nitrogen introduction.

For lanthanum strontium-substituted silicate samples doped with Eu^{2+} of composition $La_9Sr_{0.9}Eu_{0.1}Si_6N_{0.60}O_{25.60}$ and $La_9Sr_{0.9}Eu_{0.1}Si_6N_{1.77}O_{23.85}$, it has not been observed any qualitative modification of the emission spectra compared to $La_9SrSi_6O_{26.5}$: Eu^{2+} reduced under Ar/H_2. The emission observed has been attributed to 4f sites. A study of the luminescence features of Eu^{3+} in trace amounts is coherent with the introduction of nitrogen within the channels.

For lanthanum strontium-substituted germanate samples doped with Eu^{2+} of the following composition: $La_{9.5}Sr_{0.4}Eu_{0.1}Ge_6N_{1.42}O_{24.62}$, no luminescence feature has been observed.

Lanthanum strontium-substituted silicate samples doped with Ce^{3+} of composition $La_{8.9}Ce_{0.1}SrSi_6N_{0.37}O_{25.94}$ or $La_{8.9}Ce_{0.1}SrSi_6N_{1.06}O_{24.91}$ show several emission/excitation spectra combination at room temperature due to the several crystallographic sites available for

Ce^{3+} in the host lattice. The emission at 380 nm (Violet) has been attributed to 4f sites. The emission at 460 nm (Blue) has been attributed to 6h sites influenced by nitrogen introduction. To finish, the emission at 545 nm has been attributed to 6h sites influenced by nitrogen introduction together with a local structure modification brought by strontium atoms located in 4f sites. A fourth emission has been found only at low temperature which has been attributed to 6h sites with no nitrogen atoms in the coordination polyhedra.

All oxynitridosilicate samples show low external quantum efficiencies. A marked thermal quenching has been identified. The absorption corresponding to the emission at 545 nm is small, which has been correlated with the few number of corresponding crystallographic sites in the structure.

In cerium doped oxynitride germanate samples, an emission at 590 nm (orange) has been found. By analogy with silicates, this emission has also been related to local structural modifications brought by strontium atoms.

Table III-3. Summary of the main samples investigated with associated luminescent features at room-temperature

Sample	Excitation (nm)	Emission (nm)
$La_9Sr_{0.9}Eu_{0.1}Si_6N_{0.60}O_{25.60}$	325-425 nm	513 nm
$La_{8.9}Ce_{0.1}SrSi_6N_{0.37}O_{25.94}$	280-325 nm	380 nm
$La_{8.9}Ce_{0.1}SrSi_6N_{0.37}O_{25.94}$	240-350 nm	460 nm
$La_{8.9}Ce_{0.1}SrSi_6N_{0.37}O_{25.94}$	400 nm	545 nm
$La_{9.9}Ce_{0.1}Ge_6N_{2.46}O_{23.31}$	390 nm	590 nm

References for Chapter III:

[1] Mott, N. F. *Proceedings of the Royal Society A* **167**, 384–391 (1938).

[2] Kiel, A. *Proceedings of the Third International Conference on Quantum Electronics* , 765 (1963).

[3] Struck, C. W. and Fonger, W. H. *Journal of Luminescence* **10**, 1–30 (1975).

[4] Blasse, G., Schipper, W., and Hamelink, J. *Inorganica Chimica Acta* **189**(1), 77 – 80 (1991).

[5] Yen, W., Raukas, M., Basun, S., van Schaik, W., and Happek, U. *Journal of Luminescence* **69**(5-6), 287 – 294 (1996).

[6] Pidol, L., Viana, B., Galtayries, A., and Dorenbos, P. *Physical Review B* **72**, 125110 (2005).

[7] Verwey, J., Dirksen, G., and Blasse, G. *Journal of Physics and Chemistry of Solids* **53**(3), 367 – 375 (1992).

[8] Huheey, J. E., Keiter, E. A., and Keiter, R. L. *Chimie Inorganique*. (1993).

[9] van Krevel, J., Hintzen, H., Metselaar, R., and Meijerink, A. *Journal of Alloys and Compounds* **268**(1-2), 272 – 277 (1998).

[10] Lin, J. and Su, Q. *Journal of Materials Science* **5**, 1151 (1995).

[11] Lammers, M. J. J. and Blasse, G. *Journal of the Electrochemical Society* **134**, 2068–2072 (1987).

[12] Dierre, B., Xie, R.-J., Hirosaki, N., and Sekiguchi, T. *Journal of Materials Research* **22**(7), 1933–1941 (2007).

[13] Iwata, T., Fukuda, K., Béchade, E., Masson, O., Julien, I., Champion, E., and Thomas, P. *Solid State Ionics* **178**(27-28), 1523 – 1529 (2007).

[14] Shannon, R. D. *Acta Crystallographica Section A* **32**, 751–767 (1976).

[15] Masubuchi, Y., Higuchi, M., Takeda, T., and Kikkawa, S. *Solid State Ionics* **177**, 263–268 (2006).

[16] Lambert, S., Vincent, A., Bruneton, E., Beaudet-Savignat, S., Guillet, F., Minot, B., and Bouree, F. *Journal of Solid State Chemistry* **179**, 2602–2608 (2006).

[17] Sansom, J. E. H., Richings, D., and Slater, P. R. *Solid State Ionics* **139**, 205–210 (2001).

[18] Pauling, L. *Journal of the American Chemical Society* **51**, 1010–1026 (1929).

[19] Cui, Z.-F., Yuan, S.-L., Yang, Y.-X., Cheviré, F., Tessier, F., and Chen, G.-R. *Chinese Physics Letters* **28**(1), 014209 (2011).

[20] Li, Y. Q., Delsing, A. C. A., de With, G., and Hintzen, H. T. *Chemistry of Materials* **17**(12), 3242–3248 (2005).

[21] Zhang, X., Zhang, J., Huang, J., Tang, X., and Gong, M. *Journal of Luminescence* **130**, 554–559 (2010).

[22] Yamashita, N. *Journal of the Electrochemical Society* **140**, 840–843 (1993).

[23] Yamashita, N. *Journal of Luminescence* **59**, 195–199 (1994).

[24] Jia, D. and jun Wang, X. *Optical Materials* **30**(3), 375 – 379 (2007).

[25] Ouenzerfi, R. E., Panczer, G., Goutaudier, C., Cohen-Adad, M., Boulon, G., Trabelsi-Ayedi, M., and Kbir-Ariguib, N. *Optical Materials* **16**(1-2), 301–310 (2001).

[26] Seto, T., Kijima, N., and Hirosaki, N. *ECS Transactions* **25**(9), 247–252 (2009).

[27] Duan, C. J., Wang, X. J., Otten, W. M., Delsing, A. C. A., Zhao, J. T., and Hintzen, H. T. *Chemistry of Materials* **20**(4), 1597–1605 (2008).

[28] Toquin, R. L. and Cheetham, A. *Chemical Physics Letters* **423**(4-6), 352 – 356 (2006).

[29] Leon-Reina, L., Martin-Sedeño, M. C., Losilla, E. R., Cabeza, A., Martinez-Lara, M., Bruque, S., Marques, F. M. B., Sheptyakov, D. V., and Aranda, M. A. G. *Chemistry of Materials* **15**(10), 2099–2108 (2003).

[30] Leon-Reina, L., Losilla, E. R., Martinez-Lara, M., Bruque, S., and Aranda, M. A. G. *Journal of Materials Chemistry* **14**, 1142–1149 (2004).

[31] Leon-Reina, L., Porras-Vazquez, J. M., Losilla, E. R., and Aranda, M. A. *Solid State Ionics* **177**(15-16), 1307 – 1315 (2006).

[32] Leon-Reina, L., Losilla, E. R., Martinez-Lara, M., Bruque, S., Llobet, A., Sheptyakov, D. V., and Aranda, M. A. G. *Journal of Materials Chemistry* **15**, 2489–2498 (2005).

[33] Leon-Reina, L., Porras-Vazquez, J. M., Losilla, E. R., Sheptyakov, D. V., Llobet, A., and Aranda, M. A. G. *Dalton Transactions* , 2058–2064 (2007).

[34] Leon-Reina, L., Porras-Vazquez, J. M., Losilla, E. R., and Aranda, M. A. *Journal of Solid State Chemistry* **180**(4), 1250 – 1258 (2007).

[35] Dexter, D. L. and Schulman, J. H. *The Journal of Chemical Physics* **22**, 1063–1070 (1954).

[36] Patterson, A. L. *Phys. Rev.* **56**, 978–982 Nov (1939).

.

General Conclusion

General Conclusion:

The main initial aim of this thesis was to prepare and to study luminescent materials with potential application in Solid State Lighting (White PC-LED). New luminescent oxynitrides based on the apatite structure doped with Eu^{2+}or Ce^{3+} have been prepared. The hosts compounds have the general formula $La_{10-x}Sr_x(Si/Ge)_6N_yO_{27-x/2-3/2y}$.The treatment of precursor oxides with the required cationic ratio in NH_3(g) was used as a convenient general method to prepare the oxynitride materials at moderate temperatures. This allowed decreasing the nitriding temperature from 1600-1400 °C to 1050-600 °C with respect to the method generally used for the luminescent (oxy)nitride silicates: the solid-state-reaction between oxides, nitrides and carbonates under N_2 or N_2/H_2 flow.

A second objective has consisted in a detailed study of their luminescent properties with a substantial effort addressed to understand the relationships between the structural modifications brought by nitrogen introduction and the related luminescence properties observed.

In the first chapter, the bibliographic study has allowed highlighting the potential of lanthanum apatite compounds as oxynitride phosphors. The flexibility of this structure, as well as the diversity of available crystallographic sites makes it an interesting subject of investigation. A main focus has been directed towards oxynitridosilicate apatite phosphors.

The second chapter illustrates the numerous characterization techniques that have been used during this thesis. Nitrogen contents have been determined by TGA and combustion analysis. Nitrogen distribution in a particle has been found homogeneous by Auger spectroscopy and electron microprobe analysis. In the apatite structure, two anionic positions are available for nitrogen atoms: in silicon tetrahedra and in channel sites. A study of the localization of nitrogen atoms in the crystal structure has been carried out. Raman and Infrared spectroscopy measurements, compared with *ab initio* simulations indicate that silicon tetrahedra environment is directly affected by nitrogen atoms introduction. NMR ^{29}Si studies have also been carried out which confirm that nitrogen introduction mechanism is related to the loss of interstitial oxygen in the channels of the structure. The study by neutron diffraction

of an oxynitridosilicate sample has led to place nitrogen atoms in both the silicon tetrahedra and the channel sites.

The third chapter has been dedicated to the study of luminescent properties. Cerium-doped compounds have given the most interesting and original properties. In the oxynitridosilicate, an emission at 545 nm (yellow) has been found, with a main excitation at 400 nm. In the oxynitridogermanate, an emission at 590 nm (orange) has been found, with a main excitation at 390 nm. Both emissions would be suitable to be used in combination with a GaN LED, emitting at 400 nm. Multiple other luminescence features were observed. We have been able, by working at low temperature, and by making comparisons with oxidic compounds reduced under Ar/H_2 to assign the different luminescence features observed to the different available crystallographic sites. Emissions at 545 nm and 590 nm in oxynitridosilicates and oxynitridogermanate respectively have been assigned to a local deformation of the structure brought by strontium atoms in association with nitrogen atoms coordinated to the 6h crystallographic sites. The low absorption observed at the maximum of excitation of this emission indicates that the quantity of these sites is small. The luminescence of Ce^{3+} in the other 6h sites has been found to be blue-shifted by nitrogen introduction compared to the emission of Ce^{3+} in 6h sites in the oxidic samples, only visible at low temperature, which is an unusual feature.

All samples show low external quantum efficiencies. A marked thermal quenching has been identified in all samples and for all emissions. Some optimization work has been carried out with Ce-doped oxynitrido-silicates phosphors. Starting from the same oxide precursor, an ammonolysis with slow cooling gives more intense luminescence properties. Lower cerium concentration leads to a higher luminescence intensity for the emission at 545 nm. Increasing the nitrogen content by changing the ammonolysis parameters do not modify qualitatively the emission features. On the contrary, grayish compounds with high absorption in the emission area have been obtained after ammonolysis at high temperature, which is strongly detrimental to the external quantum efficiency.

Optimization of the phosphors by further investigating the concentration dependence of luminescent properties would constitute an interesting short-term perspective. The main objective would be to increase the proportion of crystallographic sites where the Ce^{3+} emission is shifted at high wavelength. Apatite oxide precursors with other compositions

could be explored. The introduction of elements of high oxidation state like Ti^{4+} in lanthanum silicate apatite has been reported to lead to phases with high nitrogen content [14]. Replacing some La^{3+} atoms by higher oxidation state cations like Zr^{4+} would allow introducing more M^{2+} (M= Ba, Sr ,Ca) cations, responsible for the emissions at 545 and 590 nm, while keeping a high interstitial oxygen content in the oxidic precursor.

References:

[1] Guyader, J., Grekov, F. F., Marchand, R., and Lang, J. *Revue de Chimie Minérale* **15**, 431–438 (1978).

Appendices

Appendix I: Emission and excitation spectra measurements

The emission and excitation spectra have been recorded with a spectrofluorimeter SPEX Fluorolog-2 (Figure A-1) driven by the software DATAMAX. The excitation source is a 450W xenon lamp.

Excitation and emission wavelength are selected by two double monochromators of focal distance 22 cm with a Czerny-Turner configuration. A first monochromator select the wavelength of the light coming to the sample whereas the light emitted by the sample is filtered by the second monochromator. The emission signal is detected and amplified by a photomultiplier Hamamatsu R928 cooled by Peltier effect.

Emission spectra are systematically corrected from the spectral response of the system thanks to a correction file taking in account the variations of the transmission of the monochromator as well as the response of the photomultiplier. Excitation spectra are corrected from the emission profile of the lamp with a system that detect the intensity of the excitation light which is composed by Rhodamine Beta and a photomultiplier, located just after the excitation monochromator.

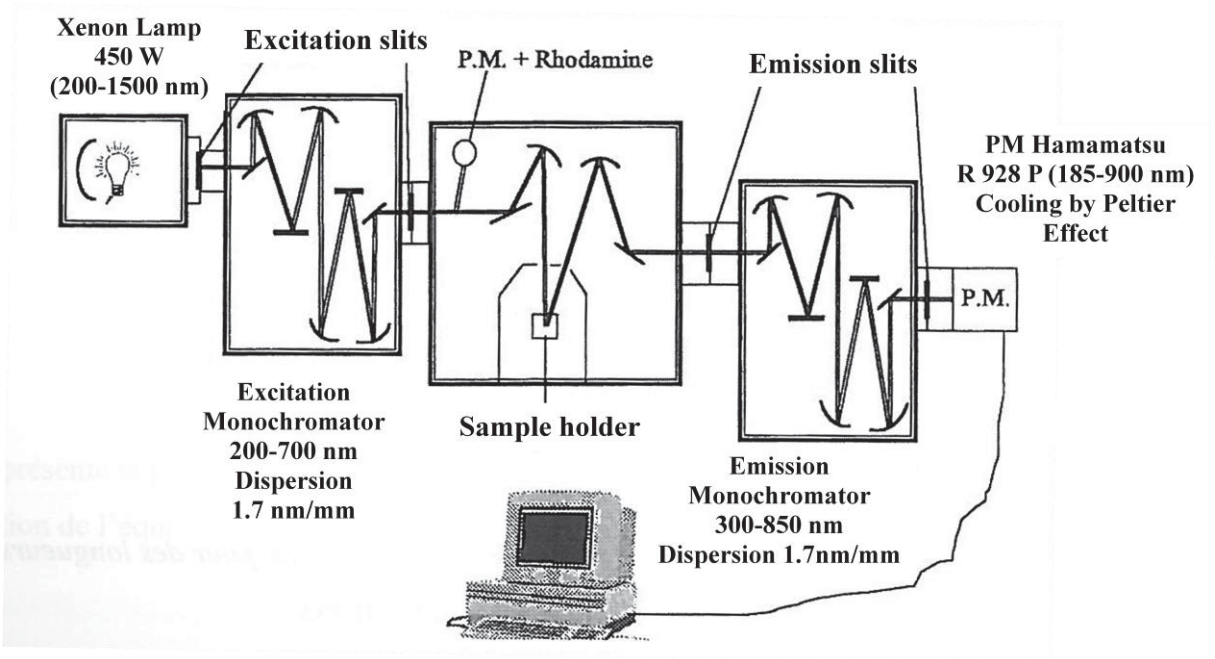

Figure A-1. Experimental set-up of the spectrofluorimeter SPEX Fluorolog-2

Appendix II: Fluorescence measurements at low temperature

Low temperature measurements were performed using two cryostats. In the case of liquid nitrogen measurements, the powder was directly in contact with a bronze sample holder with controlled temperature between 80 K and 295 K. Measurements at constant temperature of 80 K were carried out by means of a vacuum pump which draws up the liquid nitrogen in a capillary running through the device and that is connected to the sample holder. For measurements under liquid helium a double chamber cryostat was used. The first chamber is under high vacuum (10^{-7} mPa), and the second one contains the sample holder in a stream of very low temperature helium gas obtained by vaporization of liquid helium in a capillary wrapped around a heating element to regulate the temperature. A pumping system ensures the circulation of helium gas that allows measurements between 4.5 K and 10 K. A thermal probe was also linked to the sample in both cases.

Figure A-2. Experimental set-up for fluorescence measurements at 4.2K (with liquid helium)

Abstract :
Rare-earth doped oxynitrides have attracted much attention as phosphors for white LEDs. A new family of Ce^{3+} or Eu^{2+}-doped oxynitride phosphors with the apatite structure has been studied: $La_{8+x}Sr_{2-x}(Si/Ge)_6N_yO_{26+x/2-3/2y}$. The ammonolysis of an apatite oxide precursor has been used as a general method of synthesis, allowing decreasing the nitriding temperature respective to the classical solid state reaction in N_2/H_2 atmosphere. The luminescence properties of the obtained phosphors have been studied and relationships with the crystalline structure have been drawn. The apatite structure shows several crystallographic sites available for nitrogen as well as two cationic sites for optically active rare-earth ions. Several structural characterization technique have been used (IR, Raman, NMR, Neutron diffraction) and important information has been obtained concerning the nitrogen distribution in the available positions of the crystal structure. Comparison of the luminescent properties with those of compounds reduced under Ar/H_2 allowed attributing emissions to the different crystallographic sites available in the structure. Quantum efficiency measurements have been carried out as well as trials for improving the intensity of the luminescent properties.

Keywords :

• Phosphor • LED • Oxynitride • Ammonolysis
• Europium • Cerium • Apatite

Titre : Synthèse par Ammonolyse et Etude des Propriétés de Luminescence dans des Oxynitrures de Structure Apatite Dopés au Cérium ou à l'Europium

Résumé :
Les oxynitrures dopés terre rare présentent des propriétés intéressantes pour un usage en tant que luminophore pour LEDs blanches. Une nouvelle famille de luminophores dopés Eu^{2+} ou Ce^{3+} avec un réseau hôte oxynitrure de structure apatite a été étudiée : $La_{8+x}Sr_{2-x}(Si/Ge)_6N_yO_{26+x/2-3/2y}$. L'ammonolyse d'un précurseur oxyde de structure apatite a été utilisée comme technique générale de nitruration. Elle a permis de diminuer substantiellement la température de nitruration en comparaison avec la méthode classique par réaction à l'état solide sous atmosphère mixte N_2/H_2. Les différentes luminescences des luminophores obtenus ont été étudiées et corrélées à la structure cristalline à l'aide de différentes techniques de caractérisation. La structure apatite présente notamment la particularité de proposer plusieurs sites anioniques pour l'introduction de l'azote ainsi que deux sites cationiques pour les ions terre rare activateurs. L'utilisation de nombreuses techniques de caractérisation (IR, Raman, RMN, diffraction des neutrons) a permis d'obtenir des informations sur la position de l'azote. En parallèle, la comparaison des propriétés optiques avec celles de composés réduits sous Ar/H_2 a permis d'attribuer les émissions aux différents sites cristallins disponibles dans la structure. Des mesures de rendement quantique ainsi que des tentatives d'optimisation des propriétés de luminescence ont été effectuées.

Mots clés :

• Luminophore • LED • Oxynitrure • Ammonolyse
• Europium • Cérium • Apatite